

Electronic Theses and Dissertations, 2004-2019

2017

Tensile-Compressive Asymmetry and Anisotropy of Fused Deposition Modeling PLA under Monotonic Conditions

Casey Perkowski
University of Central Florida

 Part of the [Mechanical Engineering Commons](#)
Find similar works at: <https://stars.library.ucf.edu/etd>
University of Central Florida Libraries <http://library.ucf.edu>

This Masters Thesis (Open Access) is brought to you for free and open access by STARS. It has been accepted for inclusion in Electronic Theses and Dissertations, 2004-2019 by an authorized administrator of STARS. For more information, please contact STARS@ucf.edu.

STARS Citation

Perkowski, Casey, "Tensile-Compressive Asymmetry and Anisotropy of Fused Deposition Modeling PLA under Monotonic Conditions" (2017). *Electronic Theses and Dissertations, 2004-2019*. 5576.
<https://stars.library.ucf.edu/etd/5576>

TENSILE-COMPRESSIVE ASYMMETRY AND ANISOTROPY OF FUSED
DEPOSITION MODELING PLA UNDER MONOTONIC CONDITIONS

by

CASEY PERKOWSKI
B.S.M.E University of Central Florida, 2016

A thesis submitted in partial fulfillment of the requirements
for the degree of Master of Science
in the Department of Mechanical and Aerospace Engineering
in the College of Engineering and Computer Science
at the University of Central Florida
Orlando, Florida

Summer Term
2017

© 2017 Casey Perkowski

ABSTRACT

Additive Manufacturing (AM) continues to gain popularity for its ability to produce complexly-shaped final use components that are impractical to manufacture by traditional methods; however, additive manufactured parts contain complex mesostructures that result in directionally-dependent mechanical properties that have yet to be fully characterized. This effort demonstrates a framework of experimental and analytical methods needed to characterize the uniaxial monotonic behavior of fused deposition modeling PLA using tensile and compressive experiments on specimens printed at various orientations. Based on experimental results, the asymmetry and anisotropy of the tensile and compressive response was analyzed for a candidate material. Specimens from different orientations underwent microscopy and failure surface analysis to correlate test data. The material was observed to exhibit tetragonal behavior with tensile-compressive asymmetry. The experimental and simulated results show a strong correlation. Based on the collection of results, analysis, and computations, this work demonstrates a practice that can be used to characterize similar materials for use in AM components.

ACKNOWLEDGMENTS

I would like to thank:

- My family and friends for all of the love and support they have given me throughout my academic career. Namely, my parents for giving me the opportunity to pursue my academic endeavors and motivating me along the way, and my girlfriend, Stephanie, for encouraging, believing in, and loving me.
- Dr. Ali Gordon for the guidance and mentoring with all parts of this thesis as well as for chairing my committee and allowing me to research in the Mechanics of Materials Research Group (MOMRG). I would also like to thank Dr. Eduardo Divo and Dr. Alain Kassab for their time and advice while serving on my defense committee.
- My colleagues in the MOMRG lab for their help. Namely, Aaron Santomauro for his work on this project and for continuing this research after I graduate.
- Dr. Kimberly Schneider and the UCF LEARN program. With a special thanks to my mentees Deziree Lara and Trevor Sheridan for their help and sense of humor working in the lab.
- Dr. Kenneth Church, Dr. Paul Deffenbaugh, Beth Brownell, and all of my friends and colleagues at nScript Inc. and Sciperio Inc. Thank you for the support over the years and I look forward to continuing to work with you all.
- Dr. Thomas Weller and my colleagues at the Center for Wireless and Microwave Information Systems (WAMI) at USF.
- Mrs. Laurie Wray, Mr. Jimmie Melvin, and Mr. Stephen Hommerbocker for the early encouragement that lead me to become an engineer.

TABLE OF CONTENTS

LIST OF FIGURES	vii
LIST OF TABLES	xi
CHAPTER 1: INTRODUCTION	1
CHAPTER 2: BACKGROUND	4
2.1. Additive Manufacturing	4
2.2. Mechanical Characterization.....	8
2.2.1. Tension.....	9
2.2.2. Compression	18
2.3. Theoretical Mechanics	20
2.3.1. Elasticity	21
2.3.2. Failure and Yield Theories.....	26
2.4. Knowledge Gaps	29
CHAPTER 3: EXPERIMENTAL APPROACH	31
3.1. Specimen Fabrication.....	31
3.2. Tensile.....	37
3.3. Compression	39
3.4. Mesostructural Analysis.....	41
CHAPTER 4: EXPERIMENTAL RESULTS	51
4.1. Tensile Testing.....	51

4.1.1. Tensile XY Plane Results	51
4.1.2. Tensile ZX Plane Results.....	54
4.1.3. Tensile ZX+45 Plane Results.....	57
4.1.4. Tensile Failure Analysis.....	60
4.2. Compression	66
4.2.1. Compressive XY Plane Results	66
4.2.2. Compressive ZX Plane Results.....	69
4.2.3. Compressive ZX+45 Plane Results.....	72
4.2.4. Compressive Failure Analysis	74
CHAPTER 5: MODELING	79
5.1. FDM Failure: Methods and Theory	79
5.2. FDM Failure: Implementation and Results.....	81
CHAPTER 6: CONCLUSIONS	87
6.1. Closing Statements on Performed Work.....	87
6.2. Future Work.....	88
APPENDIX A: TSAI-WU FAILURE CODE	90
APPENDIX B: STRESS-STRAIN CURVES	96
APPENDIX C: PRINTER SETTINGS	105
REFERENCES	109

LIST OF FIGURES

Figure 1.1: 3D printed quadcopter (left) with internal fully printed complex RF electronics (right) [1]	2
Figure 1.2: 3D printed rocket injector - CT scan cross section (left) and final part (right) [2].....	2
Figure 1.3: 3D printed medical implants – spinal implant (left)[3] and cranial implant (right)[4].....	2
Figure 2.1: Overview of AM process categories for polymer materials (ASTM 52900, 2015 [5]).....	5
Figure 2.2: FDM printing process schematic [6]	6
Figure 2.3: Cost and time comparison for Traditional and Additive Manufacturing of a geometry complex vs. solid part.....	7
Figure 2.4: Basic schematic of tensile testing (Adapted from [8])	9
Figure 2.5: Specimen orientations from Bertoldi and coauthors	10
Figure 2.6: 0°, θ° and 90° ASTM D3039 Specimens [11]	11
Figure 2.7: Specimen with 76mm radius (a) vs. 244 mm radius (b) [20]	13
Figure 2.8: Component study performed by Domingo-Espin and coauthors	14
Figure 2.9: Modified specimen geometry used by Lanzotti and coauthor.....	15
Figure 2.10: Specimen dimensions for dogbone used by Torres and coauthors [25]	16
Figure 2.11 Orientations tested by Zou and coauthors [26].....	16
Figure 2.12: Specimen orientations tested by Cantrell and coauthors[28]	18
Figure 2.13: Compression specimens oriented flat in the XY plane (left) and vertical (right) from Ahn and coauthors[17].	19
Figure 2.14: Print orientation tested by Guessasma and coauthors [32].....	20
Figure 3.1: Ultimaker 2 FDM 3D printer.....	31
Figure 3.2: Compression specimen dimensions.....	33
Figure 3.3: Tensile specimen dimensions	33
Figure 3.4: Illustration of the coordinate system of the printer.....	34

Figure 3.5: Illustration showing the different specimen orientations	34
Figure 3.6: Example cases for description of specimen orientation	35
Figure 3.7: Image depicting reasoning for support material use in specimen manufacturing	36
Figure 3.8: Printed Y-45 sample with specimens and support material labeled	37
Figure 3.9: Picture of test setup on MTS load frame	38
Figure 3.10: Close up of tensile experiment setup	38
Figure 3.11: Instron test frame setup for compression testing	40
Figure 3.12: Close up of compression testing setup	40
Figure 3.13: Components of Solidworks material cube - (A) Trace cross section (dimensions in mm), (B) Trace, (C) Single layer	42
Figure 3.14: Solidworks material cube whole (left) and sectioned using section tool (right)	42
Figure 3.15: Buehler planar grinder	43
Figure 3.16: Z+0 cross section (left top and bottom) and Z+90 cross section (right top and bottom)	45
Figure 3.17: Z+45 cross section	45
Figure 3.18: Z+22.5 cross section	46
Figure 3.19: Z+67.5 cross section	46
Figure 3.20: Y-22.5 cross section	47
Figure 3.21: Y-45 cross section	47
Figure 3.22: Y-67.5 cross section	48
Figure 3.23: Y-90 cross section	48
Figure 3.24 Y-22.5/Z+45 cross section	49
Figure 3.25: Y-45/Z+45 cross section	49
Figure 3.26: Y-67.5/Z+45 cross section	50
Figure 4.1: Representative stress-strain curves for XY plane specimens in tension	52

Figure 4.2: Tensile strength for XY plane samples.....	53
Figure 4.3: Elastic Modulus for XY plane samples	54
Figure 4.4: Representative stress-strain curves for ZX plane specimens in tension	55
Figure 4.5: Tensile strength for ZX plane samples.....	56
Figure 4.6: Elastic Modulus for ZX plane samples.....	57
Figure 4.7: Representative stress-strain curves for ZX+45 plane specimens in tension.....	58
Figure 4.8: Tensile strength for ZX+45 plane samples.....	59
Figure 4.9: Elastic Modulus for ZX+45 plane samples	60
Figure 4.10: Fractured XY plane specimens.....	61
Figure 4.11: Failure surface for Z+0 specimen.....	62
Figure 4.12: Failure surface for Z+22.5 specimen.....	63
Figure 4.13: Failure surface for Z+45 specimen.....	63
Figure 4.14: Side view of ZX plane specimen failure surfaces	64
Figure 4.15: Side view of ZX+45 plane specimen failure surfaces	64
Figure 4.16: Failure surface for Y-22.5 orientation.....	65
Figure 4.17: Failure surface for Y-45/Z+45 orientation	65
Figure 4.18: Failure surface for Y-90 orientation	66
Figure 4.19: Representative stress-strain curves for XY plane specimens in compression.....	67
Figure 4.20: Compressive strength for XY plane samples	68
Figure 4.21: Elastic modulus for XY plane compression samples	69
Figure 4.22: Representative stress-strain curves for ZX plane specimens.....	70
Figure 4.23: Compressive strength for ZX plane samples.....	71
Figure 4.24: Elastic modulus for ZX plane compression samples.....	71
Figure 4.25: Representative stress-strain curves for ZX plane specimens.....	72

Figure 4.26: Compressive strength for ZX+45 plane samples.....	73
Figure 4.27: Elastic modulus for ZX+45 plane compression samples.....	74
Figure 4.28: Illustration of layer delamination and buckling [44]	75
Figure 4.29: Comparison of Z+67.5 (left) and Z+45 (right) specimens after compressive testing.....	76
Figure 4.30: Brittle fracture of 22.5° and 45° specimens for ZX and ZX+45 planes	77
Figure 4.31: The Y-67.5 (left) and Y-67.5/Z+45 (right) specimens after testing.	77
Figure 4.32: The Y-90 specimen after testing.....	78
Figure 5.1: Tsai-Wu failure criteria vs experimental results for the XY axis in tension and compression	82
Figure 5.2: Tsai-Wu failure criteria vs. experimental results for the ZX axis in tension and compression	83
Figure 5.3: Tsai-Wu failure criteria vs. experimental results for the ZX+45 axis in tension and compression	84
Figure 5.4: Failure surface for uni-axial compression as predicted by the Tsai-Wu criteria.....	85
Figure 5.5: Failure surface for uni-axial tension as predicted by the Tsai-Wu criteria.....	85
Figure 6.1: Component simulation (left) and component testing (right)	89

LIST OF TABLES

Table 3.1: Summary of print settings used	32
Table 3.2: Grinding and polishing steps for polymer sample preparation	44
Table 4.1: Ultimate tensile strength versus orientation in XY plane	52
Table 4.2: Elastic modulus versus orientation in XY plane	54
Table 4.3: Tensile Strength versus orientation in ZX plane.....	56
Table 4.4: Elastic modulus versus orientation in ZX plane	56
Table 4.5: Tensile Strength versus orientation in ZX+45 plane	58
Table 4.6: Elastic modulus versus orientation in ZX+45 plane	59
Table 4.7: Compressive strength versus orientation in XY plane.....	67
Table 4.8: Elastic modulus versus orientation in compression for XY plane	68
Table 4.9: Compressive strength versus orientation in ZX plane	70
Table 4.10: Elastic modulus versus orientation in compression for ZX plane	71
Table 4.11: Compressive strength versus orientation in ZX+45 plane	73
Table 4.12: Elastic modulus versus orientation in compression for ZX+45 plane	73

CHAPTER 1: INTRODUCTION

Additive Manufacturing (AM) or 3D printing has seen a large increase in popularity in recent years. This emerging technology has found quick interest and adoption from many industries due to its ability to rapidly manufacture parts from 3D computer aided design (CAD) models. Currently this ability is used mainly for prototyping purposes. AM has begun to change the design process for engineers. It has given them the ability to cheaply and quickly produce prototypes in order to verify the fit and function of parts before finalizing a design. Before AM, an engineer would send a design out to a machine shop and wait six weeks just to receive the finished part and find out it did not work properly. They would then make the needed revisions and send the design out again. This leads to high costs and long design cycle times. With AM the same engineer can make a design, set it up to be printed, and in the same day be able to see the needed revisions. This allows for much quicker and lower cost design cycles.

Although AM is a powerful tool for prototyping, the true potential lies in being able to manufacture end use parts. AM has a number of advantages over traditional manufacturing methods. These include the ability to create parts with minimal waste material, the ability to create complex geometries that cannot be manufactured using traditional methods, and the ability to easily produce customized parts since it requires no special tooling. An example of specialty parts that are enabled through 3d printing can be seen in Figure 1.1 - Figure 1.3. In order to continue to leverage the advantages of AM, however, the mechanical properties and performance of the materials that are used need to be fully understood. This has not yet been accomplished for AM materials.



Figure 1.1: 3D printed quadcopter (left) with internal fully printed complex RF electronics (right) [1]

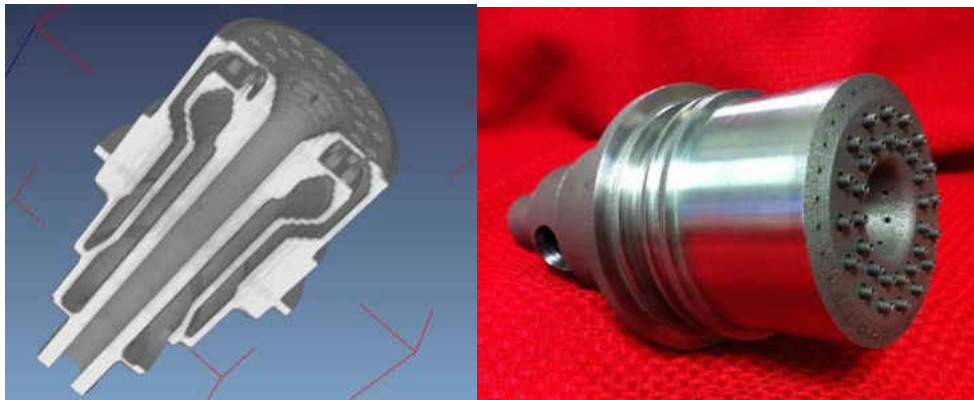


Figure 1.2: 3D printed rocket injector - CT scan cross section (left) and final part (right) [2]



Figure 1.3: 3D printed medical implants – spinal implant (left)[3] and cranial implant (right)[4]

This thesis looks to present a framework to fully characterize the mechanical responses of 3D printed materials. Fused deposition modeling (FDM) PLA is the candidate material of the study. Tensile and compressive testing on specimens manufactured in numerous orientations are conducted. The data generated is used to investigate the relationship between the mechanical response and the material orientation. To help understand the driving factor for failure, the failure modes will be studied. Additionally, a mesostructure analysis will be done to gain insight on the changing internal geometries. The properties found will be used to generate a failure surface in tension and compression for the candidate material.

To begin this paper the processes involved in additive manufacturing and the research that has been done to characterize the mechanical response of FDM materials will first be discussed. Then, the theoretical background for the elastic behavior and failure of a material will be outlined. The knowledge gaps in the field of research will be identified. The procedures for printing specimens, and tensile and compressive testing will be detailed. A mesostructure study will be shown to support the specimen orientations chosen. Next the results from the uniaxial testing will be presented and discussed. Finally a failure surface based on the Tsai-Wu failure criteria will be fit to the experimental results.

CHAPTER 2: BACKGROUND

2.1. Additive Manufacturing

Additive Manufacturing (AM) is an all-encompassing term that describes a number of manufacturing processes in which material is selectively added or layered in order to create 3D objects. Using thermal or chemical reaction bonding, materials in powder, resin, or filament form are fused together to build and bond layers together. Processes exist for manufacturing of parts in most material types, including ceramics, metals, polymers, and composites. This thesis will focus on the manufacturing processes for polymer materials.

Polymer printing can happen by way of numerous processes such as Stereolithography (SLA), PolyJet, Selective Laser Sintering (SLS), Selective Laser Melting (SLM), Laminated Object Manufacturing (LOM), etc. These numerous processes fall under six categories as outlined in the ASTM 52900 standard for AM terminology. Those include binder jetting, material extrusion, material jetting, powder bed fusion, sheet lamination, and vat photopolymerization. Figure 2.1 shows an overview of each process category for AM of polymer materials. Processes are categorized by the method used to fuse the material, the material feedstock type used, where material is positioned in the machine, and overarching principle of the process. For fusion methods, thermal or chemical bonding can be used. Thermal bonding methods include the use of a laser or electric heating element to melt a material. Chemical methods consist of the use of a liquid binder or ultra violet light to induce curing or bonding of a material. Material feedstock can be in a solid form such as filament or pellets, liquid form such as light-activated resin, or powder form. Material distribution refers to where the material is located in the machine. For example both material jetting and vat polymerization use photopolymer resin, but material jetting has the resin located inside of a printing head and vat polymerization uses a vat of resin.

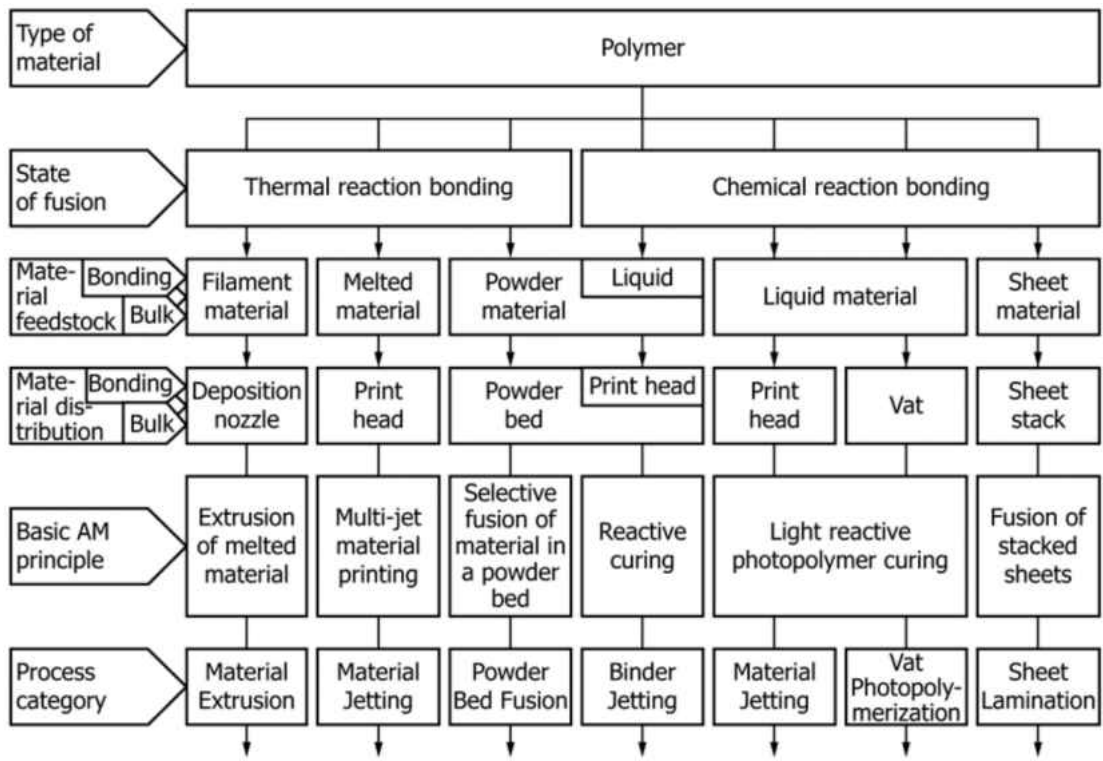


Figure 2.1: Overview of AM process categories for polymer materials (ASTM 52900, 2015 [5])

For the manufacturing of specimens for mechanical testing in this thesis, the process chosen was Fused Deposition Modeling. Fused Deposition Modeling falls under the material extrusion category. In order to print, it uses thermoplastic in filament form on a spool and extrudes it out of a heated nozzle. Figure 2.2 shows a schematic the FDM process. The schematic shows how the filament is pushed into the heated section using an extruder wheel. The filament travels through the heated area, is melted, and gets pushed out of the nozzle. The heated area (or melt zone) is temperature controlled using a closed loop feedback system that consist of a thermocouple or thermistor to measure temperature and a cartridge heater to heat the area. The melted material exits the nozzle and is deposited onto a build platform. Using x-y motion the material is printed into a pattern corresponding to the first layer of the object. The z axis is then moved by one layer height, and the next layer is deposited on the previous layer. This process is repeated until all layers, and therefore the object, are complete.

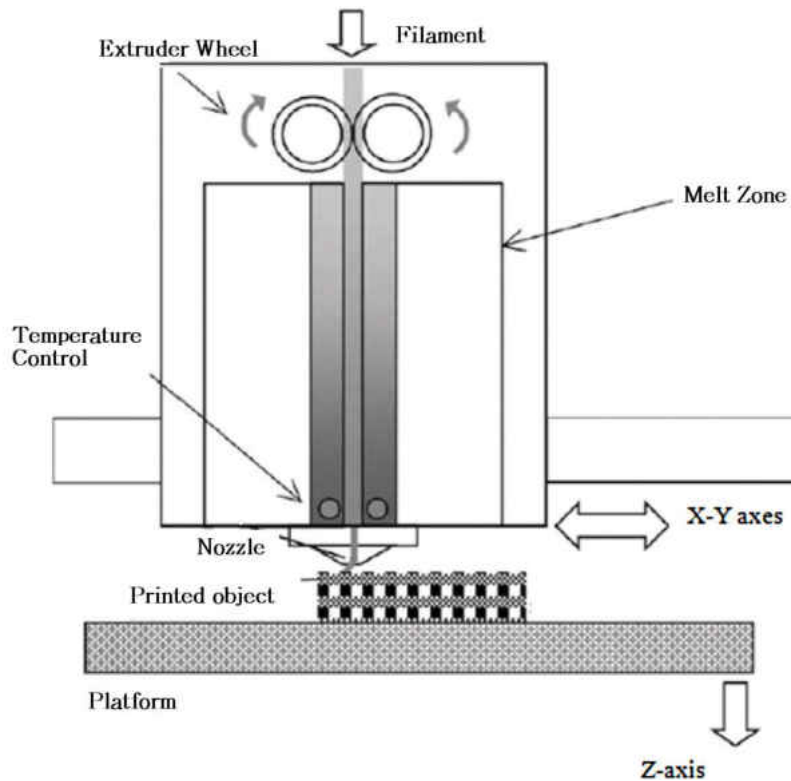


Figure 2.2: FDM printing process schematic [6]

Thanks to the layering process that is used by FDM and other AM methods, they are able to create complexly shaped geometries that are impossible or impractical to manufacture using traditional methods. For FDM it actually reduces cost and manufacturing time to have a more complex shape as compared to a solid shape of the same size. This is illustrated in Figure 2.3 which compares a simple solid linkage with a topologically optimized linkage design that has a very complicated shape. As the table highlights, although the optimized design is lighter and more complex, for FDM it is lower cost and will take less time to produce. This is because the cost of FDM parts is a balance between machine time and material cost. The optimized design uses less material and since there is less material the part can be printed in less time. This is contrary to traditional subtractive methods such as Computer Numerical

Control (CNC) machining, which removes material from material stock to make parts. In the case of the linkages, for CNC machining both would require the same size initial block of material, but the optimized design would require much more material to be removed in the machining process. This would increase the machining time and therefore the cost. This ability to have increased complexity without increased cost is what has helped increase the popularity of AM throughout industry.



	
Solid Design	Optimized Design
Less complex	More complex
Higher weight	Lower weight
Additive Manufacturing	
Higher cost	Lower cost
Longer print time	Shorter print time
Traditional Manufacturing	
Lower cost	Higher cost
Shorter manufacturing time	Longer manufacturing time

Figure 2.3: Cost and time comparison for Traditional and Additive Manufacturing of a geometry complex vs. solid part¹

Although AM can produce complex parts, the mechanical performance of such printed parts can be very hard to predict. This is due to the variability and anisotropy that is inherent to printed materials. The mechanical properties are dependent on both orientation and printer settings. Special considerations need to be taken when characterizing the mechanical properties of AM materials. This has caused mechanical properties and materials to be the most studied topic with regard to AM. In their literature review, Costabile and co-authors examined the number of published papers about AM yearly and the

¹ It should be noted that this is not a direct comparison of the two technologies cost and manufacturing time but rather an illustration of the effect of complexity on cost and manufacturing time for each manufacturing technique individually.

topics in which they addressed. They found that in 2005 there were roughly 1000 paper published about various AM topics, 500 of which dealt with mechanical properties and materials. The yearly total grew to roughly 1900 paper in 2010 with 1000 being about mechanical properties and materials. Increasing to approximately 4400 paper in 2015 with 2600 covering mechanical properties and materials [7]. These past publications which deal with FDM materials specifically will be discussed further in following sections. The methods used for mechanical characterization will be investigated, the theory behind elastic behavior of anisotropic materials and material yielding will be discussed, the previous findings on anisotropy of FDM structures will be presented, and the gaps that previous publications leave behind will be highlighted.

2.2. Mechanical Characterization

The mechanical characterization of FDM materials can be very complicated due to the large number of variables in the manufacturing process. As stated before, this has made mechanical response and materials the most popular topic for AM research. Many papers have been published on the characterization of FDM materials using tensile testing, less have been published on compressive testing.

Unlike many areas of study which show a progression of ideas and discoveries over time, the study of FDM material behavior is relatively new and has been focused on applying known mechanical theories to this new manufacturing method. The papers have mainly investigated the effects of many of the process variables on the mechanical behavior. These variables studied fall include two categories. The first is the effect of printer settings on the mechanical response of test specimens. Printer settings refer to the user assigned characteristics of the printing process such as the layer height, line width, extrusion temperature, print speed, and so on. The second category is the effect of orientation on the mechanical response of test specimens. The orientation refers to how the specimen is positioned with respect to the major axis, infill pattern and build direction. Through this section, the extent to which both of these

categories of variables have been studied using tensile and compressive monotonic testing with be presented by identifying the methods and variables studied by each paper. These will be done using small summaries of each paper.

2.2.1. Tension

Tensile testing is the most common form of experiment used to obtain the mechanical properties of standard materials. A simple schematic of a tension test setup can be seen in Figure 2.4. It consist of a crosshead that can be move upward or downward, a tensile specimen, an extensometer to measure the local extension of the specimen, a load cell to measure the pulling force on the specimen, and grips that connect to the load cell and crosshead and holds the specimen during testing.

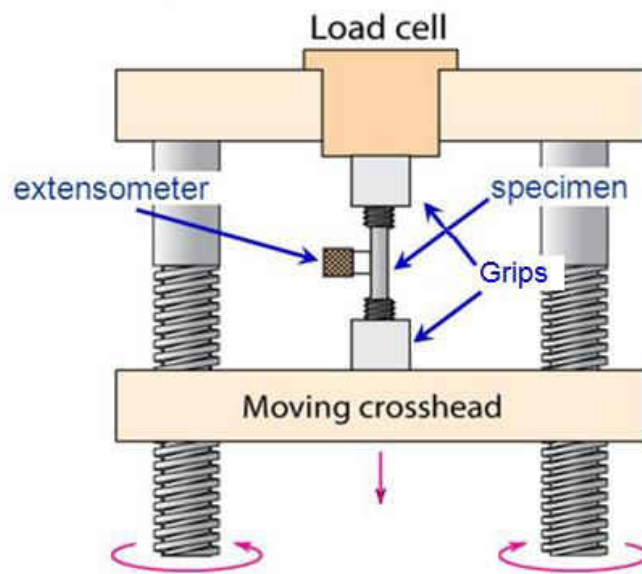


Figure 2.4: Basic schematic of tensile testing (Adapted from [8])

Bertoldi and coauthors measured the ultimate tensile strength (UTS), Elastic modulus, and Poisson's ratio of Acrylonitrile butadiene styrene (ABS) specimens printed in 6 orientations [9]. A representation of the specimen orientations can be seen in Figure 2.5. Printer settings were held constant for all samples. Two specimens were printed in each plane. One specimen along the primary axis and another angled +45 degrees from the primary axis. For the infill of the specimens a layering sequence of $0^{\circ}/90^{\circ}/+45^{\circ}/-45^{\circ}$ was used in hopes to achieve a quasi-isotropic behavior.

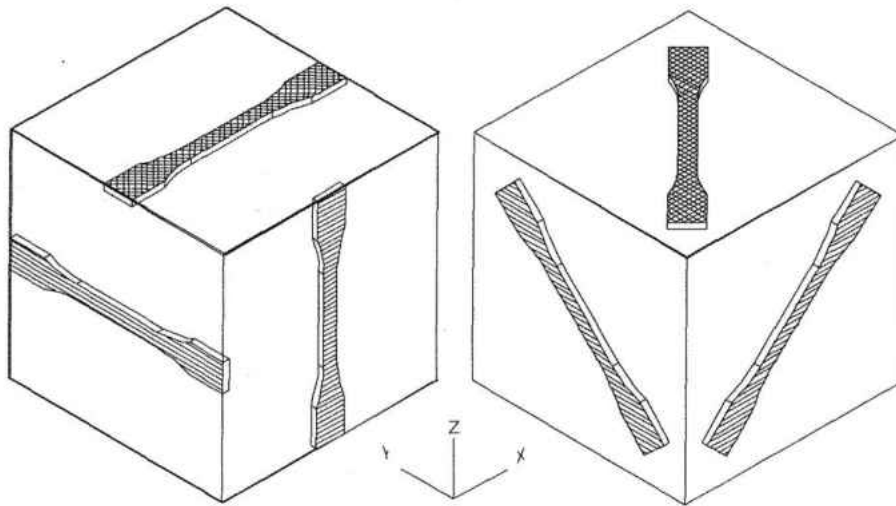


Figure 2.5: Specimen orientations from Bertoldi and coauthors

For the tensile testing and specimen preparation, the ASTM D5937 standard was used [10]. This standard was meant for extruded and molded plastic materials and has since been withdrawn by ASTM. In order to measure the Poisson's ratio during testing, an axial and a transverse extensometer were used.

Rodriguez and coauthors released a number of papers pertaining to FDM ABS. Two of which related to tensile experiment [11, 12]. In these papers the UTS and elastic modulus of ABS test specimens were measured. For testing they followed the ASTM D3039 standard meant for polymer matrix

composites. The specimen type and dimensions can be seen in Figure 2.6. Per this standard a flat plate is produced and metal tabs are glued onto the ends as support. In the study, specimens in the XY plane at $\theta = 0^\circ, 10^\circ, 45^\circ,$ and 90° were tested. These were all printed uniaxially. Uniaxial prints have all deposited traces running in the direction corresponding to θ .

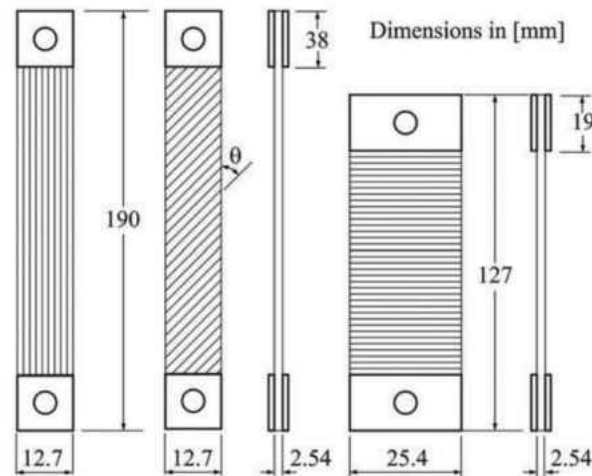


Figure 2.6: $0^\circ, \theta^\circ$ and 90° ASTM D3039 Specimens [11]

Rodriguez and coauthors remaining works focused on the mesostructure of uniaxially printed parts [13-15]. Through sectioning and microscopy of printed samples the authors characterized the mesostructure. They worked to create a constitutive model leveraging the mesostructure study and experimental results.

ES-Said and coauthors studied the tensile loading of specimens printed both uniaxially in the XY plane at $0^\circ, 45^\circ,$ and 90° and with crossing layers of $+45^\circ/-45^\circ$ and $0^\circ/45^\circ$. They used ABS and reported the UTS and yield strength. They used the ASTM D638 standard for testing, however their specimens were of non-standard dimensions.

Montero and coauthors measured the effect of filament color, line width, print temperature, and air gap the on UTS and elastic modulus of specimens printed uniaxially at 0° and 90° in the XY plane [16,

17]. They also measured the strength of specimens printed with $+45^\circ/-45^\circ$ and $0^\circ/90^\circ$ layers. In their testing they first used the ASTM D638 type 1 specimen, but ran into trouble due to premature rupturing of samples. They moved to the ASTM D3039 standard for testing after this trouble.

Li and coauthors measured the effect of air gap on Poisson's ratio and elastic modulus of specimens printed uniaxially in the XY plane at 0° , 45° , and 90° [18]. They also measured the elastic modulus of specimens printed with $0^\circ/90^\circ$, $15^\circ/75^\circ$, $30^\circ/60^\circ$, and $+45^\circ/-45^\circ$ layers. They used the ASTM 3039 standard for testing.

Sood and coauthors studied the effects of layer height, line width, and airgap on samples with raster angles of 0° , 30° , and 60° [19]. Samples were oriented at 0° , 15° , and 30° in the XY plane. ISO R527:1966 standard was used for testing. Tensile strength was reported and the material used was ABS.

Croccolo and coauthors studied the effect of contours on specimens in the XY plane and one oriented 90° onto its side. In the study, they began with an ASTM D638 type 1 specimen geometry[20]. They found there was a stress concentration at the radius that caused fracture to occur out of the gage length (Figure 2.7a). In order to mitigate this, they created a specimen with a much larger radius of 244 mm that fractured more consistently within the gage length (Figure 2.7b).

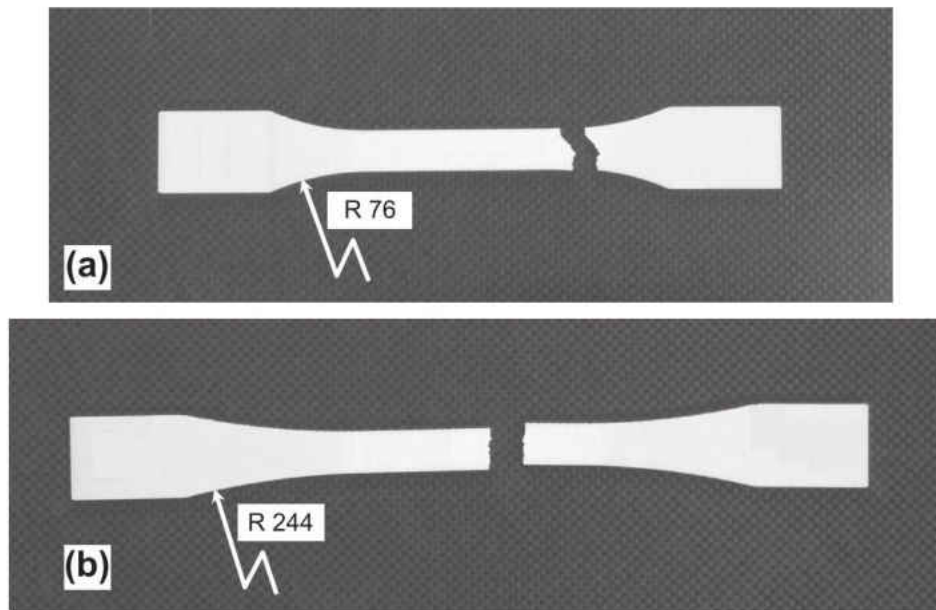


Figure 2.7: Specimen with 76mm radius (a) vs. 244 mm radius (b) [20]

Using this new specimen they studied the strength and stiffness of samples with 1, 4, 7, and 10 contours (alternatively called perimeters) and $+45^\circ/-45^\circ$ infill. The material used was ABS.

Hill and Haghi measured the UTS, yield strength, elongation at break and elastic modulus of specimens printing uniaxially in the XY plane at angles from 0° to 90° in increments of 15° [21]. They used the ASTM D638 type 1 specimen and ABS. Using the result, they developed a direction dependent failure criteria which was driven by the strength of the individual traces in tension, the strength of the welds between traces in tension, and the strength of the welds under shear.

Domingo-Espin and coauthors did a study very similar to Bertoldi and coauthors in which they measured the mechanical properties of FDM polycarbonate (PC) in the same orientations (Figure 2.5) [22]. They used the ASTM D638 standard type 1 dogbone printed with a single perimeter and $+45^\circ/-45^\circ$ infill pattern. Using the test data they developed a stiffness matrix based of the orthotropic material

model. Using this model they were able to do a component study in which they simulated and tested a printed L-shaped beam (Figure 2.8).

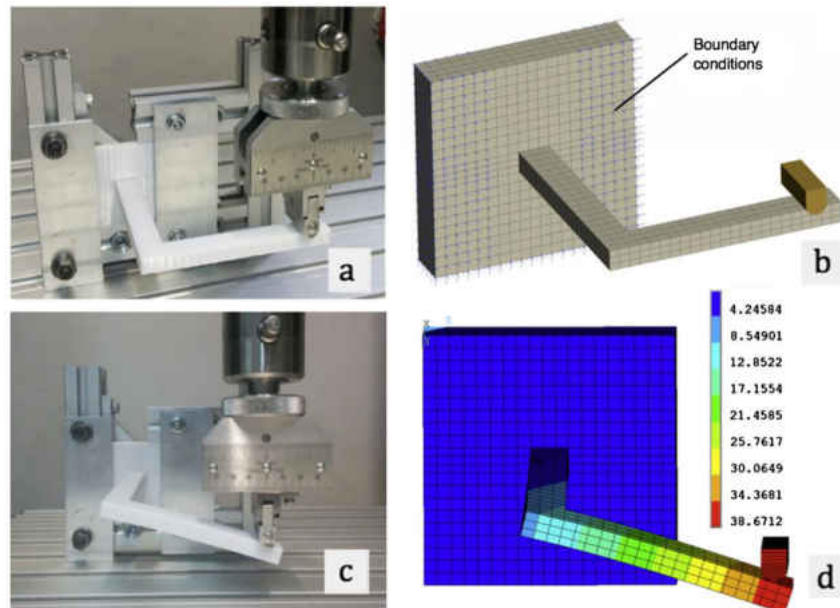


Figure 2.8: Component study performed by Domingo-Espin and coauthors

Lanzotti and coauthors studied the mechanical properties of PLA printed on a low cost 3D printer[23]. They looked at the effects of perimeters and layer height on the UTS and strain at break for samples printed in with 0° , 18° , 45° , 72° , and 90° uniaxial infill. They used a modified ASTM 638 specimen (Figure 2.9) in which large parabolic radii were added to the transition in width to reduce the stress concentration in the area and insure failure at the smallest cross section.

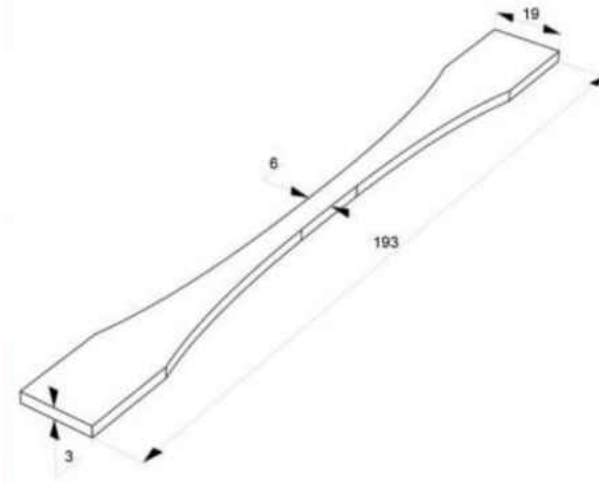


Figure 2.9: Modified specimen geometry used by Lanzotti and coauthor

Torrado and Roberson did a study on the effect of specimen geometry on the results obtained from tensile test of ABS [24]. In the study he compared ASTM D638 type 1, 4, and 5 specimens printed with uniaxial 0° and 90° infill, and $0^\circ/90^\circ$ crosshatch infill. They showed that different specimen types yielded different UTS and elongation at break results. They also investigated the fracture surface of the specimens and found varying form of fracture propagation for different specimen geometries. These finding led them to call for a specific testing standard for FDM parts that possibly used multiple specimen geometries for the different orientations.

Torres and coauthors measured the effects of a number of variables on PLA specimens printed flat, rotated 90° about the x-axis (on edge), and another rotated 90° about the y-axis (vertical) [25]. The variables tested included the printing temperature, infill orientation, infill density, print speed, layer height, and use of perimeter. They used both $0^\circ/90^\circ$ and $+45^\circ/-45^\circ$ infill orientations. The ASTM D638 standard was used, however a non-standard specimen geometry was used (Figure 2.10). This geometry used a small radius as the transition to the gage section. This contradicts the previous studies that used

custom geometries in which they increased the radius greatly. In the study, the elastic modulus, 0.2% yield strength, UTS and toughness were reported.

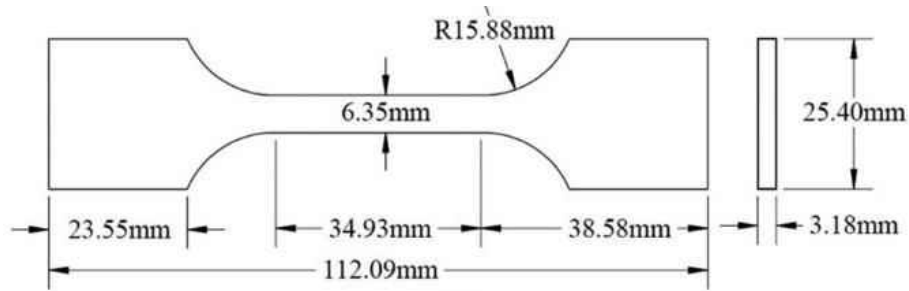


Figure 2.10: Specimen dimensions for dogbone used by Torres and coauthors [25]

Zou and coauthors studied ABS specimens oriented 0° , 30° , 45° , 60° , and 90° in the zx plane (Figure 2.11) [26]. They used the ISO 527-2 for testing and employed the type 1B specimen geometry. Printer settings were kept constant for all samples. The tensile strength, max strain, elastic modulus, and Poisson's ratio were recorded. The Poisson's ratio was captured using a biaxial strain gauge that was adhered to the sample.

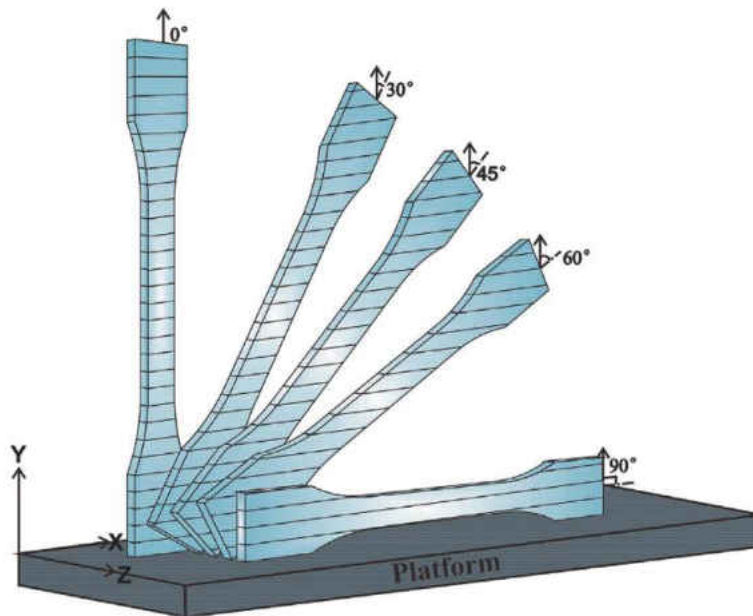


Figure 2.11 Orientations tested by Zou and coauthors [26]

Garg and Bhattacharya performed an in-depth finite element analysis study on the behavior of ABS parts printed in the xy plane with uniaxial 0° and 90° and alternating $0^\circ/90^\circ$ infill under tension. For their experimental validation they did tensile testing of specimens with varying layer height and alternating $0^\circ/90^\circ$ infill. They used the ASTM D638 standard was applied for testing and the ASTM D638 type 4 dogbone geometry was used [27]. No specific mechanical properties were reported. The failure mechanisms predicted by the FEA simulation were compared to the observed failure mechanisms instead.

Cantrell and coauthors performed an in depth study of both ABS and PLA for specimens at various orientations[28]. The specimens were printed at 0° , 15° , 30° , and 45° in the xy plane, rotated 90° about the x axis onto their side and printed at 0° and 45° and rotated 90° about the y axis and printed on end at 0° and 45° . Figure 2.12 shows an illustration of the orientations. The infill was kept at a constant +45/-45 pattern for all prints. For the experiments, the ASTM D638 standard was followed, and the type 4 specimen geometry was used. The Poisson's ratio, elastic modulus, yield strength, ultimate strength, strain at failure, breaking strength, and strain energy density were all reported for each orientation for both ABS and PC.

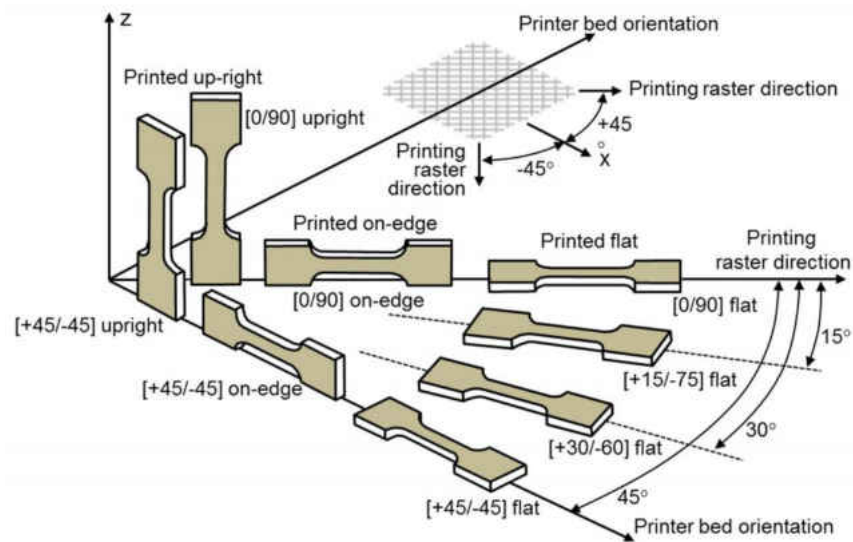


Figure 2.12: Specimen orientations tested by Cantrell and coauthors[28]

2.2.2. Compression

Ahn and coauthors were the first to study the mechanical properties of an FDM material under compressive loading [17]. For the experiments, ABS was used and specimens from the xy plane (flat) and rotated 90° about the y axis (vertical) orientations were tested. For the specimen geometry and testing, the ASTM D695 standard was used [29]. The specimens tested can be seen in Figure 2.13 and have a 1 inch height and ½ inch diameter. In this study, only the compressive strength was reported. The most important finding of these experiments is that the tensile and compressive strengths were not equal. Although this was well established for polymeric materials, it was yet to be shown for an FDM material.

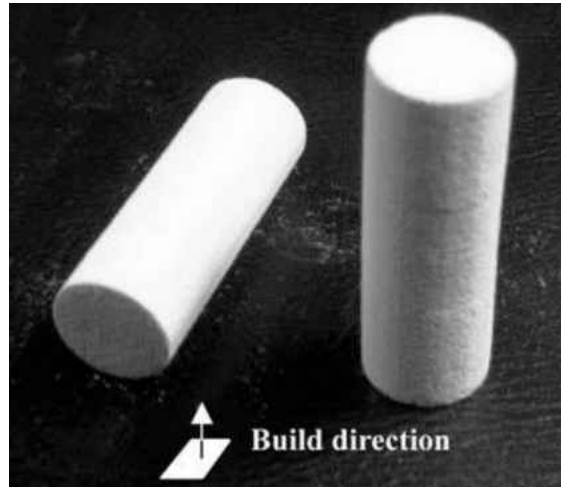


Figure 2.13: Compression specimens oriented flat in the XY plane (left) and vertical (right) from Ahn and coauthors[17].

Lee and coauthors did a study to compare FDM, powder bed fusion, and a novel printing technique they had developed [30]. To do so, they used compression samples to measure the strength in different orientations. For the FDM, the test procedure was an exact match to that used by Ahn and coauthor in the last work described. An interesting note however, is that for the powder bed fusion an off-axis diagonal sample was manufactured and tested. This is the first example of an off axis sample being tested.

Sood and coauthors performed an experiment to optimize the print settings in order to maximize the compressive strength of FDM samples [31]. To achieve this, they created a test matrix consisting of high, medium, and low settings for build orientation, air gap, layer thickness, raster angle, and raster width. In the test matrix, specimens printed with the long side flat on the bed, and at angles of 15° and 30° off of the bed were tested. Specimens at each orientation also were tested with varying raster angles of 0° , 30° , and 60° . All tested were performed with prismatic square samples with dimension 10mm x 10mm x 30mm and using ISO 604-1973 standard. Samples were found to fail due to layers buckling, and delaminating.

Guessasma and coauthors extensively studied the strength and failure of ABS cubes under compression[32]. For the experiments, 30 mm cubes were printed using $-45^{\circ}/45^{\circ}$ infill. Cubes were printed at orientation rotated 0° 30° 45° , and 60° about the z-axis of the printer (see Figure 2.14). Each cube orientation was then tested in compression along the x, y, and z axis of the cube. No test standard was used during the experiments. The yield strength and elastic modulus was reported for each orientation. Extensive examination of the damage experienced by the cubes after severe compression was performed using X-ray micro-tomography. This gave an in depth look at the voids and cracks at multiple cross sections of the cubes after testing.

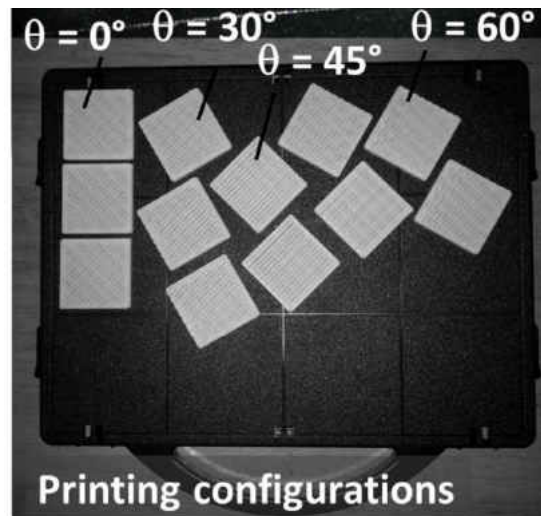


Figure 2.14: Print orientation tested by Guessasma and coauthors [32].

2.3. Theoretical Mechanics

2.3.1. Elasticity

For nearly all publications, FDM materials have been treated as homogenous and linear elastic. Linear elastic materials behave such that the applied stress experienced by a body can be mapped to the strains that will occur using a proportional relationship. This relationship is commonly referred to as Hooke's Law. In the generalized form, the stress-strain relationship can be expressed as

$$\sigma_{ij} = C_{ijkl} \varepsilon_{kl} \quad , \quad \text{where } i,j,k,l = 1, 2, 3 \quad (2.1)$$

where the stiffness tensor C is a fourth-order tensor comprised of 81 constants. The number of constants can be initially reduced using physical constraints such as the satisfaction of equilibrium at an arbitrary point in a material. This equilibrium constraint provides the initial simplification which is the symmetry of the stress and strain tensors, i.e.

$$\sigma_{ij} = \sigma_{ji} \quad (2.2)$$

$$\varepsilon_{kl} = \varepsilon_{lk} \quad (2.3)$$

This causes the stiffness tensor to be reduced to having 36 independent constants. Furthermore, the stiffness tensor itself is also symmetric such that

$$C_{ijkl} = C_{jikl} = C_{ijlk} = C_{klij} \quad (2.4)$$

This leaves 21 independent constants in the stiffness matrix C . By exploiting equations 2.2, 2.3, and 2.4, a contracted notation can be used to express the stress-strain relationship. This is referred to as Voigt notation and works by transforming the stress and strain tensors from second to first order tensors in which the six independent components of stress are transformed as follows

$$\sigma_{11} = \sigma_1$$

$$\sigma_{22} = \sigma_2$$

$$\begin{aligned}
\sigma_{33} &= \sigma_3 \\
\sigma_{23} &= \sigma_4 \\
\sigma_{31} &= \sigma_5 \\
\sigma_{12} &= \sigma_6
\end{aligned} \tag{2.5}$$

For the strain, in order to get consistency between forms, the shear components need to be multiplied by two. The result for the strain transformation is

$$\begin{aligned}
\varepsilon_{11} &= \varepsilon_1 \\
\varepsilon_{22} &= \varepsilon_2 \\
\varepsilon_{33} &= \varepsilon_3 \\
2\varepsilon_{23} &= \varepsilon_4 \\
2\varepsilon_{31} &= \varepsilon_5 \\
2\varepsilon_{12} &= \varepsilon_6
\end{aligned} \tag{2.6}$$

This form also allows the stiffness tensor to be reduced to the simplified 6 x 6 matrix seen below.

$$C = \begin{bmatrix} C_{11} & C_{12} & C_{13} & C_{14} & C_{15} & C_{16} \\ C_{12} & C_{22} & C_{23} & C_{24} & C_{25} & C_{26} \\ C_{13} & C_{23} & C_{33} & C_{34} & C_{35} & C_{36} \\ C_{14} & C_{24} & C_{34} & C_{44} & C_{45} & C_{46} \\ C_{15} & C_{25} & C_{35} & C_{45} & C_{55} & C_{56} \\ C_{16} & C_{26} & C_{36} & C_{46} & C_{56} & C_{66} \end{bmatrix} \tag{2.7}$$

This is the general form of the stiffness matrix for elastic homogeneous materials and can be used to describe the elastic response of an anisotropic material. However, to individually test for all 21 constants in order to characterize a candidate material would be time consuming and in almost all cases redundant. It is much more convenient to further simplify the stiffness matrix.

Further simplification of the stiffness matrix can be done using the symmetries observed in the materials themselves and the assumed invariance that accompanies them. Using a method explained fully by Bos and Slawinski [33], by knowing the requirement of invariance with respect to M for the stiffness matrix C ,

$$C = M^T C M \tag{2.8}$$

We can use matrices to enforce different types of symmetry onto the stiffness matrix. For this case the transformation matrix M has two forms, M_A and M_B , where

$$M_A = \begin{bmatrix} A_{11}A_{11} & A_{12}A_{12} & A_{13}A_{13} & A_{12}A_{13} & A_{11}A_{13} & A_{11}A_{12} \\ A_{21}A_{21} & A_{22}A_{22} & A_{23}A_{23} & A_{22}A_{23} & A_{21}A_{23} & A_{21}A_{22} \\ A_{31}A_{31} & A_{32}A_{32} & A_{33}A_{33} & A_{32}A_{33} & A_{31}A_{33} & A_{31}A_{32} \\ 2A_{21}A_{31} & 2A_{22}A_{32} & 2A_{23}A_{33} & A_{22}A_{33} + A_{23}A_{32} & A_{21}A_{33} + A_{23}A_{31} & A_{21}A_{32} + A_{22}A_{31} \\ 2A_{11}A_{31} & 2A_{12}A_{32} & 2A_{13}A_{33} & A_{12}A_{33} + A_{13}A_{32} & A_{11}A_{33} + A_{13}A_{31} & A_{11}A_{32} + A_{12}A_{31} \\ 2A_{11}A_{21} & 2A_{12}A_{22} & 2A_{13}A_{23} & A_{12}A_{23} + A_{13}A_{22} & A_{11}A_{23} + A_{13}A_{21} & A_{11}A_{22} + A_{12}A_{21} \end{bmatrix} \quad (2.9)$$

Where A can either equal A_θ for a rotation symmetry corresponding to θ about the x_3 -axis or A'_θ which represents a reflection about the x_1x_2 plane when $\theta = 0^\circ$.

$$A = A_\theta = \begin{bmatrix} \cos(\theta) & -\sin(\theta) & 0 \\ \sin(\theta) & \cos(\theta) & 0 \\ 0 & 0 & 1 \end{bmatrix} \quad \text{or} \quad A'_\theta = \begin{bmatrix} \cos(\theta) & -\sin(\theta) & 0 \\ \sin(\theta) & \cos(\theta) & 0 \\ 0 & 0 & -1 \end{bmatrix} \quad (2.10)$$

Or we can use M_B to represents a reflection about the x_1x_2 plane.

$$M_B = \begin{bmatrix} 1 & 0 & 0 & 0 & 0 & 0 \\ 0 & 1 & 0 & 0 & 0 & 0 \\ 0 & 0 & 1 & 0 & 0 & 0 \\ 0 & 0 & 0 & -1 & 0 & 0 \\ 0 & 0 & 0 & 0 & 1 & 0 \\ 0 & 0 & 0 & 0 & 0 & -1 \end{bmatrix} \quad (2.11)$$

The first class of anisotropic materials are monoclinic materials. Monoclinic materials have a single reflective symmetry about an arbitrary plane. By applying any planar reflection (in this case $M_{A'_0}$ was chosen) we can derive the simplified stiffness matrix. Starting by substituting $M_{A'_0}$ into (2.8),

$$C = M_{A'_0}^T C M_{A'_0} \quad (2.12)$$

We can evaluate this equality to obtain

$$\begin{bmatrix} C_{11} & C_{12} & C_{13} & C_{14} & C_{15} & C_{16} \\ C_{12} & C_{22} & C_{23} & C_{24} & C_{25} & C_{26} \\ C_{13} & C_{23} & C_{33} & C_{34} & C_{35} & C_{36} \\ C_{14} & C_{24} & C_{34} & C_{44} & C_{45} & C_{46} \\ C_{15} & C_{25} & C_{35} & C_{45} & C_{55} & C_{56} \\ C_{16} & C_{26} & C_{36} & C_{46} & C_{56} & C_{66} \end{bmatrix} = \begin{bmatrix} C_{11} & C_{12} & C_{13} & -C_{14} & -C_{15} & C_{16} \\ C_{12} & C_{22} & C_{23} & -C_{24} & -C_{25} & C_{26} \\ C_{13} & C_{23} & C_{33} & -C_{34} & -C_{35} & C_{36} \\ -C_{14} & -C_{24} & -C_{34} & C_{44} & C_{45} & -C_{46} \\ -C_{15} & -C_{25} & -C_{35} & C_{45} & C_{55} & -C_{56} \\ C_{16} & C_{26} & C_{36} & -C_{46} & -C_{56} & C_{66} \end{bmatrix} \quad (2.13)$$

When equating, it is clear that

$$C_{14} = C_{15} = C_{24} = C_{25} = C_{34} = C_{35} = C_{46} = C_{56} = 0 \quad (2.14)$$

and

$$C = \begin{bmatrix} C_{11} & C_{12} & C_{13} & 0 & 0 & C_{16} \\ C_{12} & C_{22} & C_{23} & 0 & 0 & C_{26} \\ C_{13} & C_{23} & C_{33} & 0 & 0 & C_{36} \\ 0 & 0 & 0 & C_{44} & C_{45} & 0 \\ 0 & 0 & 0 & C_{45} & C_{55} & 0 \\ C_{16} & C_{26} & C_{36} & 0 & 0 & C_{66} \end{bmatrix} \quad (2.15)$$

This leaves the stiffness matrix with 13 independent constants. To further simplify and step to the next class of anisotropic materials, an additional reflection about the x_1x_2 plane can be added to the monoclinic stiffness matrix (2.15). This is done by substituting the M_B matrix into (2.8).

$$C = M_B^T C M_B \quad (2.16)$$

This leads to the equality

$$\begin{bmatrix} C_{11} & C_{12} & C_{13} & 0 & 0 & C_{16} \\ C_{12} & C_{22} & C_{23} & 0 & 0 & C_{26} \\ C_{13} & C_{23} & C_{33} & 0 & 0 & C_{36} \\ 0 & 0 & 0 & C_{44} & C_{45} & 0 \\ 0 & 0 & 0 & C_{45} & C_{55} & 0 \\ C_{16} & C_{26} & C_{36} & 0 & 0 & C_{66} \end{bmatrix} = \begin{bmatrix} C_{11} & C_{12} & C_{13} & 0 & 0 & -C_{16} \\ C_{12} & C_{22} & C_{23} & 0 & 0 & -C_{26} \\ C_{13} & C_{23} & C_{33} & 0 & 0 & -C_{36} \\ 0 & 0 & 0 & C_{44} & -C_{45} & 0 \\ 0 & 0 & 0 & -C_{45} & C_{55} & 0 \\ -C_{16} & -C_{26} & -C_{36} & 0 & 0 & C_{66} \end{bmatrix} \quad (2.17)$$

Which results in the stiffness matrix that describes the behavior of an orthotropic material,

$$C = \begin{bmatrix} C_{11} & C_{12} & C_{13} & 0 & 0 & 0 \\ C_{12} & C_{22} & C_{23} & 0 & 0 & 0 \\ C_{13} & C_{23} & C_{33} & 0 & 0 & 0 \\ 0 & 0 & 0 & C_{44} & 0 & 0 \\ 0 & 0 & 0 & 0 & C_{55} & 0 \\ 0 & 0 & 0 & 0 & 0 & C_{66} \end{bmatrix} \quad (2.18)$$

The orthotropic stiffness matrix is made up of 9 independent constants. Orthotropic materials have reflective symmetry about the three major planes of the coordinate system. Although only two reflective symmetries are used in the derivation of the stiffness matrix, the third symmetry is a result of the previous two operations. Due to the constraint put on the stiffness matrix, it is not possible to have a reflective symmetry about only two out of three planes that are orthogonal.

Continuing on, by invoking a rotational symmetry of 90° about the x_3 -axis, you can achieve a further reduction. This is done using the $M_{A\frac{\pi}{2}}$ matrix and the equation

$$C = M_{A\frac{\pi}{2}}^T C M_{A\frac{\pi}{2}} \quad (2.19)$$

Following the same procedure as in following steps, the resulting matrix is that of a tetragonal material.

$$C = \begin{bmatrix} C_{11} & C_{12} & C_{13} & 0 & 0 & 0 \\ C_{12} & C_{11} & C_{13} & 0 & 0 & 0 \\ C_{13} & C_{13} & C_{33} & 0 & 0 & 0 \\ 0 & 0 & 0 & C_{44} & 0 & 0 \\ 0 & 0 & 0 & 0 & C_{44} & 0 \\ 0 & 0 & 0 & 0 & 0 & C_{66} \end{bmatrix} \quad (2.20)$$

Tetragonal materials have six independent material constants. This reduction is due to the properties along the x_1 and x_2 -axis being equivalent. This causes the axial terms C_{11} and C_{22} to be equivalent and the shear terms in the $x_1 x_2$ plane (C_{13} and C_{23} as well as C_{44} and C_{55}) to be equivalent.

Further reduction can be done to achieve the remaining two classes of anisotropic materials (cubic and transversely isotropic) and the isotropic stiffness matrix, however this is not of interest for applying to FDM materials as the symmetries seen in the material cannot achieve this level of simplicity.

2.3.2. Failure and Yield Theories

In engineering, a number of failure criteria have been developed over the years as tools for predicting what stress states will cause a material to fail. These yield and failure theories can be categorized by the material behavior they can accommodate. One of the earliest theories is the Von Mises yield theory [34]. This theory states that when the “Von Mises stress” (σ_{vm}) is equal to the yield stress, the material will yield and cause permanent deformation. This can be seen in equation form as,

$$\sigma_{vm} = \sigma_y = \sqrt{3J_2} \quad (2.21)$$

Where σ_y is the yield in any orientation which can be determined by a single unidirectional material test, and J_2 is the second invariant of the deviatoric stress tensor. The Von Mises stress can be expressed in the Cauchy stress tensor terms as,

$$\sigma_{vm} = \sqrt{0.5 [(\sigma_{11} - \sigma_{22})^2 + (\sigma_{22} - \sigma_{33})^2 + (\sigma_{33} - \sigma_{11})^2 + 6(\sigma_{23}^2 + \sigma_{31}^2 + \sigma_{12}^2)]} \quad (2.22)$$

This theory is limited however to tensile –compressive symmetric isotropic materials and predicts yielding for ductile materials.

An extension of the Von Mises theory was presented by Drucker and Prager to help develop a theory for the behavior seen in soil mechanics [35]. This theory incorporates the first invariant of the stress tensor in order to implement a pressure dependence. The equation form of this theory is

$$\alpha I_1 + J_2^{1/2} = k \quad (2.23)$$

Where α and k are positive constants determined by experimentation. When $\alpha = 0$ the theory is equal to the Von Mises theory. Unlike the Von Mises theory, the Drucker-Prager theory can be made to

accommodate tensile-compressive asymmetric materials. The theory can be written in terms of the max tensile and compressive strengths of a material

$$3\sqrt{3} \frac{\sigma_c - \sigma_t}{\sigma_c + \sigma_t} I_1 + J_2^{1/2} - \frac{2\sigma_c \sigma_t}{\sqrt{3}(\sigma_c + \sigma_t)} = 0 \quad (2.24)$$

Although the pressure dependence makes Drucker-Prager able to describe many materials, it is still limited to isotropic materials.

Another extension of the Von Mises theory is that of Hill done in 1948 [36]. The Hill criteria was developed to capture the behavior of single crystal metals. This means it is meant for orthotropic materials. To do this, Hill added a coefficient in front of each term of the Von Mises theory (F, G, H, L, M, N). In equation form this is written as

$$[F(\sigma_{22} - \sigma_{33})^2 + G(\sigma_{33} - \sigma_{11})^2 + H(\sigma_{11} - \sigma_{22})^2 + 2(L\sigma_{23}^2 + M\sigma_{31}^2 + N\sigma_{12}^2)] = 1 \quad (2.25)$$

Where

$$F = \frac{1}{2} \left[-\frac{1}{\sigma_{1t}^2} + \frac{1}{\sigma_{2t}^2} + \frac{1}{\sigma_{3t}^2} \right], \quad G = \frac{1}{2} \left[\frac{1}{\sigma_{1t}^2} - \frac{1}{\sigma_{2t}^2} + \frac{1}{\sigma_{3t}^2} \right], \quad H = \frac{1}{2} \left[\frac{1}{\sigma_{1t}^2} + \frac{1}{\sigma_{2t}^2} - \frac{1}{\sigma_{3t}^2} \right] \quad (2.26)$$

$$L = \frac{1}{2} \left[\frac{1}{\tau_{23}^2} \right], \quad M = \frac{1}{2} \left[\frac{1}{\tau_{31}^2} \right], \quad N = \frac{1}{2} \left[\frac{1}{\tau_{12}^2} \right] \quad (2.27)$$

$\sigma_{1t}^2, \sigma_{2t}^2, \sigma_{3t}^2$ represent the failure strength in the 1,2,3-axis respectively and $\tau_{23}^2, \tau_{31}^2, \tau_{12}^2$ are the failure strength in the three pure shear states. This theory allows for orthotropic materials but does not allow for tensile-compressive asymmetry.

In 1971 Steven Tsai and Edward Wu presented a relatively simple failure criteria which was developed for composite materials [37]. It uses two stress tensors with two matrices of material constants such that failure is predicted when the scalar sum is equal to one. This takes the form

$$F_i \sigma_i + F_{ij} \sigma_i \sigma_j = 1 \quad (2.28)$$

The interesting feature of this theory is that it satisfies the same invariance conditions as the stiffness matrix. This means the constant matrices can be simplified in the manner by applying symmetries. For the orthotropic assumption,

$$F_{ij} = \begin{bmatrix} F_{11} & F_{12} & F_{13} & 0 & 0 & 0 \\ F_{12} & F_{22} & F_{23} & 0 & 0 & 0 \\ F_{13} & F_{23} & F_{33} & 0 & 0 & 0 \\ 0 & 0 & 0 & F_{44} & 0 & 0 \\ 0 & 0 & 0 & 0 & F_{55} & 0 \\ 0 & 0 & 0 & 0 & 0 & F_{66} \end{bmatrix} \quad 2.29$$

And

$$F_i = \begin{bmatrix} F_1 \\ F_2 \\ F_3 \\ 0 \\ 0 \\ 0 \end{bmatrix}$$

Which results in the simplified failure criteria,

$$\begin{aligned} F_1 \sigma_1 + F_2 \sigma_2 + F_3 \sigma_3 + F_{11} \sigma_1^2 + F_{22} \sigma_2^2 + F_{33} \sigma_3^2 + F_{44} \sigma_4^2 + F_{55} \sigma_5^2 + F_{66} \sigma_6^2 \\ + 2F_{12} \sigma_1 \sigma_2 + 2F_{23} \sigma_2 \sigma_3 + 2F_{31} \sigma_3 \sigma_1 \geq 1 \end{aligned} \quad (2.30)$$

Where

$$F_{11} = \frac{1}{XX'} \quad F_{22} = \frac{1}{YY'} \quad F_{33} = \frac{1}{ZZ'} \quad F_{44} = \frac{1}{Q^2} \quad F_{55} = \frac{1}{R^2} \quad F_{66} = \frac{1}{S^2}$$

$$F_1 = \frac{1}{X} - \frac{1}{X'} \quad F_2 = \frac{1}{Y} - \frac{1}{Y'} \quad F_3 = \frac{1}{Z} - \frac{1}{Z'}$$

In this form, X, Y, Z are the uniaxial tensile strengths along the 1,2,and 3-axis respectively, X', Y', Z' are the uniaxial compressive strengths along the 1,2,and 3-axis respectively, and Q, R, S are the strengths in pure shear for the 1,2,and 3-plane respectively. The coupling terms F_{12}, F_{23} , and F_{31} have more complex equations which can be seen below

$$F_{12} = \frac{1}{2N^2} [1 - N(F_1 + F_2) - N^2(F_{11} + F_{22})]$$

$$F_{23} = \frac{1}{2O^2} [1 - O(F_2 + F_3) - O^2(F_{22} + F_{33})]$$

$$F_{31} = \frac{1}{2P^2} [1 - P(F_3 + F_1) - P^2(F_{33} + F_{11})]$$

In these equations N, O, P represent the max strength from a biaxial tensile experiment. Due to the need for these challenging experiments, the Tsai-Wu Criteria is not widely used. It is very powerful though since it can predict failure for tensile-compressive asymmetric materials.

2.4. Knowledge Gaps

In section 2.2, the prior work done in this area was shown to have described the effects of printer settings such as line width, layer height, air gap, etc. in multiple publications and for multiple materials fewer publications have covered the effects of orientations on mechanical properties, and only a single paper [21] attempts to develop a generalized failure criteria. This shows a need for more work in the study of the effects of orientation and failure of FDM materials.

In the work by Cantrell et al. [28], a number of orientations were tested, but only in tension/shear and for ABS and PC plastics. In the work by Guessasma and co-authors[32], a number of orientations

were covered, but only for compression and with a focus on excessive deformation. In the work of Hill and Haugi [21], a mode driven failure criteria was presented, but only for the XY plane of orientations.

An effort to characterize the behavior and failure of a candidate FDM material in both tension and compression in a range of orientations in multiple planes has not yet been done. The advantages of having this all done in a single effort include the elimination in variance in printer setup as parts printed on different printers can have slightly different properties. By keeping all setting equal and only changing orientation you can fully characterize the mechanical response of a material, but the true power lies in being able to run the same experiment on multiple machines to develop a calibration standard for the strength of parts manufactured on a given printer.

CHAPTER 3: EXPERIMENTAL APPROACH

In an effort to address the knowledge gaps, an experimental procedure has been developed in which the printer settings (line width, layer height, temperatures, raster angle, etc.) are kept constant and only the orientation of the specimen to the printer coordinate system is changed. Orientations will be chosen from multiple planes, and specimens will be manufactured and tested in both tension and compression. This procedure will be full described in the following section, including the methods for fabricating the specimens, performing the tensile and compressive experiments, and a mesostructural study to help validate the need for the orientations chosen.

3.1. Specimen Fabrication

For mechanical testing, specimens were manufactured using the Ultimaker 2 FDM printer (Figure 3.1). The Ultimaker 2 is a popular desktop model which features a 0.4 mm nozzle capable of temperature up to 260 °C, a heated bed capable of temperatures up to 100 °C, and a build volume of 223mm x 223mm x 205mm. The printer is equipped with a Bowden extruder setup that uses 2.85 mm filament.

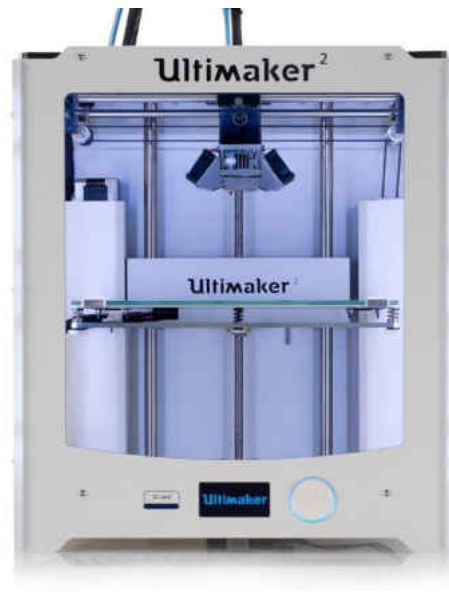


Figure 3.1: Ultimaker 2 FDM 3D printer

Although the Ultimaker is able to print any lower temperature FDM material, PLA was chosen due to its ease of printing, and experience with the use of PLA in prior studies [25, 38]. To maintain consistency between specimens, the same brand, color, and lot of filament was used for all samples. This is crucial due to possible changes in properties that can occur from the different formulations used by separate manufacturers, and even the variance in a single manufacture’s process parameters that occur day to day.

In order to make objects, the printer intakes a file written in the numerical control programming language called G code. This G code file is produced using a slicing software which takes a 3D model, slices it into layers, and creates the needed tool paths and extrusion commands for the printer to replicate the model. The tool path and extrusion commands are controlled using a number of settings in the software such as layer height, line width, print speed, infill type, and infill percentage. To create the G code for the specimens a common open source slicing software called slic3r was used.

To further lock down any variance in manufacturing between specimens, the exact same print settings were used for each specimen. Table 3.1 shows a summary of the most important settings used. A full list of setting can be seen in the Appendix.

Table 3.1: Summary of print settings used

General Print Setting	
Layer height	0.2 mm
Extrusion width	0.4 mm
Perimeters	0
Infill%	100%
infill angle	0°
Print Speed	30 mm/s

For tensile test, ASTM D638 type 4 specimens with a thickness of 3.2 mm were used. For compression tests ASTM D695 block specimens were used. The dimensions for each can be seen in Figure 3.2 and Figure 3.3.

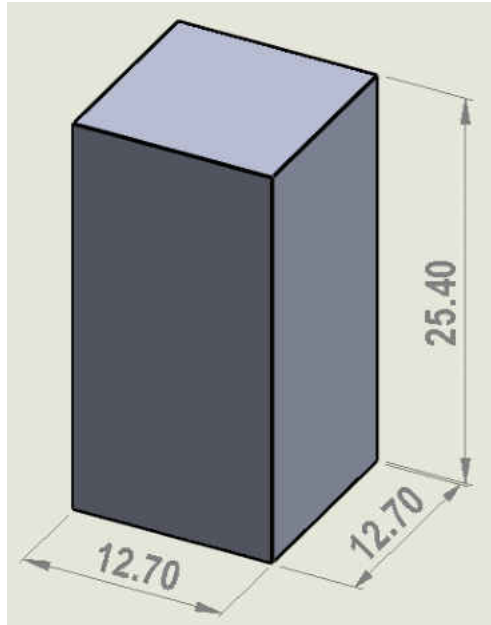


Figure 3.2: Compression specimen dimensions

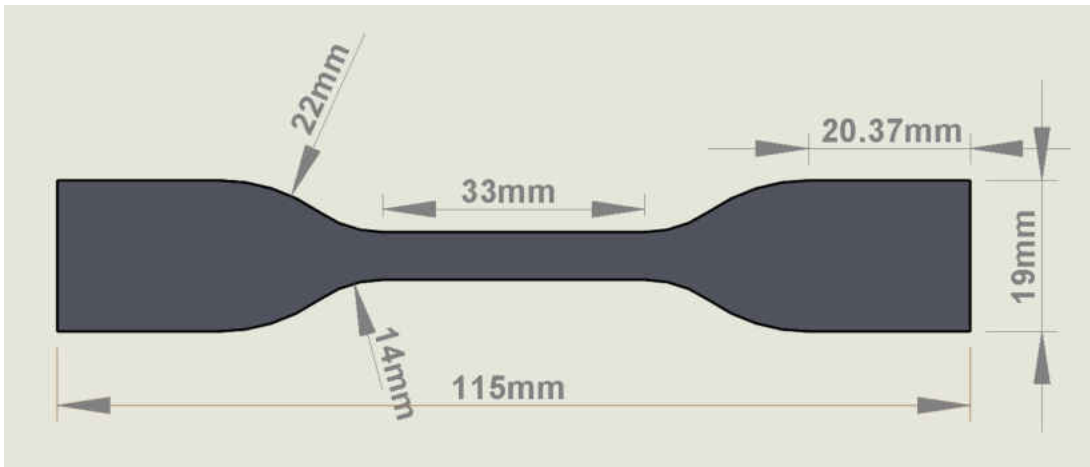


Figure 3.3: Tensile specimen dimensions

Specimens were manufactured in 12 orientations to capture the mechanical properties in the different directions. These include samples in the XY, ZX, and ZX+45° planes. Specimens were positioned from 0° to 90° in increments of 22.5° in each plane. The x, y, and z axis are with respect to the

printers coordinates as shown in Figure 3.4. A diagram of all specimen orientations and can be seen in Figure 3.5.



Figure 3.4: Illustration of the coordinate system of the printer

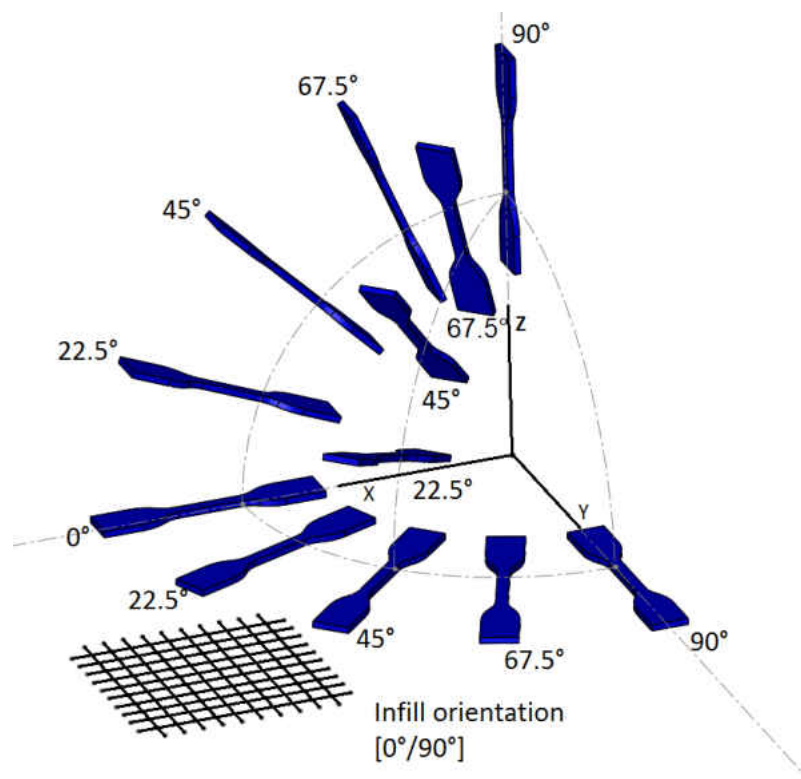


Figure 3.5: Illustration showing the different specimen orientations

In order to reference a specific specimen orientation, the rotations about the major axis from the initial specimen orientation will be used. In this case the initial specimen orientation is the specimen aligned with the x-axis, and all other orientations will be labeled by the non-zero rotations about the axis using the right hand rule to determine positive and negative direction. A few examples are displayed in Figure 3.6 below. Note the initial orientation has 0 rotation about any of the major axis so it will be referred to as the Z+0 orientation.

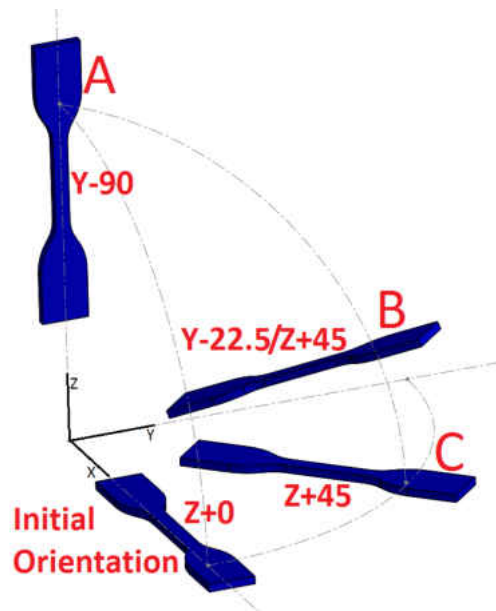


Figure 3.6: Example cases for description of specimen orientation

Example case A has a single rotation about the y-axis of -90° and is referred to as the Y-90 orientation. Example case B undergoes a rotation of -22.5° about the y-axis and 45° about the z-axis meaning the resulting orientation is Y-22.5/Z45. Example case C has a single rotation about the z-axis of 45° and is referred to as the Z+45 orientation.

The specimens in the XY plane (Z+0 thru Z+90) were easily manufactured since they are parallel to the build plate. In order to manufacture the specimens out of the XY plane (Y-22.5 thru Y-90 and Y-

22.5/Z+45 thru Y-90/Z+45 orientations), support material was needed. The FDM process normally allows walls that are at an angle of 45° from the build platform (or less with properly tuned settings) to be easily manufactured. However with the small cross section of the tensile specimens and the continual angle of printing, support material was used for all non XY plane samples. This is illustrated in Figure 3.7 for the 45° example.

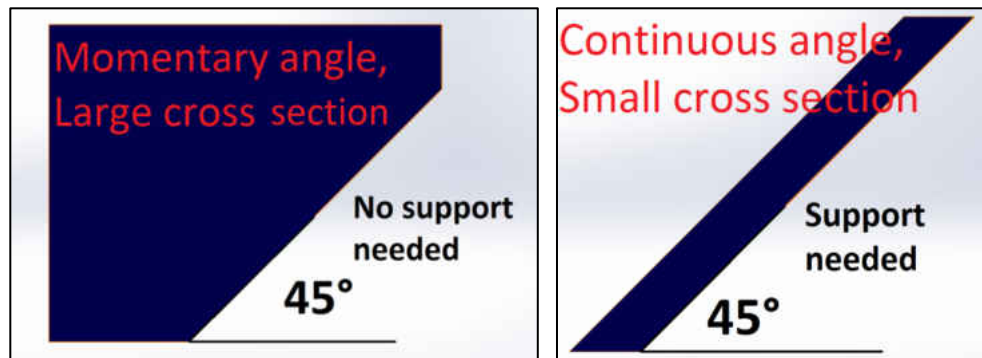


Figure 3.7: Image depicting reasoning for support material use in specimen manufacturing

Support material can either be soluble, meaning it can be removed in a bath of solvent such as water or D-Limonene, or “break away” which is detached manually from the print by prying it away. Break away support was used for simplicity and to avoid the need for a dual extrusion printer. A printed Y-45 sample with support material can be seen in Figure 3.8.

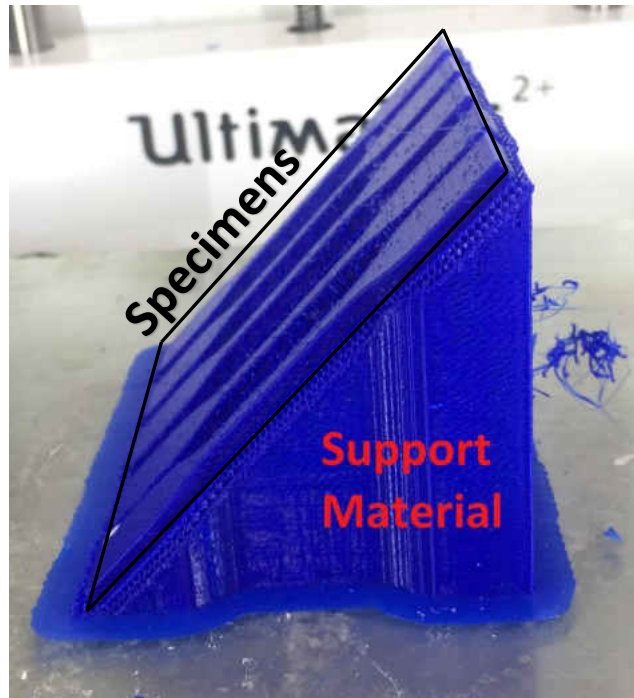


Figure 3.8: Printed Y-45 sample with specimens and support material labeled

3.2. Tensile

The ASTM D638 type 4 specimens after printing were prepared for tensile testing in order to measure the mechanical properties of each orientation. All support material was removed from any specimen from out of the XY plane. Each specimen width and thickness was then measured in the gage section using calipers to get an accurate cross-sectional area before testing.

The specimens were then pull tested on an MTS Insight 5kN electromechanical testing system outfitted with Mark-10 5.3 kN wedge grips (Figure 3.9). To measure displacement an MTS 634.11 extensometer with 1 in. gage length was connected to the specimen using quick attach springs (Figure 3.10).



Figure 3.9: Picture of test setup on MTS load frame



Figure 3.10: Close up of tensile experiment setup

The test were setup using MTS TestWorks software which allows for the control of testing parameters and the capture and exporting of all data collected. For the test, a speed of 1.25 mm/min. was used to ensure all samples would rupture within 30 seconds to 5 minutes as requested by the ASTM D638 standard.

The tensile test data was then processed using a MATLAB code that was developed to analyze the data, and output the mechanical properties for each test. The code then takes the average of the tests at each orientation and calculates the average strength and elastic modulus for each orientation.

3.3. Compression

The ASTM D695 block specimens after printing were prepared for compression testing. Much like the tensile samples, all specimens from out of the XY plane had the support removed. The length and width were measured with calipers.

The compression testing took place on an Instron 3369 test frame with 50kN capacity configured with platens for applying a compressive load. The Instron load frame was used due to the higher load capacity when compared to the MTS load frame used for tensile test. The test were performed without the use of an extensometer. Instead, for displacement the values for the position of the cross head were used.



Figure 3.11: Instron test frame setup for compression testing

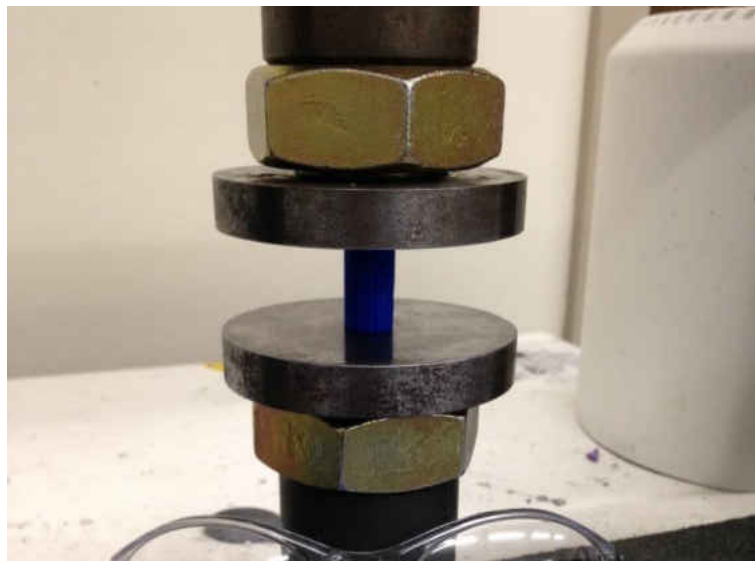


Figure 3.12: Close up of compression testing setup

The Instron Bluehill software was used to control the test and gather and export data. A test speed of 0.1 in./min was used for all test. This is double the 0.05 in/min recommended in the ASTM D695 standard. This was done to reduce test time for the specimens.

All data was processed in MATLAB to gather the average strength and modulus of elasticity for each orientation. Due to the use of crosshead position to measure displacement and not an extensometer, toe compensation had to be performed on the stress-strain graphs. The toe compensation was also incorporated into the MATLAB code.

3.4. Mesostructural Analysis

To further understand the effect that orientation can have on the mechanical properties, the mesostructure created in a specimen when oriented in different directions needs to be analyzed. In an effort to visualize the mesostructure, and the symmetries it possesses, a FDM “material cube” was constructed in Solidworks. Figure 3.13 show the dimensions and steps to create a single layer. The trace cross section dimensions correspond to the layer height and line width used for printed. The slotted shape is an estimate of the actual shape when printed and is also the shape used by slic3r to calculate the volume of material to extrude per movement [39]. This cross section is extruded and then patterned to create a single layer of the material cube. This single layer is then stacked in a $0^{\circ}/90^{\circ}$ pattern to create a cube representative of a block of printed material (Figure 3.14). By using the section tool in Solidworks, and orienting the plane of section to a given orientation, it will show the expected cross section of the corresponding specimen.

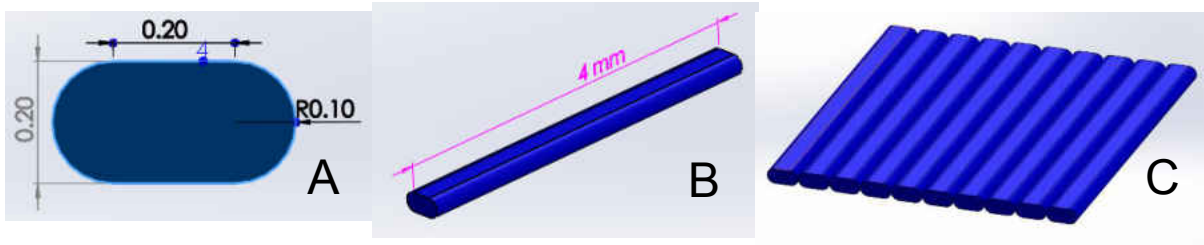


Figure 3.13: Components of Solidworks material cube - (A) Trace cross section (dimensions in mm), (B) Trace, (C) Single layer

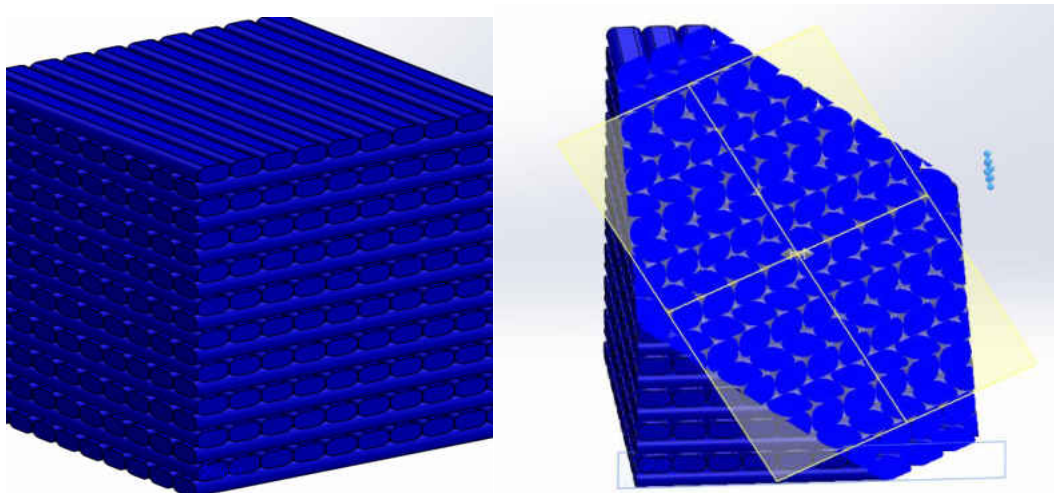


Figure 3.14: Solidworks material cube whole (left) and sectioned using section tool (right)

To verify the Solidworks process of visualizing the mesostructured, and also to view the actual printed mesostructure, samples in each orientation were sectioned and underwent microscopy. This process involves potting the specimens, grinding and polishing them, and then photographing them under a microscope.

To pot the samples, they are put into molds with LECO quick cure epoxy resin. This is a two part epoxy that has a cure time of 1 hour, however to mitigate any error in measuring and mixing the resin and hardener, samples were left to sit for 24 hours to ensure they were fully cured. The samples are then removed from the molds and polished on a Buehler planar grinder. The planar grinder can be seen in Figure 3.15.



Figure 3.15: Buehler planar grinder

The grinder works by having a bottom plate which turns at a user controlled speed. Different abrasive and polishing disks are placed on the stone and can be interchanged. The head, or top of the machine, has an attachment for the sample holder jig. It spins at a constant 60 rpm and can be set to turn with (comp.) or against (contra.) the bottom plate. The head most importantly applies a set downward force on the sample holder.

When polishing samples, multiple steps are used to go from a rough to fully polished surface. These steps start with a high particle size abrasive disk and end with a polishing cloth combined with 50 nm alumina particle polishing compound. A table of all steps in order can be seen below. This is based off of a recommended procedure for polymer sample preparation from [40]. The time for each step was increased to ensure the elimination of remnant scratches from the previous steps.

Table 3.2: Grinding and polishing steps for polymer sample preparation

Surface	Abrasive	Load lbf. /sample	Base Speed (rpm)/Direction*	Time (min:sec)
Sandpaper disc	320- (P400) grit SiC water cooled	4	200-250 Contra	Until Plane
Sandpaper disc	400- (P600) grit SiC water cooled	4	200-250 Contra	4:00
Sandpaper disc	600- (P1200) grit SiC water cooled	4	200-250 Contra	4:00
Sandpaper disc	800- (P1500) grit SiC water cooled	4	200-250 Contra	4:00
TriDent Silk style polishing cloth	Diamond paste	5	100-120 Comp.	8:00
MasterTex Felt style polishing cloth	Alumina suspension	3	100-120 Contra	8:00

* **Comp = Complimentary (platen and specimen holder both rotate in the same direction)**
 * **Contra = Contrasting (platen and specimen holder rotate in opposite directions)**

After polishing, the samples are sonicated to remove any remaining alumina particles that can become built up in the voids of the material structure. Once the alumina is removed, pictures are taken using an AmScope stereoscope with a USB camera attached.

The results showed good agreement between the Solidworks modeled cross sections and the photographed cross sections of the polished samples. Preliminary results show a symmetry between the Z+0 and Z+90 orientations, as well as the Z+22.5 and Z+67.5. Figure 3.16 through Figure 3.26 show the comparisons of the solidworks model and the photographed cross sections for each plane. As can be observed from the array of figures, the different orientations display very unique cross sections. This emphasizes the need for testing in multiple orientations, including the off-axis plane, ZX+45.

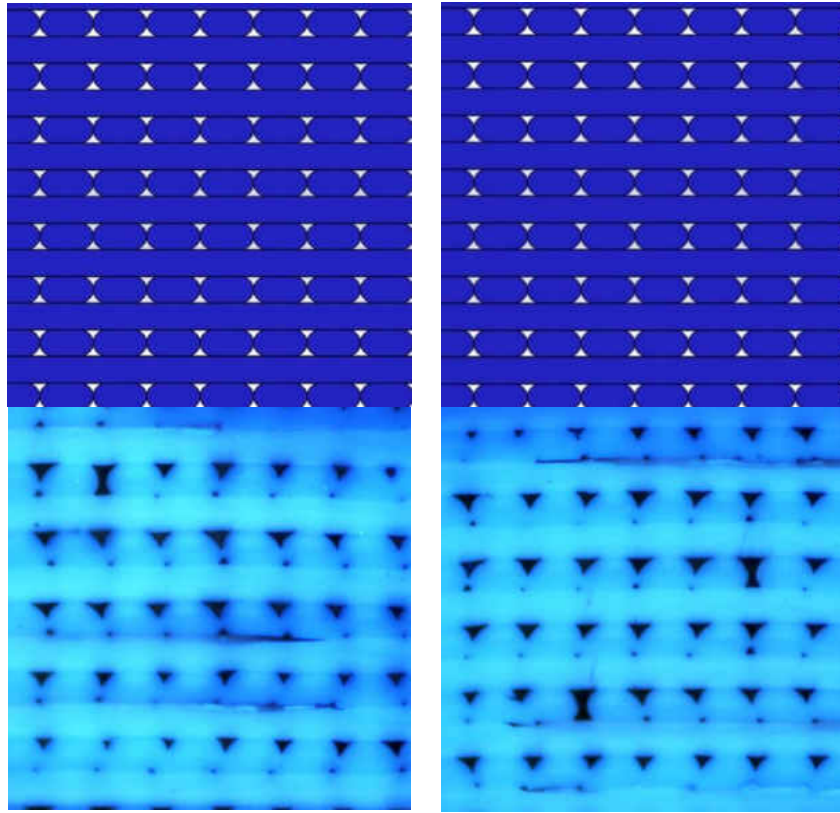


Figure 3.16: Z+0 cross section (left top and bottom) and Z+90 cross section (right top and bottom)

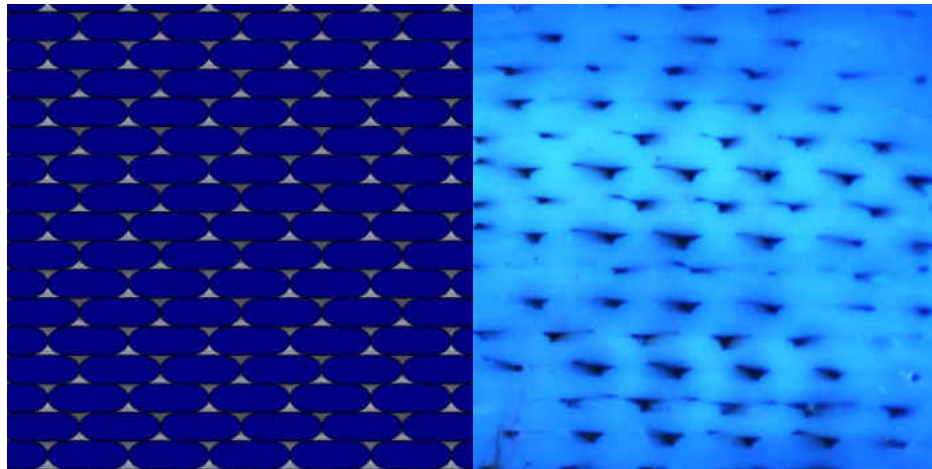


Figure 3.17: Z+45 cross section

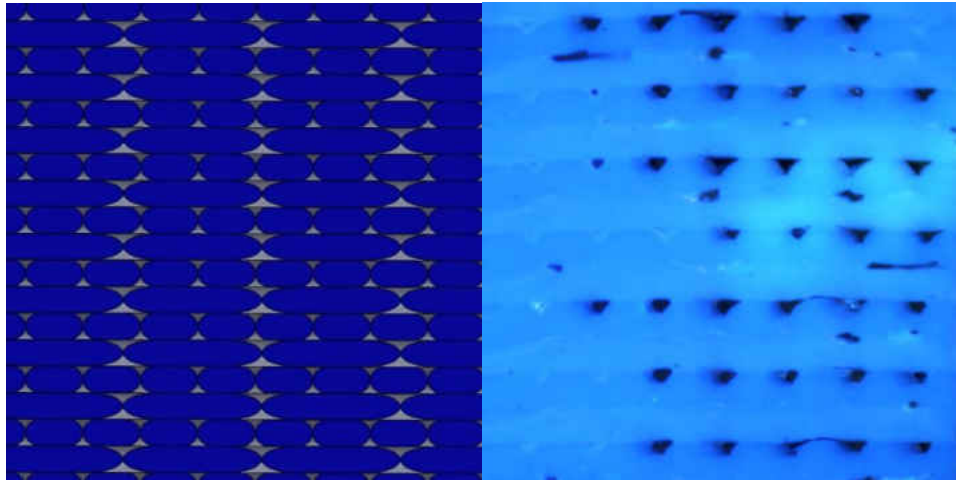


Figure 3.18: Z+22.5 cross section

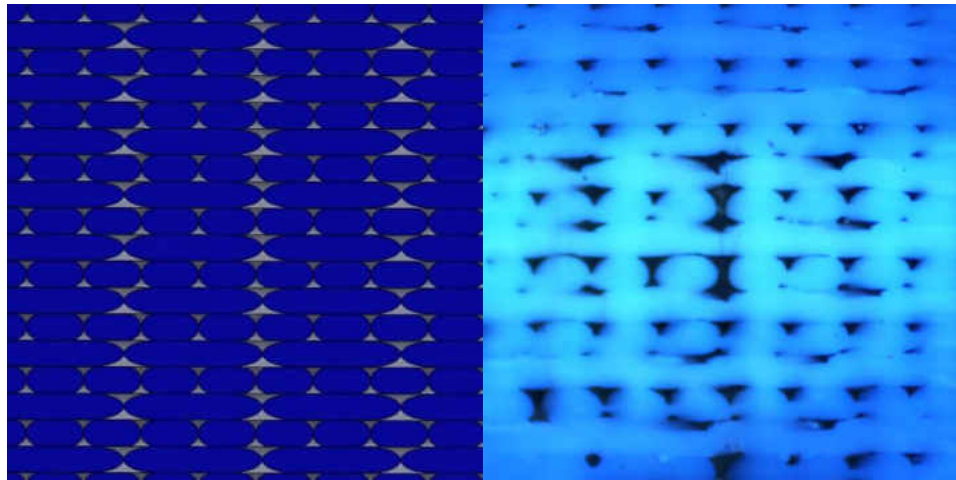


Figure 3.19: Z+67.5 cross section

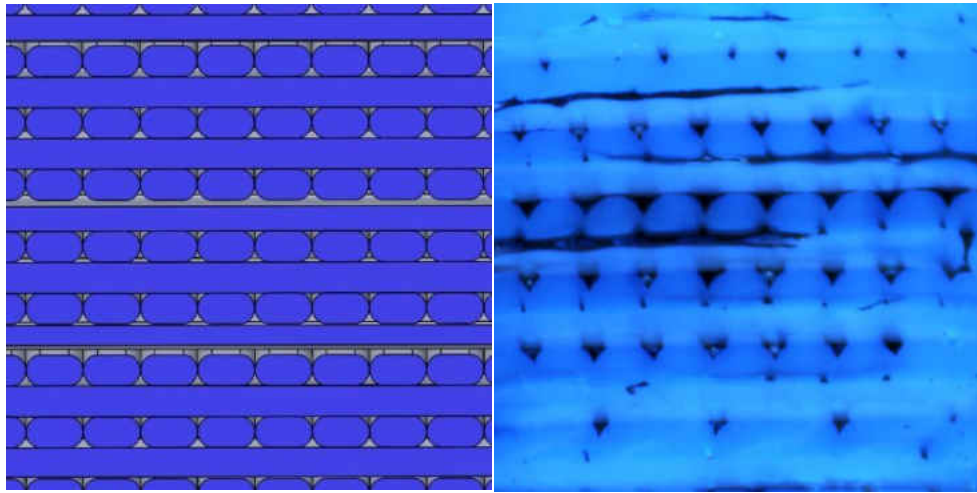


Figure 3.20: Y-22.5 cross section

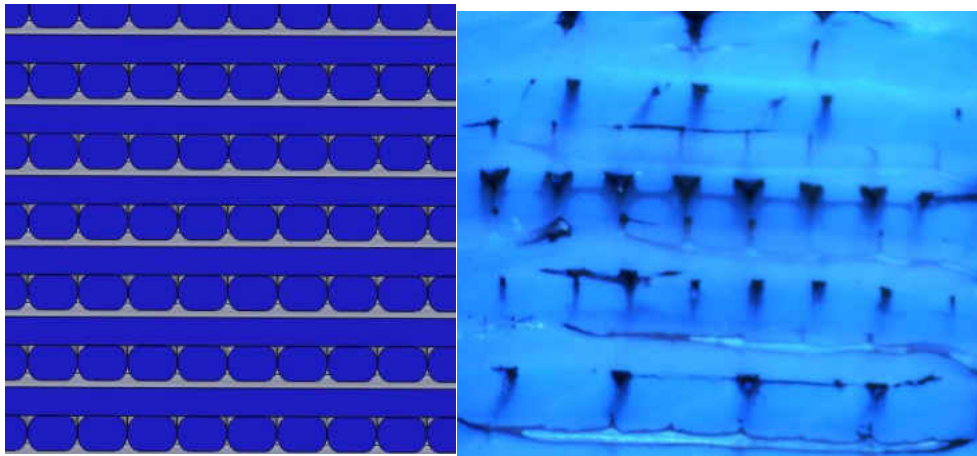


Figure 3.21: Y-45 cross section

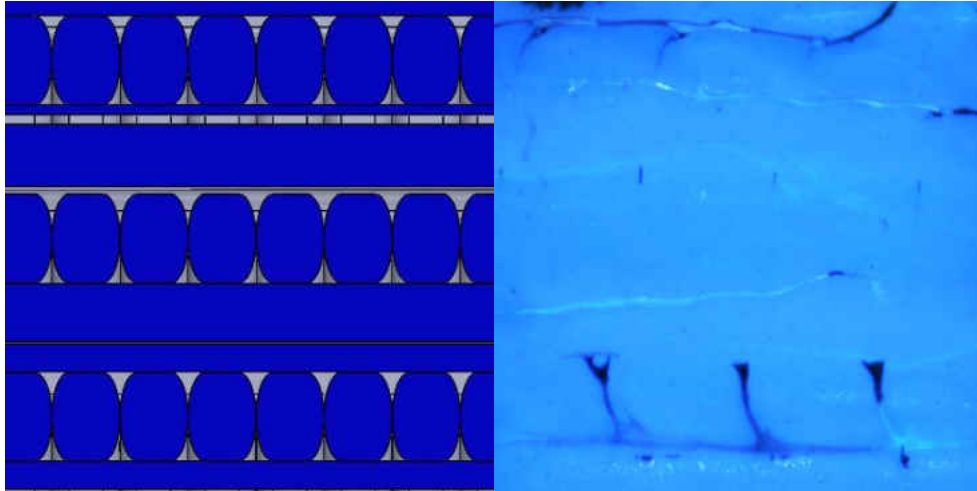


Figure 3.22: Y-67.5 cross section

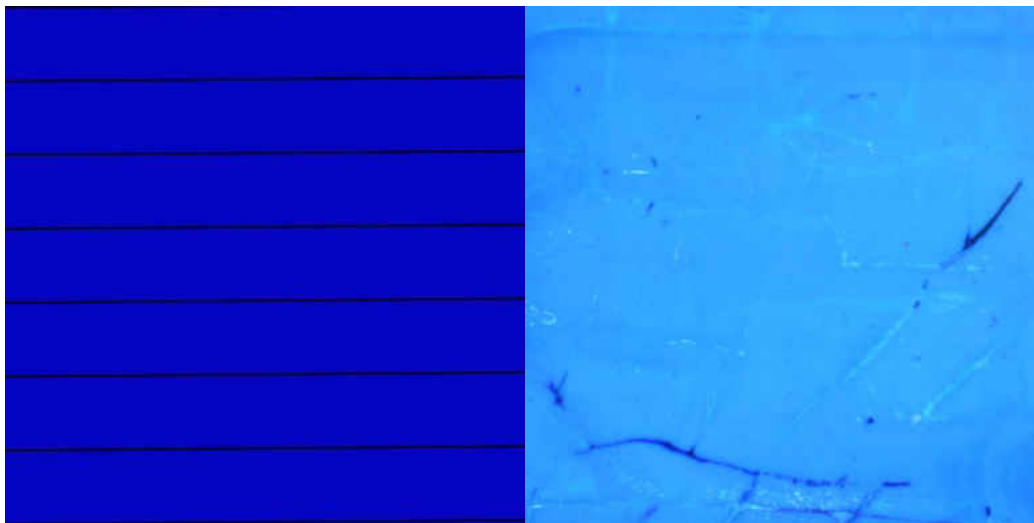


Figure 3.23: Y-90 cross section

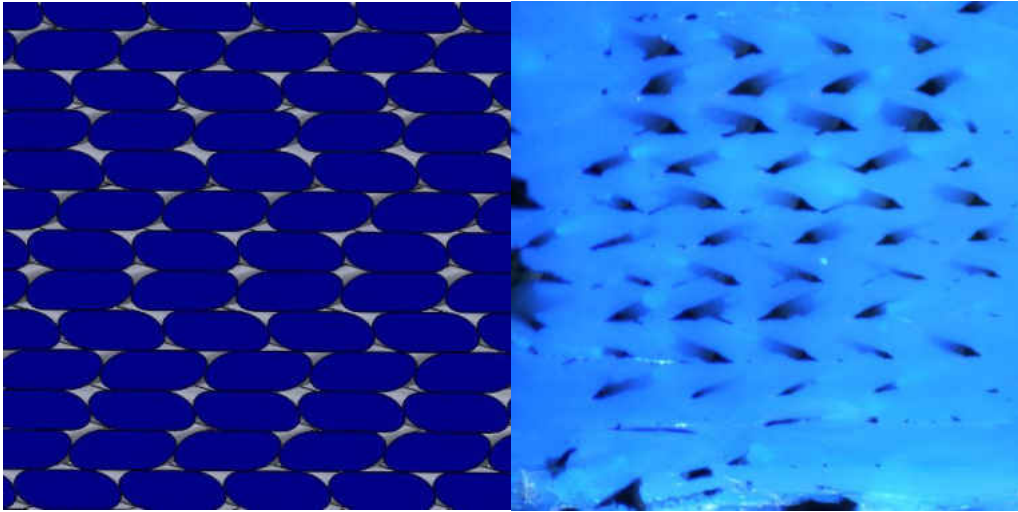


Figure 3.24Y-22.5/Z+45 cross section

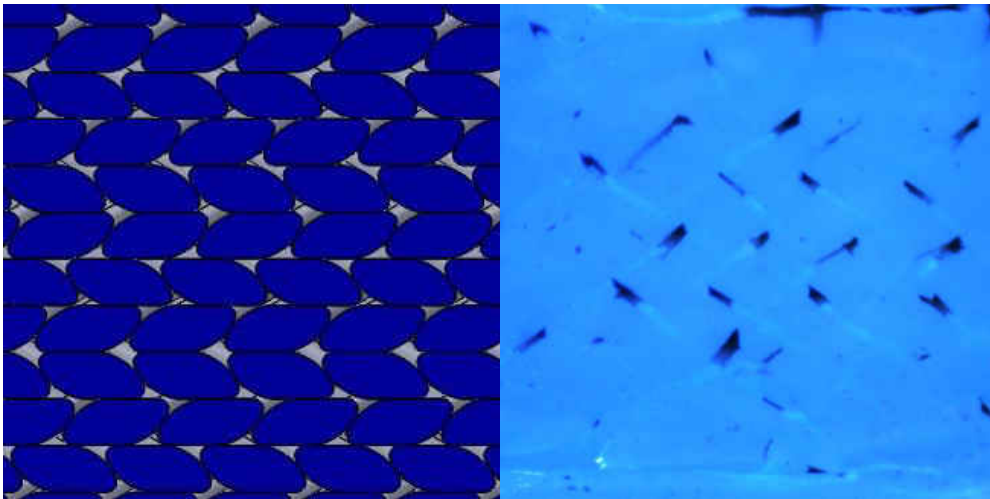


Figure 3.25: Y-45/Z+45 cross section

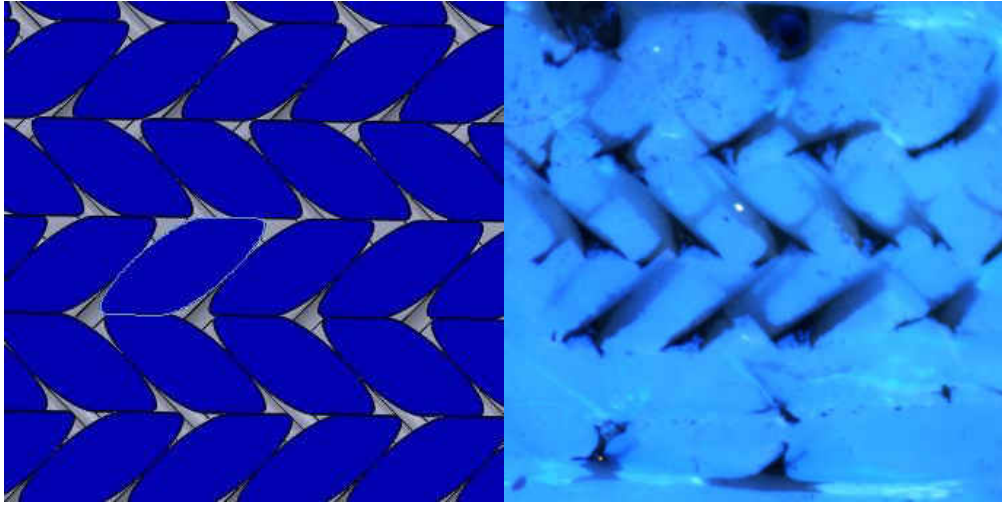


Figure 3.26: Y-67.5/Z+45 cross section

CHAPTER 4: EXPERIMENTAL RESULTS

4.1. Tensile Testing

Tensile experiments were performed on four specimens printed in each of the twelve orientations. From these experiments, the ultimate tensile strength (UTS) and elastic modulus have been calculated. In order to analyze the results, they have been separated by the plane in which they were printed. The XY plane consist of samples in the Z+0 to Z+90 orientations. The ZX plane consist of samples in the Z+0 and Y-22.5 to Y-90 orientations. ZX+45 plane consist of samples in the Z+45, Y-22.5/Z45 to Y-67.5/Z45 and Y-90 orientations. Results for the Z+0, Z+45, and Y-90 orientations appear in multiple sections since they lay at the intersection of two planes.

In order to better understand the results, samples from various orientations were examined for failure modes and mechanisms. For the tensile specimens this was done by examining the failure surfaces under a microscope and photographing them. Features of the fracture surface and exposed mesostructure are discussed with respect to their role in fracture.

4.1.1. Tensile XY Plane Results

The XY plane specimens consist of stacked layers that are parallel to the loading direction. This means the load is in plane with the infill and the load is carried by the traces of the infill which consist of alternating 0° and 90° layers. In the Z+0 orientation, the load is directly along the 0° layers and perpendicular to the 90° layers. In the Z+90 orientation the opposite is true and the load is parallel to the 90° and perpendicular to the 0° infill layers. The Z+22.5 and Z+67.5 layers share this same symmetry in which the load on the 0° infill for one is equal to the load on the 90° infill on the other and vice versa. This leads to a symmetry about the 45° plane in which the direction of the load with respect to the infill is equal on both the 0° and 90° degree infill.

The representative stress strain graphs can be seen in Figure 4.1. This shows little plastic deformation for all samples, and near brittle behavior.

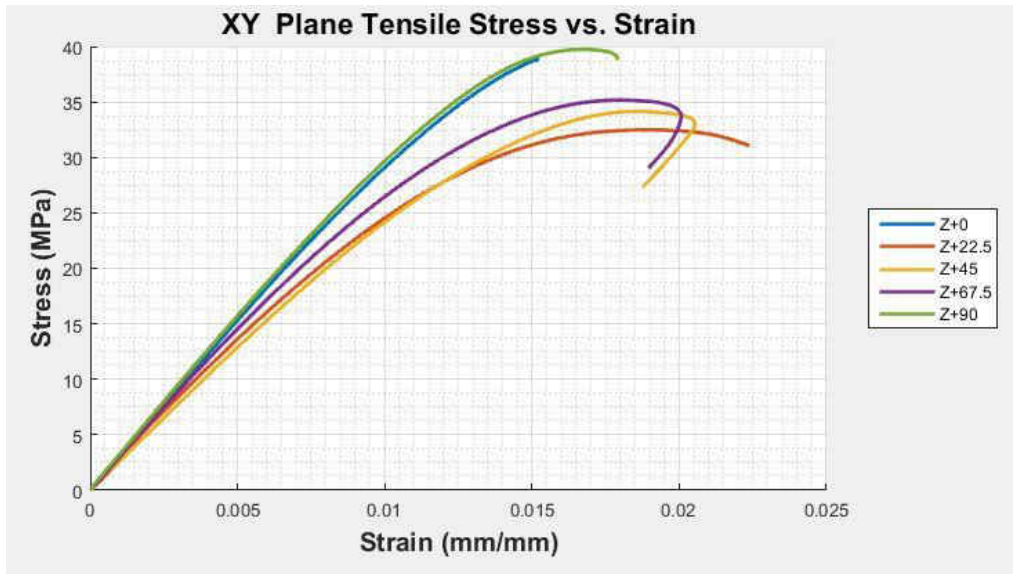


Figure 4.1: Representative stress-strain curves for XY plane specimens in tension

The results from the XY plane tensile strength can be seen in Table 4.1 and Figure 4.2. The results show the Z+0 and Z+90 to be very close as predicted. The Z+22.5 and Z+67.5 orientations do not match quite as well, but still fall within the 95% confidence interval of each other. The Z+45 orientation has been shown to be weaker than the Z+0 or Z+90 in past experiments [17, 41] for ABS and Polyether ether ketone (PEEK) specimens respectively. This also held true for PLA in these experiments.

Table 4.1: Ultimate tensile strength versus orientation in XY plane

Ultimate Strength vs. Orientation in XY Plane					
Degree	0 Degrees	22.5 Degrees	45 Degrees	67.5 Degrees	90 Degrees
Ultimate Strength	38.384	32.444	33.132	34.260	39.669
95% CI	1.000	0.936	1.831	2.204	1.985

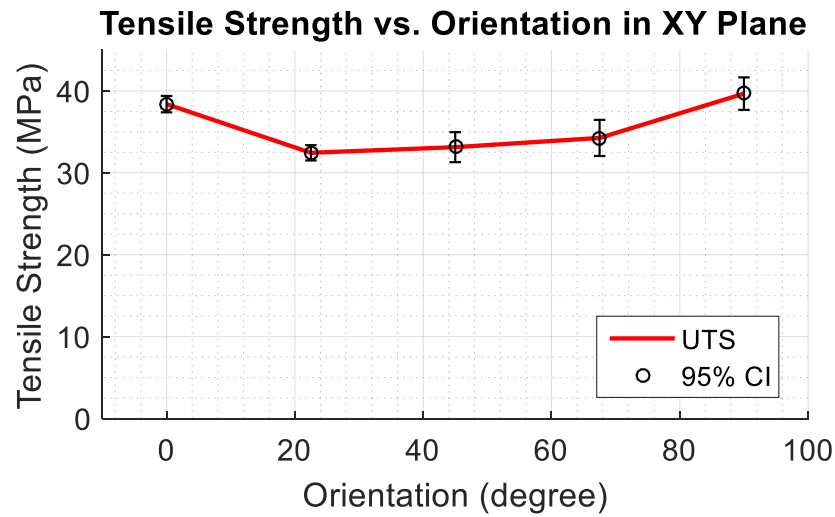


Figure 4.2: Tensile strength for XY plane samples

The elastic modulus results from the experiments can be seen in Table 4.2 and Figure 4.3. The elastic modulus follows roughly the same trend at the tensile strength. Once again the Z+0 and Z+90, and the Z+22.5 and Z+67.5 nearly match. The Z+45 has the lowest elastic modulus. This aligns with past publications that show Z+0 specimens to have greater elastic modulus than Z+45 specimens [28, 42].

Table 4.2: Elastic modulus versus orientation in XY plane

Elastic Modulus vs. Orientation in XY Plane					
Degree	0 Degrees	22.5 Degrees	45 Degrees	67.5 Degrees	90 Degrees
Elastic Modulus	3055.527	2585.438	2446.893	2758.835	3146.136
95% CI	70.976	111.439	116.268	224.265	36.494

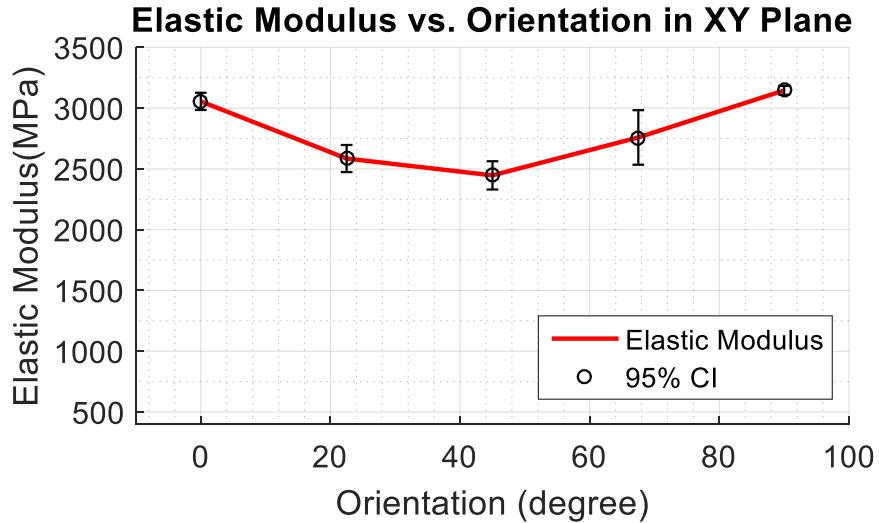


Figure 4.3: Elastic Modulus for XY plane samples

4.1.2. Tensile ZX Plane Results

The ZX plane orientations start with the Z+0 specimen which has layers parallel to the loading direction and ends with the Y-90 specimen that has layers that are perpendicular to the loading direction. For FDM materials, the weakest feature in a printed structure is the inter layer bonds. These interlayer bonds are not continuous and rely on hot traces being laid down onto a cooler surface to partially melt together in order to form a bond. In the Y-90 orientation, these weak points are experiencing the whole load and this results in low strength.

The representative stress strain graphs can be seen in Figure 4.4. This show brittle behavior and large variation in strength and elastic modulus for different orientations.

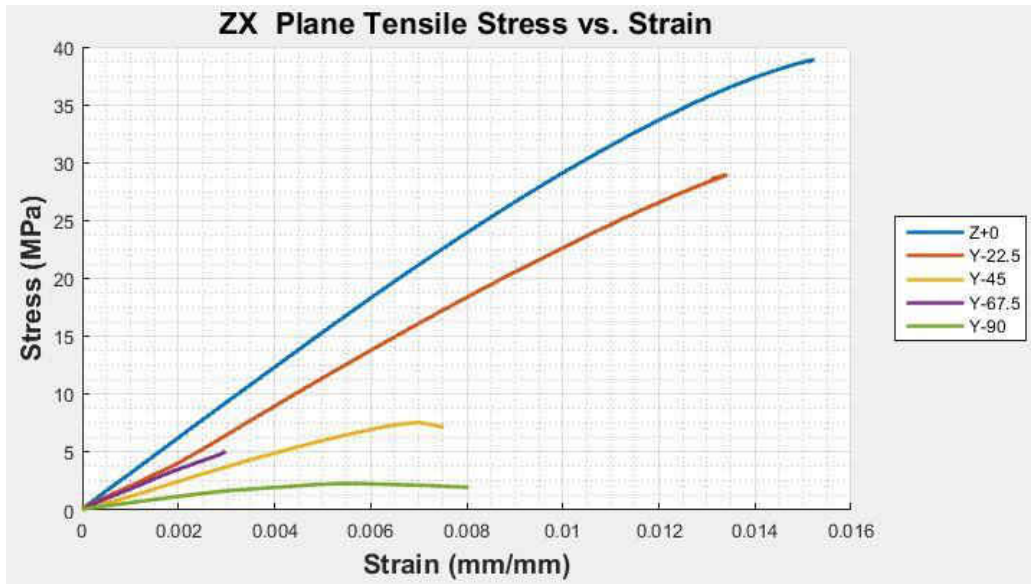


Figure 4.4: Representative stress-strain curves for ZX plane specimens in tension

Table 4.3 and Figure 4.5 show the results of the tensile ZX plane experiments. The Z+0 orientation results were seen in the last section and is one of the strongest orientations for the material in tension. The strength very quickly drops off as the layer get further from parallel with the applied load. The Y-22.5 orientation has a large Confidence interval. This is due to there being two specimens that displayed high strength and two specimens that displayed much lower strength. This hints at possible sensitivity to defects or inconsistent properties since it is in the middle of the very large change in strength from Z+0 to Y-45. As expected, the Y-90 orientation is very weak and the Y-67.5 is only slightly stronger. In general the strength of the Y-90 orientation is very low compared to past papers [22, 25, 26, 28, 43]. This points to very poor interlayer adhesion in the specimens. This can be caused by poor printer setting and is very common in materials printed at too low of a temperature. That being said, the trends seen in the properties are as expected from a layered material.

Table 4.3: Tensile Strength versus orientation in ZX plane

Ultimate Strength vs. Orientation					
Degree	0 Degrees	22.5 Degrees	45 Degrees	67.5 Degrees	90 Degrees
Ultimate Strength	38.384	19.089	6.286	3.524	2.334
95% CI	1.000	15.085	3.128	1.077	1.535

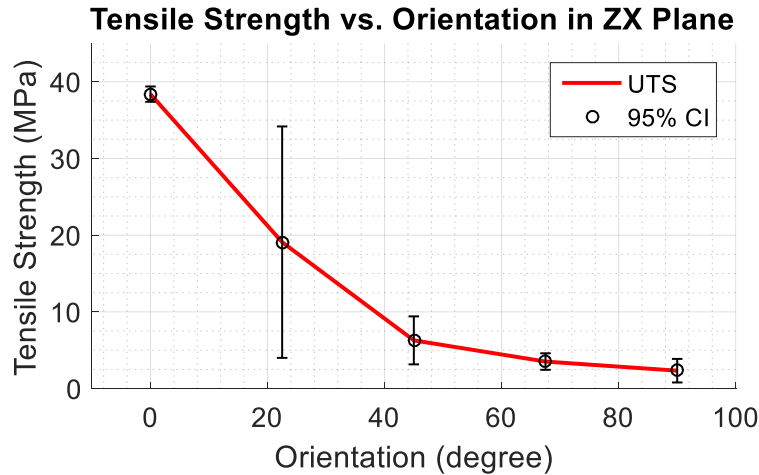


Figure 4.5: Tensile strength for ZX plane samples

The elastic modulus results for the ZX plane can be seen in Table 4.4 and Figure 4.6. They follow roughly the same trend as the tensile strength, but the results display a large amount of variance between the specimens.

Table 4.4: Elastic modulus versus orientation in ZX plane

Elastic Modulus vs. Orientation					
Degree	0 Degrees	22.5 Degrees	45 Degrees	67.5 Degrees	90 Degrees
Elastic Modulus	3055.527	2354.121	1332.840	796.965	636.127
95% CI	70.976	806.242	565.448	670.858	252.823

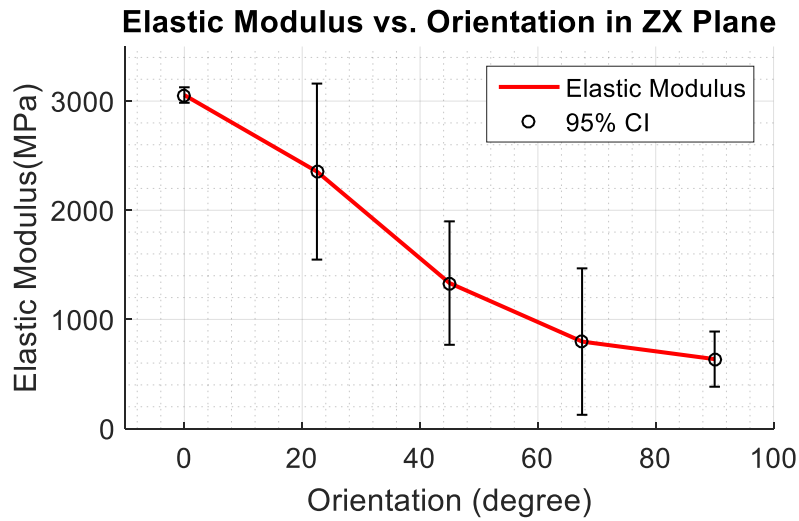


Figure 4.6: Elastic Modulus for ZX plane samples

4.1.3. Tensile ZX+45 Plane Results

The ZX+45 plane include only three unique orientations. These are the Y-22.5/Z+45, Y-45/Z+45, and Y-67.5/Z+45 orientations. These orientations have not been studied before, possibly due to the similarity to the ZX plane. The Z+45 sample is used for the 0° orientation and the Y-90 is used for the 90° orientation. Although the Y-90 sample is 45° rotated from the ZX+45 plane, the rotation about the z- axis should have no effect on the strength since the layers are still perpendicular to the axis of loading. This is backed up by the results from [28].

The representative stress strain graphs can be seen in Figure 4.7. Again this show large variation in strength and elastic modulus with changing orientation.

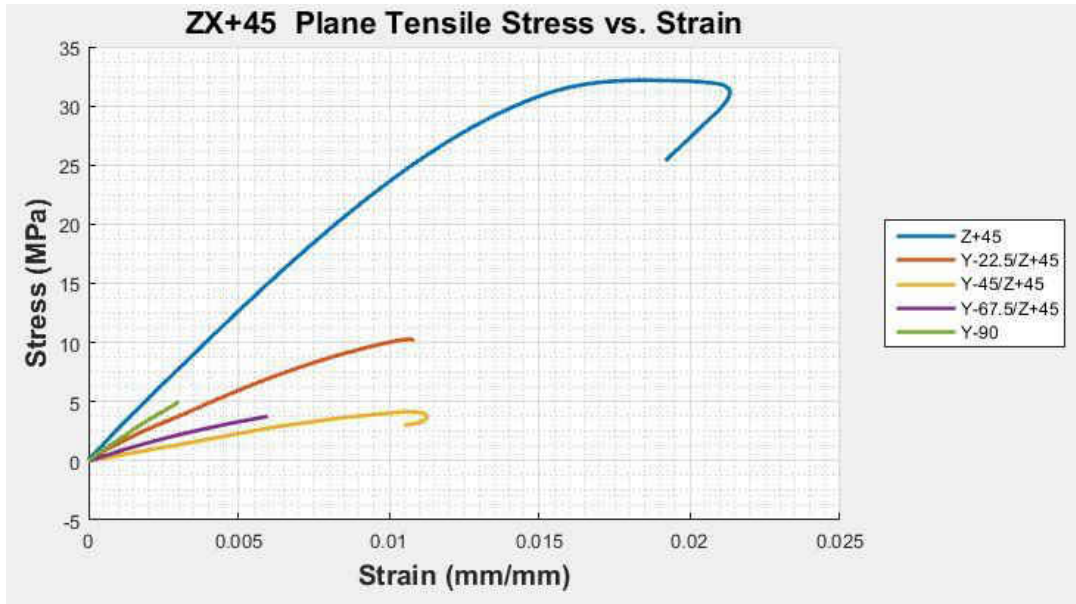


Figure 4.7: Representative stress-strain curves for ZX+45 plane specimens in tension

The ZX+45 plane results show similarity to the ZX plane (Table 4.5 and Figure 4.8). The strength drops off even quicker with increasing orientation. This could be due to the smaller confidence interval and could be a more accurate representation of the strength for Y-22.5 orientations.

Table 4.5: Tensile Strength versus orientation in ZX+45 plane

Ultimate Strength vs. Orientation in ZX+45 Plane					
Orientation	0 Degrees	22.5 Degrees	45 Degrees	67.5 Degrees	90 Degrees
Ultimate Strength	33.132	8.782	4.733	3.983	2.334
95% CI	1.831	3.333	0.568	0.976	1.535

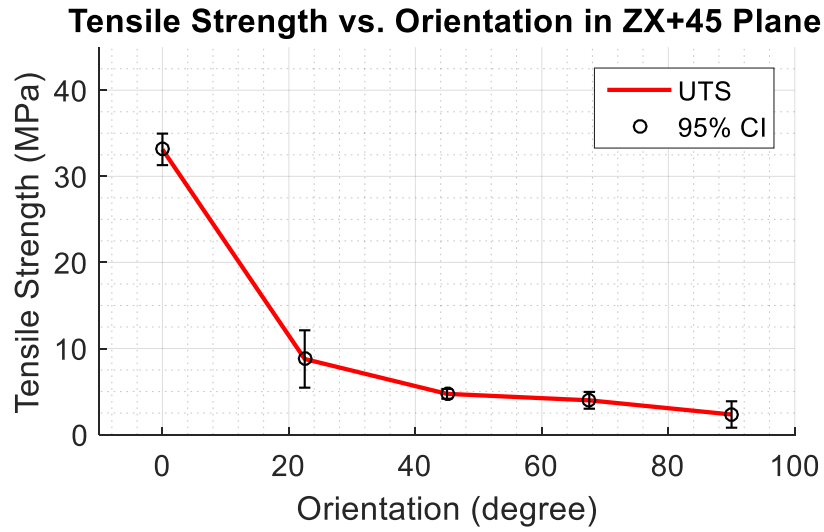


Figure 4.8: Tensile strength for ZX+45 plane samples

The elastic modulus for the ZX+45 plane can be seen in Table 4.6 and Figure 4.9. The Y-22.5/Z+45 specimens have a large confidence interval from varying values from each specimen. The Y-45/Z+45 orientation shows the lowest elastic modulus which does not follow the expected trend.

Table 4.6: Elastic modulus versus orientation in ZX+45 plane

Elastic Modulus vs. Orientation in ZX+45 Plane					
Degree	0 Degrees	22.5 Degrees	45 Degrees	67.5 Degrees	90 Degrees
Elastic Modulus	2446.893	1063.470	541.142	739.247	636.127
95% CI	116.268	804.137	157.375	92.506	252.823

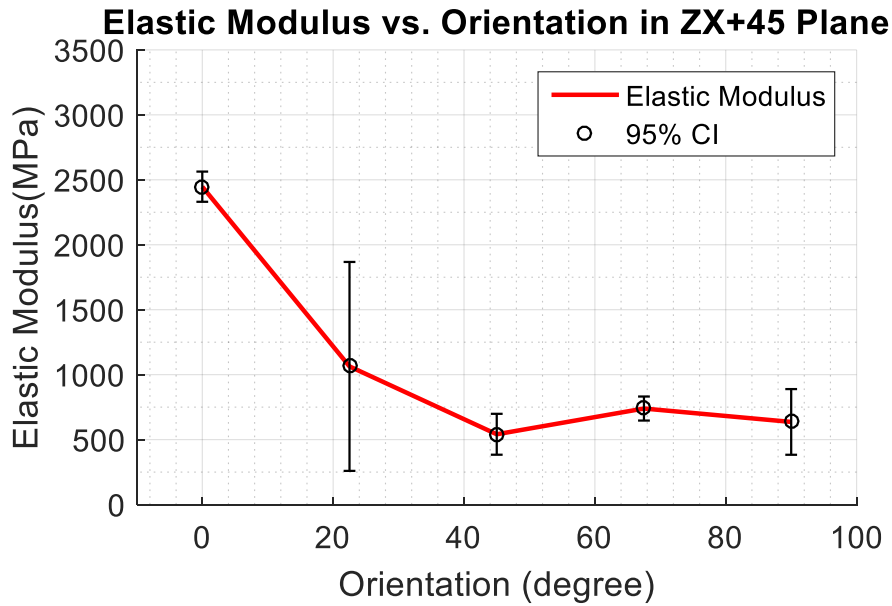


Figure 4.9: Elastic Modulus for ZX+45 plane samples

4.1.4. Tensile Failure Analysis

After testing, tensile specimens were analyzed to determine the mechanisms behind the failure at the different orientations. For the printed specimens, there are a few common sources of failure. These include the debonding of adjacent traces, the debonding of layers, and the tensile failure of traces. In order to understand the trends seen in the tensile strength, it is vital to know which of these mechanisms is driving the failure at each orientation.

In the XY plane, the specimens tend to fracture along the higher of the two infill angles. This is shown in Figure 4.10. It can be seen that the Z+0 and Z+90 orientations both fracture along the 90° direction, the Z+22.5 and Z+67.5 orientations fracture along the 67.5° direction, and the Z+45 samples fracture along the 45° direction.



Figure 4.10: Fractured XY plane specimens

When observing the fracture surface of the Z+0 specimen, a few key features stand out. The red box highlights a typical bond between transverse traces. The white discoloration indicates deformation or tearing upon separation due to good bonding between traces. The yellow box shows poor adjacent trace bonding. The glossy appearance of this trace shows it was not properly bonded to the trace adjacent to it. The red arrow indicates longitudinal traces that have undergone deformation. These traces help to track how the fracture began and propagated. The discoloration and deformation indicates slow crack growth in this area. At some critical localized stress, these deformed traces began to fail. At this point the crack quickly propagated from the left to the right side of the fracture surface. This is indicated by the flat and clean features on the right side of the failure surface which requires higher energy to produce.

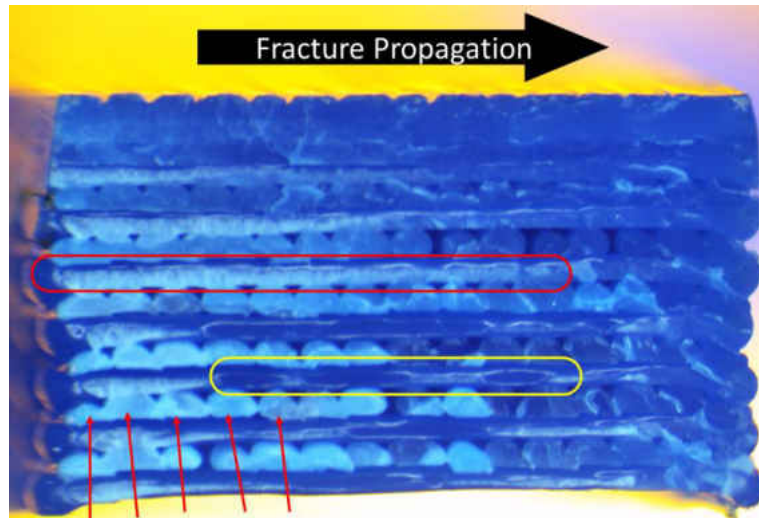


Figure 4.11: Failure surface for Z+0 specimen

The Z+22.5 orientation shows this same behavior (Figure 4.12). Examples of a strong and weak bond are again highlighted with a red box and a yellow box respectively. As seen in Figure 4.10, the fracture follows a diagonal path along the 67.5° transverse traces. The closer look shows that after the diagonal growth, the crack then cuts straight across the specimen leaving a small flat portion on the left side.

The fracture surfaces of both orientations indicate that the main cause of failure is the tensile failure of the traces. It should also be noted that the failure is aided by the poor bonding of transverse traces. Due to the symmetry in the specimens, the Z+0 and Z+90 orientations behave in the same manner, and the Z+22.5 and Z+67.5 orientations do as well.

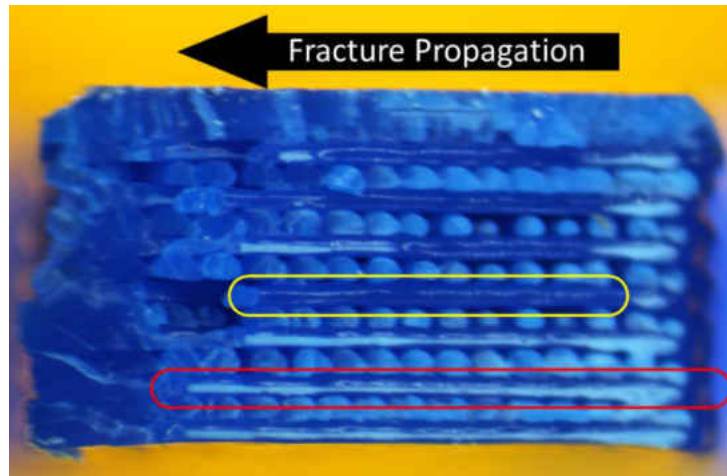


Figure 4.12: Failure surface for Z+22.5 specimen

The Z+45 failure surface, which can be seen in Figure 4.13, shows no obvious failure propagation direction. Only one transverse trace shows signs of good bonding (indicated by the red box). Since the traces are 45° offset from the loading direction, the tensile load is partially transferred into a shear load on the traces. Although all non-zero orientations have some amount of shear, the greatest amount occurs at the Z+45 orientation. This means the traces fail not just by tension, but by a mixed tensile and shear stress. This is supported by the lack of large deformation on the failure surface.

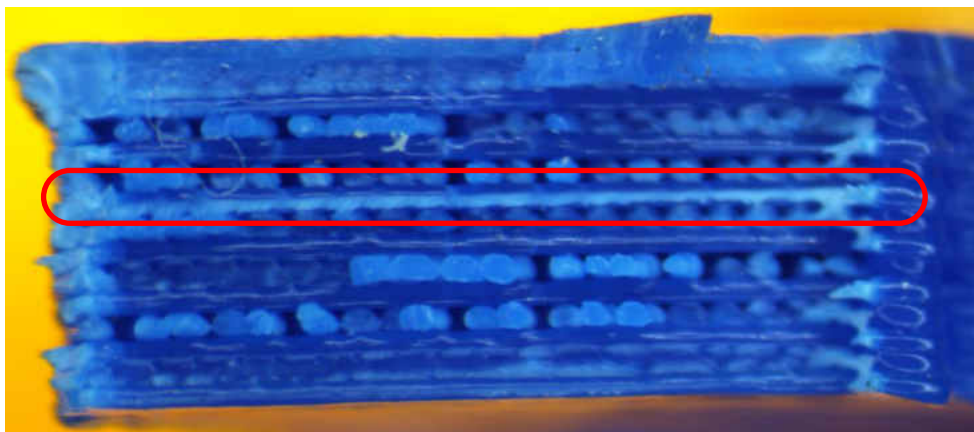


Figure 4.13: Failure surface for Z+45 specimen

The out of XY plane orientations in the ZX and ZX+45 planes have the tendency to fail along the interlayer bonds. As shown in Figure 4.14 and Figure 4.15, this leaves an angled end that corresponds to the specimen's orientation angle about the y-axis. For example, the Y-22.5 specimen has a 22.5° angle to the end.

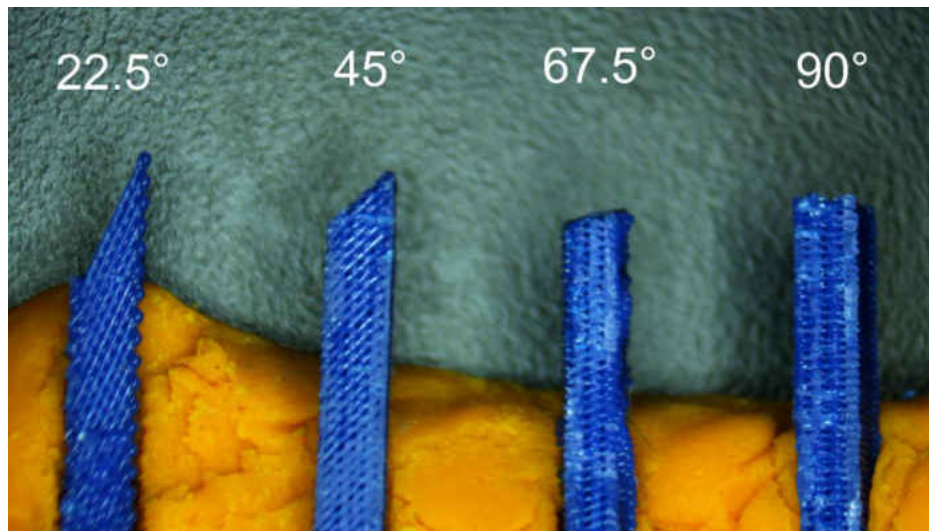


Figure 4.14: Side view of ZX plane specimen failure surfaces

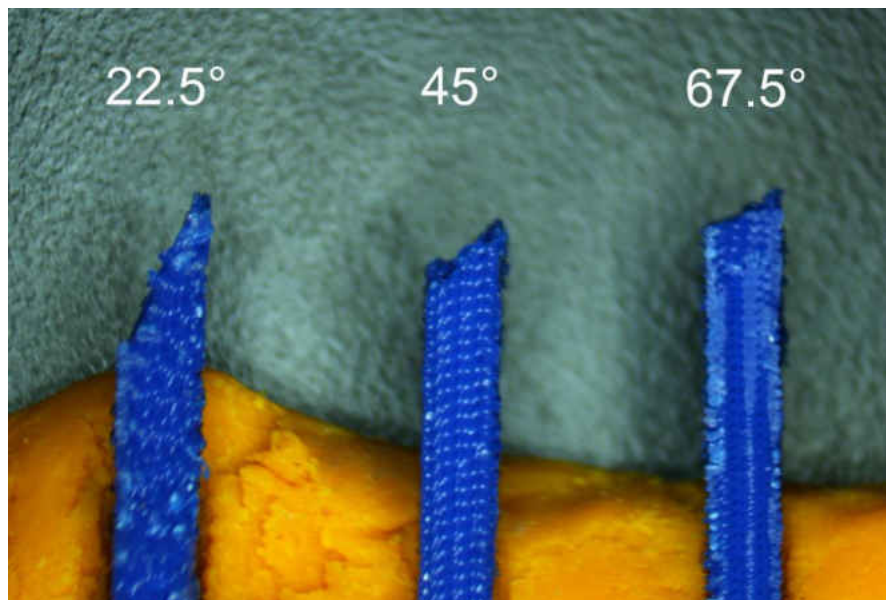


Figure 4.15: Side view of ZX+45 plane specimen failure surfaces

The failure surfaces for the Y-22.5, Y-45/Z+45, and Y-90 orientations can be seen in Figure 4.16, Figure 4.17, and Figure 4.18 respectively. Each of these surfaces show the same result which is that the infill for the out of XY plane samples is not fully solid. The surfaces also show no signs of good interlayer bonding. The surfaces are very smooth with no deformation or marks from the previously attached layer. This correlates well to the low strength seen for the out of ZX plane specimens.

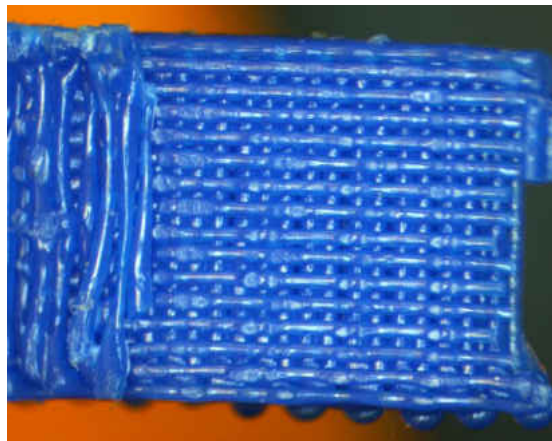


Figure 4.16: Failure surface for Y-22.5 orientation



Figure 4.17: Failure surface for Y-45/Z+45 orientation

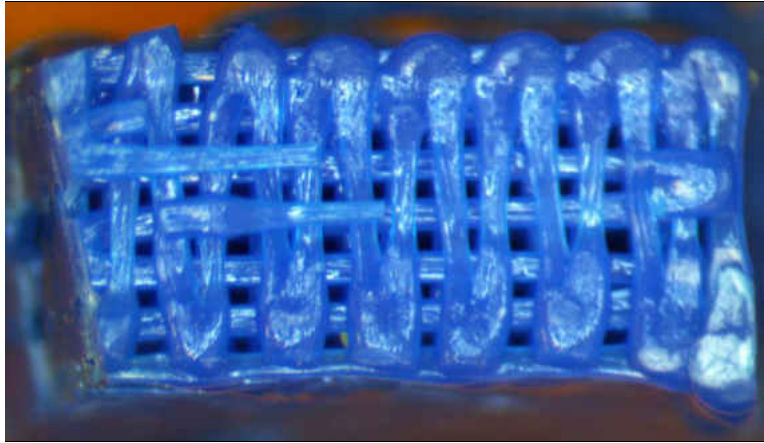


Figure 4.18: Failure surface for Y-90 orientation

4.2. Compression

Compression experiments were performed on four specimens printed in each of the twelve orientations. From these experiments, the compressive strength and elastic modulus have been calculated. Just as the tensile experiments, the result have been separated by the plane in which they were printed. The planes consist of the same orientations from the tensile sections.

Samples from various orientations were observed to determine the failure mechanisms. For compressive samples, the tested samples are only examined to determine failure modes as they do not have exposed fracture surfaces.

4.2.1. Compressive XY Plane Results

In the XY plane, the compressive samples have layers that are parallel to the loading direction. The cross section is the same as the corresponding tensile samples, however the behavior is harder to predict because the printed traces are under compression instead of tension. In compression, the long thin traces are subject to the possibility of buckling which could cause different behavior than seen in the tensile specimens.

The representative stress strain curves can be seen in Figure 4.19. The curves show a similarity between the Z+0 and Z+90, and Z+22.5 and Z+67.5 pairs. The Z+45 samples show a high strength with large amounts of plastic deformation. The Z+0 and Z+90 samples show much less plastic deformation.

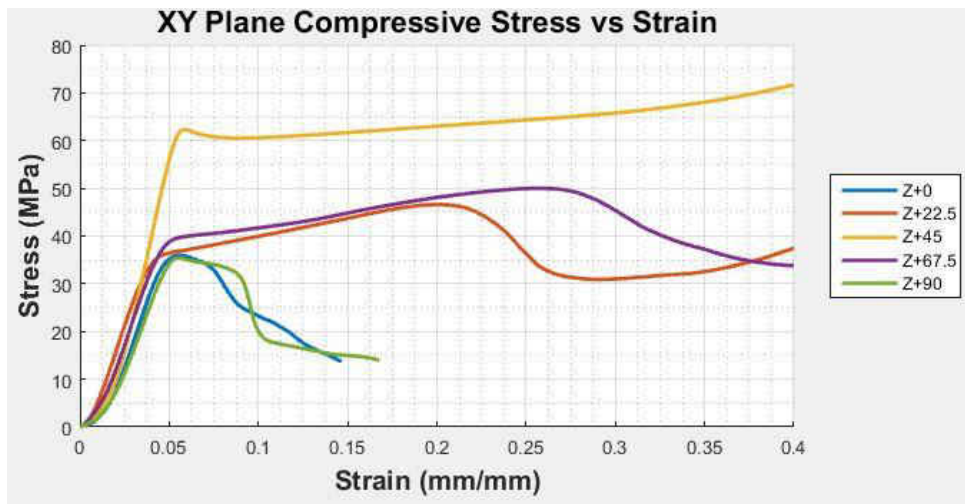


Figure 4.19: Representative stress-strain curves for XY plane specimens in compression

The tabulated results for the compressive strength can be seen in Table 4.7 and Figure 4.20. It displays the same symmetry about the Z+45 orientation as seen in tension. The Z+45 orientation in this case is the strongest orientation and is nearly double the other orientations.

Table 4.7: Compressive strength versus orientation in XY plane

Compressive Strength vs. Orientation					
Degree	0 Degrees	22.5 Degrees	45 Degrees	67.5 Degrees	90 Degrees
Compressive Strength	35.549	36.388	63.638	36.872	34.513
95% CI	0.656	1.790	0.918	2.869	1.463

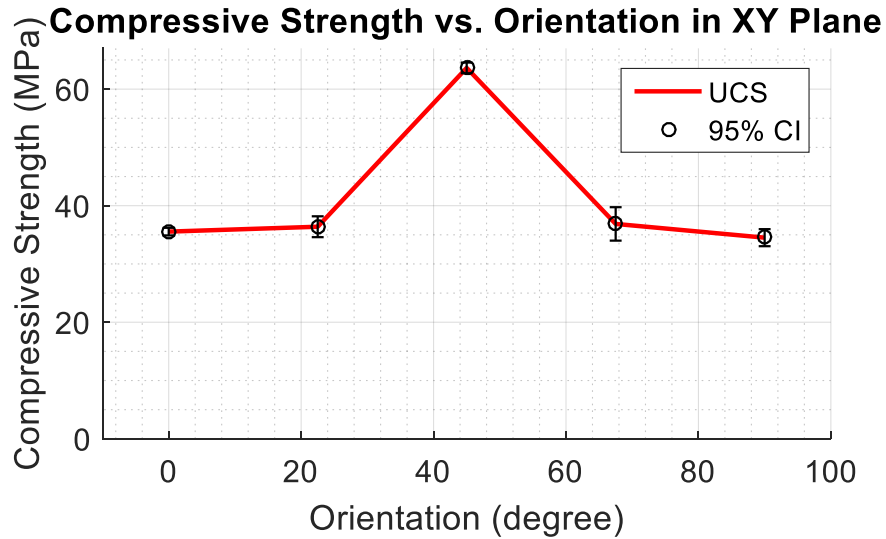


Figure 4.20: Compressive strength for XY plane samples

The elastic modulus results can be seen in Table 4.8 and Figure 4.21. They follow the same trend as the compressive strengths. The Z+90 and Z+67.5 orientations are lower than the Z+0 and Z+22.5 orientations. These are expected to be equal and symmetric. The difference however is not large enough to cause concern and is within the uncertainty of the experiments.

Table 4.8: Elastic modulus versus orientation in compression for XY plane

Elastic Modulus vs. Orientation					
Degree	0 Degrees	22.5 Degrees	45 Degrees	67.5 Degrees	90 Degrees
Elastic Modulus	1018.828	1164.695	1639.213	1004.403	887.598
95% CI	82.123	58.732	29.320	61.778	53.578

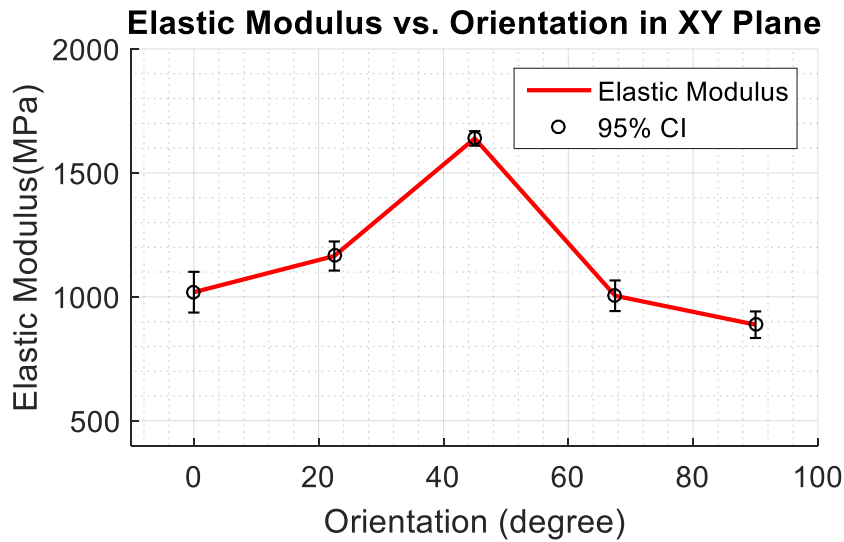


Figure 4.21: Elastic modulus for XY plane compression samples

4.2.2. Compressive ZX Plane Results

The ZX plane specimens have a large change in the cross section as they move from the Z+0 to Y-90 orientations. The Z+0 specimens have layer that are parallel to the loading direction, and the Y-90 has layer perpendicular to the loading direction. In the case of the Y-90 direction, in tension it was the weakest orientation because the load easily pulled the interlayer bonds apart resulting in a low strength. In compression, the layers are being pushed together which can create a higher strength since the force is now longer carried by the inter layer bonds.

The representative stress-strain curves for the ZX plane can be seen in Figure 4.22. The Y-22.5 and Y-45 curves show minimal to zero plastic deformation. The two specimens which are oriented near to or parallel to the z-axis show much more deformation and higher strength.

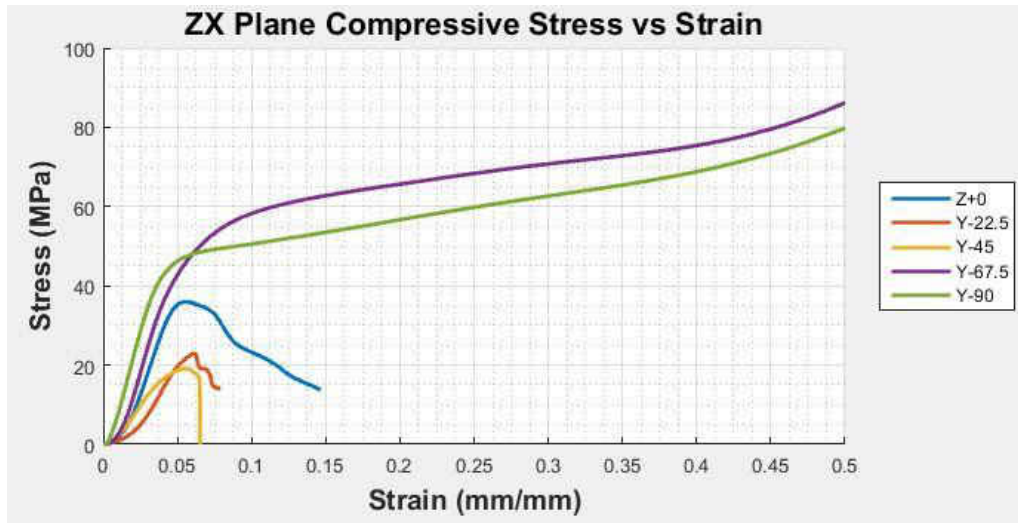


Figure 4.22: Representative stress-strain curves for ZX plane specimens

The tabulated ZX plane compressive strength results can be seen in Table 4.9 and Figure 4.23. The strength initially drops with increasing orientation, but as the load becomes closer to being perpendicular to the layers the strength increases. The Y-67.5 and Y-90 are found to have equal strength, but the Y-67.5 has a much larger confidence interval.

Table 4.9: Compressive strength versus orientation in ZX plane

Compressive Strength vs. Orientation					
Degree	0 Degrees	22.5 Degrees	45 Degrees	67.5 Degrees	90 Degrees
Compressive Strength	35.549	22.438	21.035	56.650	56.182
95%CI	0.656	2.449	2.249	9.245	2.040

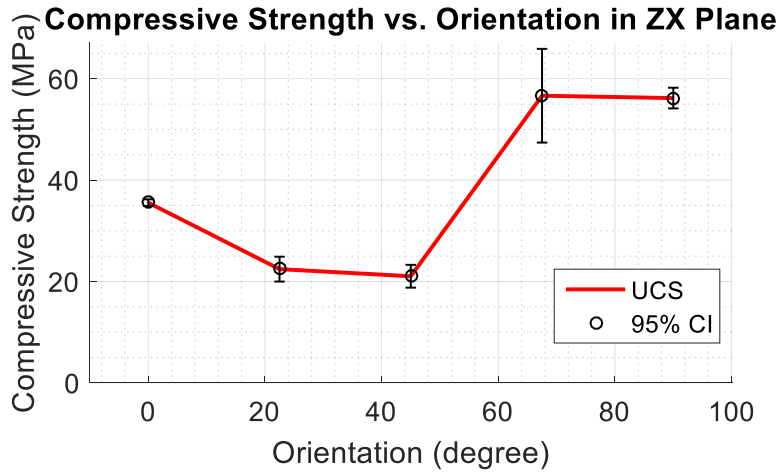


Figure 4.23: Compressive strength for ZX plane samples

The results for the elastic modulus are in Table 4.10 and Figure 4.24. The general trend follows that of the compressive strength, but the elastic modulus of the Y-67.5 orientation is lower than the Y-90 orientation. The Y-67.5 orientation elastic modulus also has a large confidence interval.

Table 4.10: Elastic modulus versus orientation in compression for ZX plane

Elastic Modulus vs. Orientation					
Degree	0 Degrees	22.5 Degrees	45 Degrees	67.5 Degrees	90 Degrees
Elastic Modulus	1018.828	645.611	675.335	925.214	1359.759
95%CI	82.123	19.061	88.125	301.850	87.957

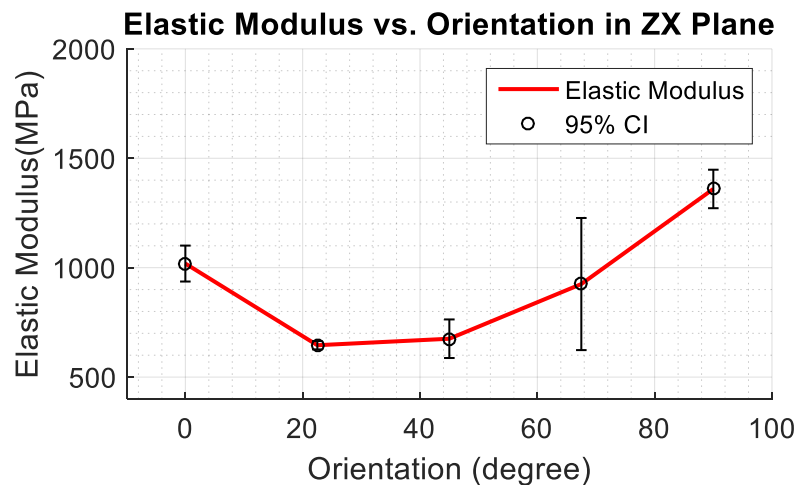


Figure 4.24: Elastic modulus for ZX plane compression samples

4.2.3. Compressive ZX+45 Plane Results

The ZX+45 plane is much like the ZX plane. In compression it is expected that the ZX and ZX+45 planes would have very similar values. Just as was done for the tensile experiments, the Y-90 is used in place of the Y-90/Z+45 sample. These two orientation have very similar cross sections and both have the load perpendicular to their layers. The two orientations are assumed to have the same compressive strength because it was shown they have the same tensile strength.

The representative stress-strain curves for the ZX plane can be seen in Figure 4.25. The curves show similarities to the ZX plane results with the Y-22.5 and Y-45 samples showing minimal deformation and lower strength,

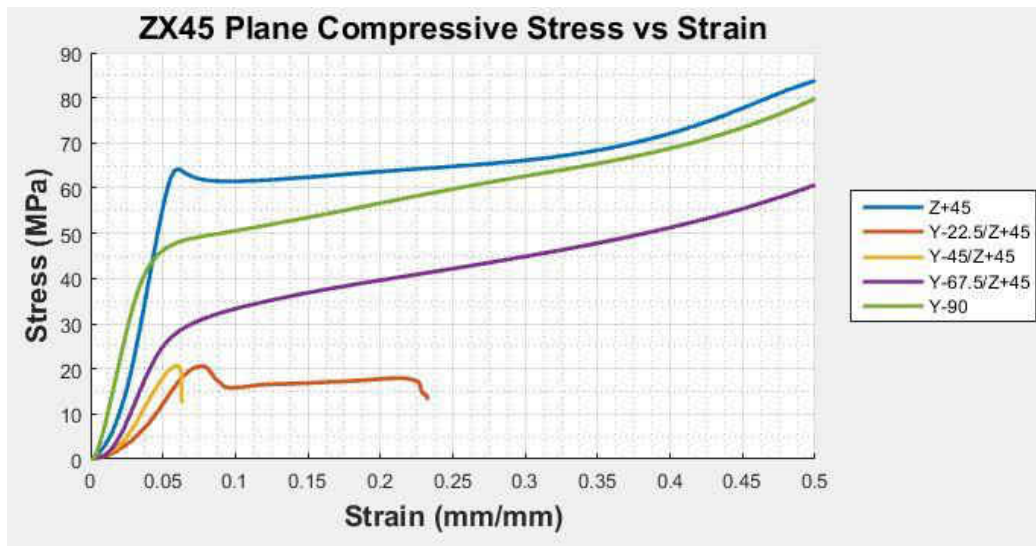


Figure 4.25: Representative stress-strain curves for ZX plane specimens

The results for compressive strength in the ZX+45 plane can be seen in Table 4.11 and Figure 4.26. The trends are the same as the ZX plane with the strength initially dropping and then increasing as the orientation moves to Y-90. In this case the Y-67.5/Z+45 has a lower strength than the Y-90/Z+45.

This creates a smoother transition between the Y-45/Z+45 and Y-90/Z+45 orientations than In the ZX plane.

Table 4.11: Compressive strength versus orientation in ZX+45 plane

Compressive Strength vs. Orientation					
Degree	0 Degrees	22.5 Degrees	45 Degrees	67.5 Degrees	90 Degrees
Compressive Strength	63.638	21.684	23.338	36.872	56.182
95%CI	0.918	2.158	3.513	2.869	2.040

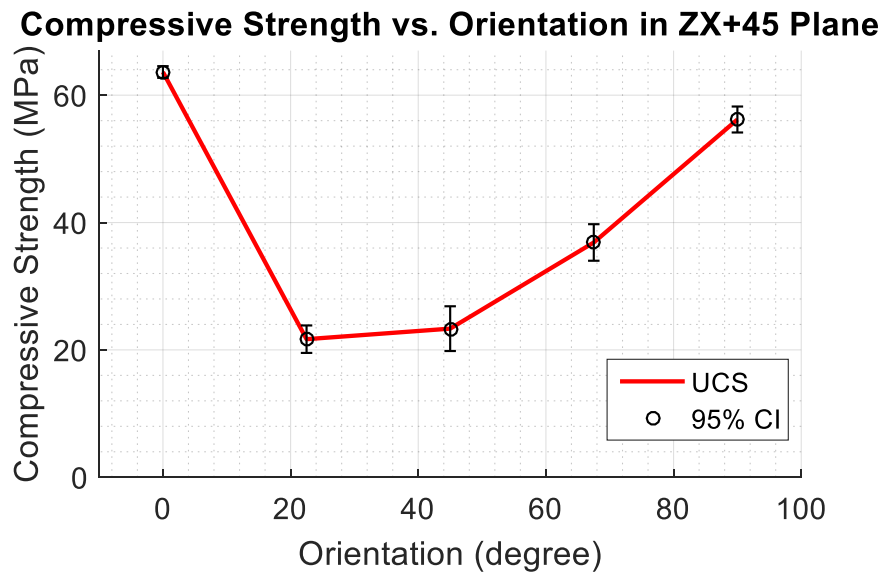


Figure 4.26: Compressive strength for ZX+45 plane samples

The elastic modulus results can be seen in Table 4.12 and Figure 4.27. The elastic modulus follows the same trends as the strength.

Table 4.12: Elastic modulus versus orientation in compression for ZX+45 plane

Elastic Modulus vs. Orientation					
Degree	0 Degrees	22.5 Degrees	45 Degrees	67.5 Degrees	90 Degrees
Elastic Modulus	1639.213	533.269	567.398	734.836	1359.759
95%CI	29.320	71.309	51.953	38.174	87.957

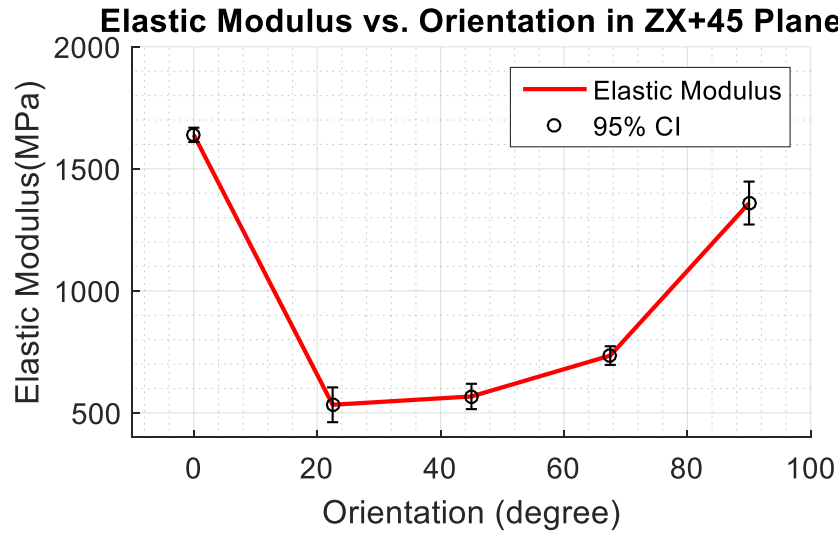


Figure 4.27: Elastic modulus for ZX+45 plane compression samples

4.2.4. Compressive Failure Analysis

During testing, multiple failure modes were observed for specimens in the different orientations. These include buckling, excessive deformation, and brittle fracture. The determining factor for the strength seen in each orientation corresponded to the failure mode observed. Unlike the tensile specimens, the compression specimen failure mode is clearly observable by looking at the final shape of the specimen after testing. No microscopy of failure surfaces are required, this is because most orientations do not produce fracture surfaces to observe. Sectioning or X-ray micro-tomography could be used to further observe the internal failures such as was done in [32], but this is beyond the scope of this work. The specimens printed in the XY plane were found to fail via buckling of layers under the compressive load. This is caused by the layers delaminating and bending out of the plane of the applied stress. An example of this can be seen in Figure 4.28. Once the layer is out of plane, the induced bending causes the specimen to fail even though the stress is below what is required for failure under pure compression.

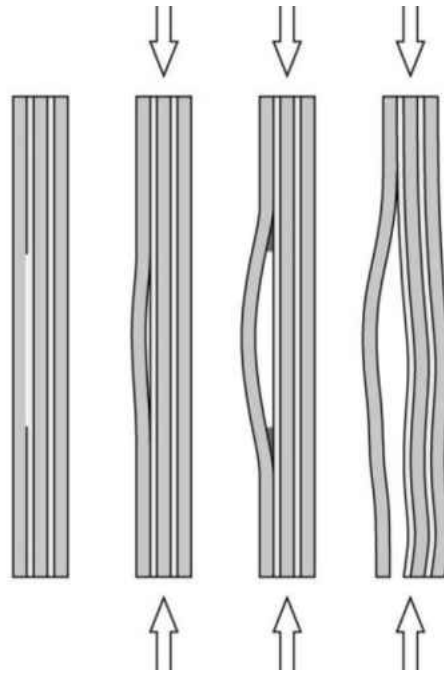


Figure 4.28: Illustration of layer delamination and buckling [44]

In the XY plane the strength and failure mode was consistent for all orientation except for the Z+45 orientation. Upon comparison of the Z+45 and other XY plane specimens, it was discovered that the Z+45 specimens showed significantly less buckling. This can be seen in Figure 4.29 which shows a Z+67.5 and Z+45 specimen after testing. This lack of delamination is due to stronger bonding between the printed layers in the Z+45 specimens which can only be attributed to variance in the printing process. This stronger layer to layer bonding lead to a strength for the Z+45 orientation that was almost double that of the other orientations.



Figure 4.29: Comparison of Z+67.5 (left) and Z+45 (right) specimens after compressive testing

The ZX and ZX+45 plane had varying failure modes with the increase in orientation. Both planes displayed the same failure modes for the corresponding out of plane orientations. At the Z+0 and Z+45 orientations which are the 0° orientations for the ZX and ZX+45 planes respectively, as was just shown, buckling occurred due to the force being parallel to the printed layers. For the Y-22.5 and Y-45 orientations of both planes, brittle fracture occurred. These specimens can be seen in Figure 4.30. This brittle failure occurs due to the shear stress on the interlayer bonds induced by the off axis force. This shear failure is the cause of the quick drop in strength seen as the orientation moves from 0° to 22.5° . After this initial drop, the compressive strength sees an increase in strength as the orientation increases as the force become closer to being parallel to the printed layers. This begins with the 45° orientation of each plane and continues from there.

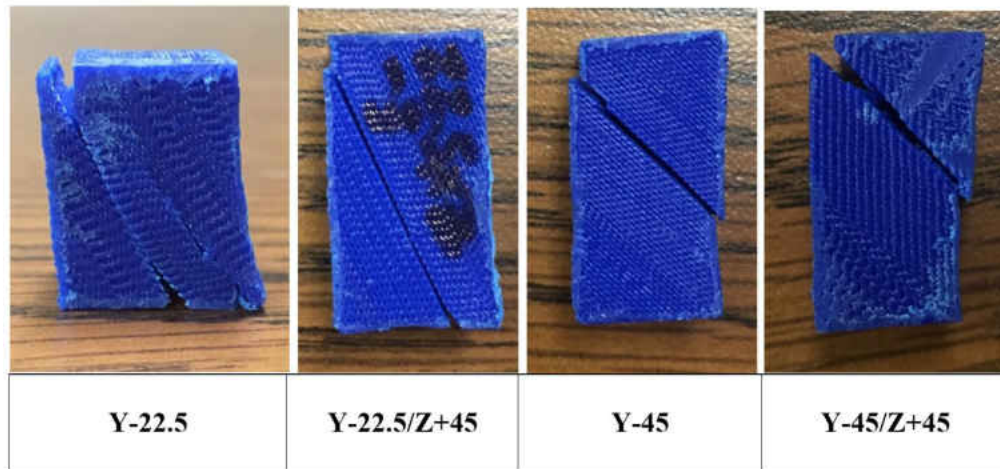


Figure 4.30: Brittle fracture of 22.5° and 45° specimens for ZX and ZX+45 planes

The Y-67.5 and Y-67.5/Z+45 specimens failed due to excessive deformation. These specimens can be seen in Figure 4.31. They specimens were able to resist the brittle shear failure since the layers were near perpendicular to the force which reduced the shear stress experienced by the sample. This allowed the 67.5° to have a relatively high strength compared to the 22.5° and 45° orientations in the ZX and ZX+45 planes.



Figure 4.31: The Y-67.5 (left) and Y-67.5/Z+45 (right) specimens after testing.

The Y-90 specimen was also found to fail from excessive deformation. The Y-90 specimen after testing can be seen in Figure 4.32. This specimen has the force directly perpendicular to the printed layers. This allows it to have a very high strength since there is no interaction between shear or buckling forces and the weak interlayer bonds.



Figure 4.32: The Y-90 specimen after testing

CHAPTER 5: MODELING

In the experimental results, the candidate material showed a complex and anisotropic behavior with high sensitivity to changes in orientation. This also included a high level of tensile-compressive asymmetry at certain orientations. In the failure analysis, multiple failure modes were identified and were also found to change with orientation. All of these factors add up to a multifaceted material behavior that becomes very difficult to predict.

5.1. FDM Failure: Methods and Theory

In an attempt to match a failure theory to the candidate material, the Tsai-Wu failure criteria was fit to the experimental data. This failure theory was chosen for the ability to accommodate both anisotropy and tensile-compressive asymmetry. As was discussed in section 2.3.2, Tsai-Wu failure criteria is described by

$$F_i \sigma_i + F_{ij} \sigma_i \sigma_j = 1 \quad (2.28)$$

In which the matrices F_i and F_{ij} can be simplified using the symmetry observed in a material. In the mesostructural study done in section 3.4, a symmetry was seen between the pair Z+0 and Z+90, and Z+22.5 and Z+67.5. In the experimental section this same symmetry was seen in the data. Although the pairs were not an exact match, the results were within the uncertainty of the study and lead to the conclusion that material is tetragonal and has a rotational symmetry of $\pi/2$ about the z-axis. This added symmetry allows for a further simplification of the Tsai-Wu constant matrices F_i and F_{ij} . By the tetragonal nature implies $X = Y$ and $X' = Y'$ which results in

$$F_1 = \frac{1}{X} - \frac{1}{X'} \quad F_2 = F_1 \quad F_3 = \frac{1}{Z} - \frac{1}{Z'}$$

Furthermore, using equation 2.19 and substituting in the F_{ij} matrix seen in equation 2.29 for the stiffness matrix C you end with the result

$$F_{11} = \frac{1}{XX'} \quad F_{22} = F_{11} \quad F_{33} = \frac{1}{ZZ'} \quad F_{44} = \frac{1}{Q^2} \quad F_{55} = F_{44} \quad F_{66} = \frac{1}{S^2}$$

For the off axis terms there is also a simplification

$$F_{23} = F_{31}$$

From the Experimental results we have all the needed information in order to calculate the needed constants for the Tsai-Wu criteria, except for the off axis F_{ij} terms F_{12} , F_{23} , and F_{31} . For these values bi-axial test are desired, however in the original Tsai-Wu criteria publication an alternate equation is given which lets you calculate the F_{12} , F_{23} , F_{31} terms using the results from a 45° off axis uniaxial experiment. This allows the use of the results from the Z+45 and Y-45 experiments to calculate the off axis terms. The alternate equations take the form

$$F_{12} = \frac{\left(\frac{4}{UU'} - F_{11} - F_{22} - F_{66}\right)}{2}$$

$$F_{23} = F_{31} = \frac{\left(\frac{4}{VV'} - F_{22} - F_{33} - F_{55}\right)}{2}$$

Where U and U' are the strengths of the Z+45 samples in tension and compression respectively, and V and V' are the strengths of the Y-45 samples in tension and compression respectively.

5.2. FDM Failure: Implementation and Results

Using the equations developed for the Tsai-Wu F_i and F_{ij} matrices, a Matlab code was developed to plot the resulting failure theory versus the experimental values. Each constant in the F_i and F_{ij} matrices is calculated using the experimental values. To enforce tetragonal symmetry, the Z+0 and Z+90 strengths in tension are averaged and used for the X and Y values and the Z+0 and Z+90 strengths in compression are averaged and used for the X' and Y' values. Like the results section, the resulting data is plotted by plane, but with both the tensile and compressive results on the same graph.

For the XY plane, the comparison of the Tsai-Wu criteria and the experimental values can be seen in Figure 5.1. For the XY plane, the 0° and 90° values are equal and very close to the experimental values. This is ensured by the use of these points in determining the value of the Tsai-Wu constants. The important part to note in this, and all other graphs in this section, is the trend between the endpoints. For the compressive data, the trend captures the increasing strength up to the 45° orientation and the decreasing strength after. The Z+45 compressive data point falls well above the trend. As was noted in the experimental results section, this value was larger than expected. The 45 specimens also exhibited stronger interlayer bonding which prevented buckling to occur. This is most likely due to an inconsistency in the printing process when printing the Z+45 samples.

For tensile results, the trend shows an increasing strength up to the 45° and then a decreasing strength. This is opposite of the trend seen in the experimental data. The strength value at the 45° orientation is determined by the shear strength used to calculate the constants. It was found by using different shear strength values for tension and compression, the 45° strength value can be lower causing a better fit. This could help accommodate the different failure modes seen in tension and compression, but needs to be studied further.

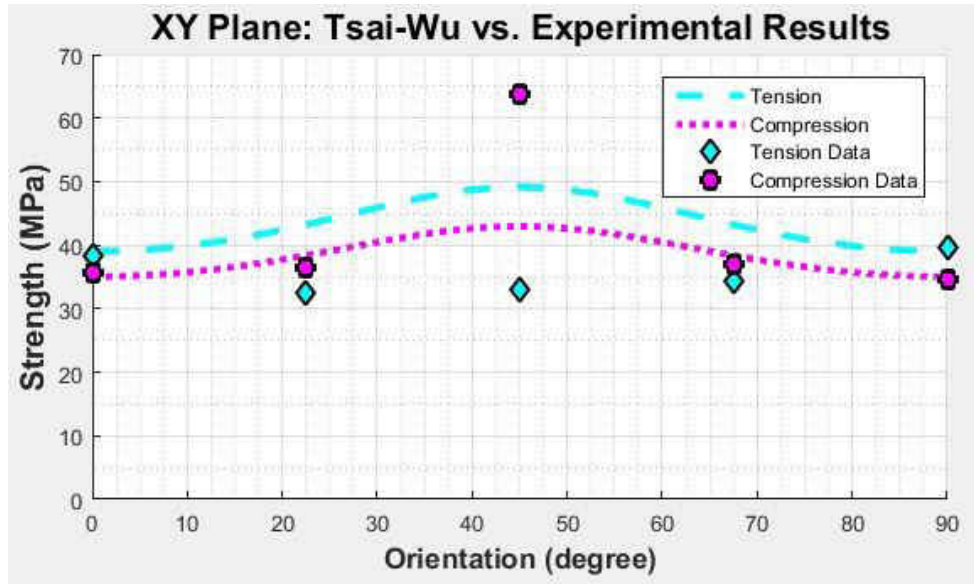


Figure 5.1: Tsai-Wu failure criteria vs experimental results for the XY axis in tension and compression

For the ZX plane, the comparison of the Tsai-Wu criteria and the experimental values can be seen in Figure 5.2. For the compression data, the trend captures the decreasing and then increasing nature of the strength with orientation, however the curve is well above the 22.5° and 45° values and below the 67.5° value.

For the tension data, the trend captures the quickly falling strength with orientation. The 22.5° value is above, but all other values fall very close to the failure line.

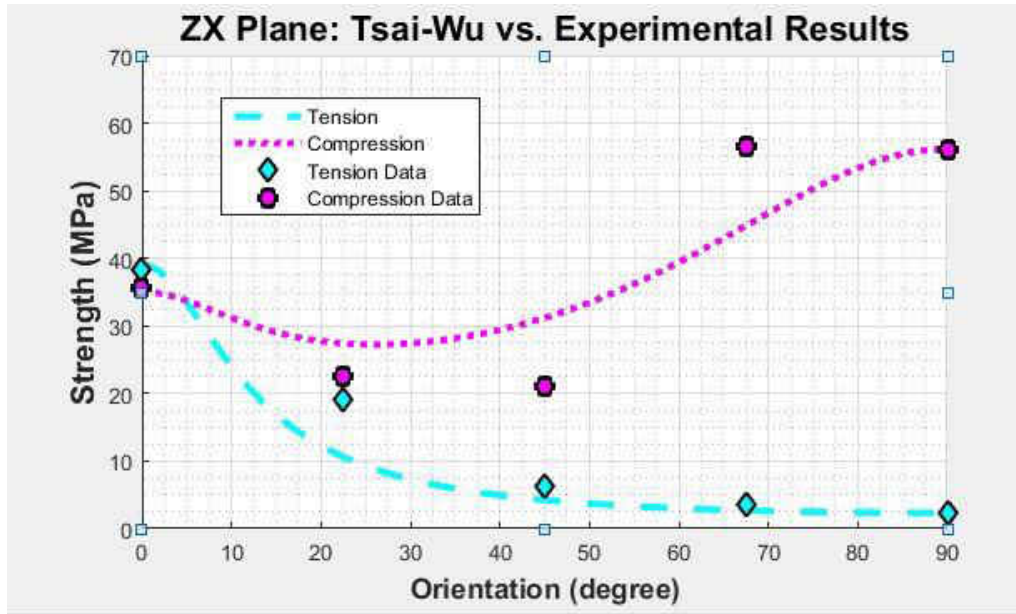


Figure 5.2: Tsai-Wu failure criteria vs. experimental results for the ZX axis in tension and compression

For the ZX plane, the comparison of the Tsai-Wu criteria and the experimental values can be seen in Figure 5.3. For this plane the 0° values correspond to the 45° values from the XY plane. Just as seen in the XY plane, the compressive value is higher than expected and falls well above the trend, and the tensile value fall below the failure line. For the other compression data, the line captures the overall trend just as it did for the ZX plane, but is above 22.5° , 45° , and 67.5° values. The remaining tensile results fall along the predicted values.

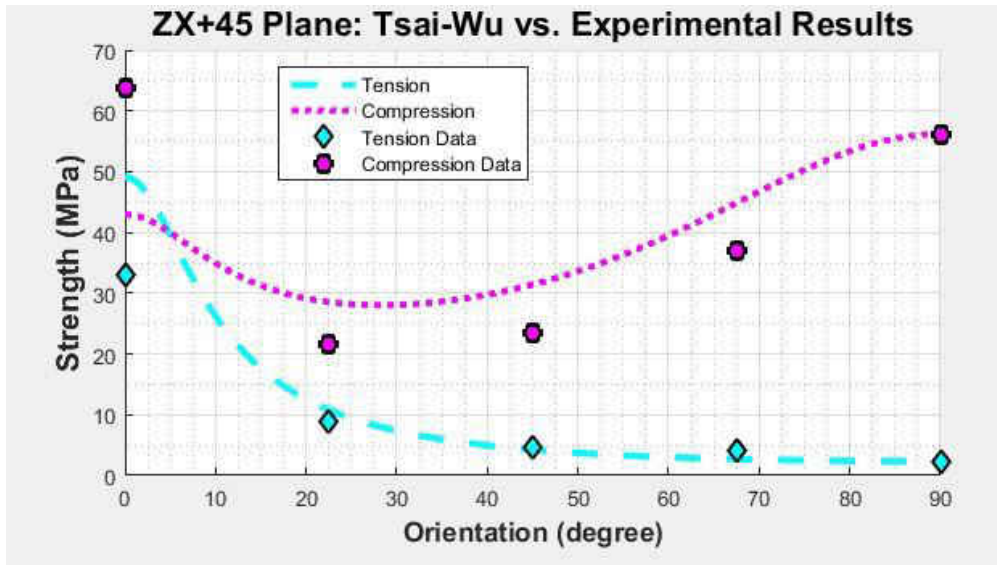


Figure 5.3: Tsai-Wu failure criteria vs. experimental results for the ZX+45 axis in tension and compression

To get a 3D visualization and comparison of the fully 3D failure behavior of the FDM material as predicted by the Tsai-Wu failure criteria, a uni-axial tensile and compressive failure surface was plotted using the Tsai-Wu criteria. The surface is made of a mesh of lines. The direction to a point on the surface represents the orientation of the material, and color indicates the magnitude and there for the predicted strength at the given orientation.

These graphs help visualize just the extent to which FDM materials are tensile-compressive asymmetric. This epitomized by the fact that the strongest orientation in compression is the weakest in tension. The compression surface is shaped like paraboloid which increase as it approaches the XY plane. This is due to the relatively high strength in the XY plane, decreasing strength moving to the 22.5° out of XY plane areas and then increasing strength to the max strength along the z-axis. The tensile surface is a very flat square shape which is a result of the max strength being in the XY plane and the weakest being along the z-axis.

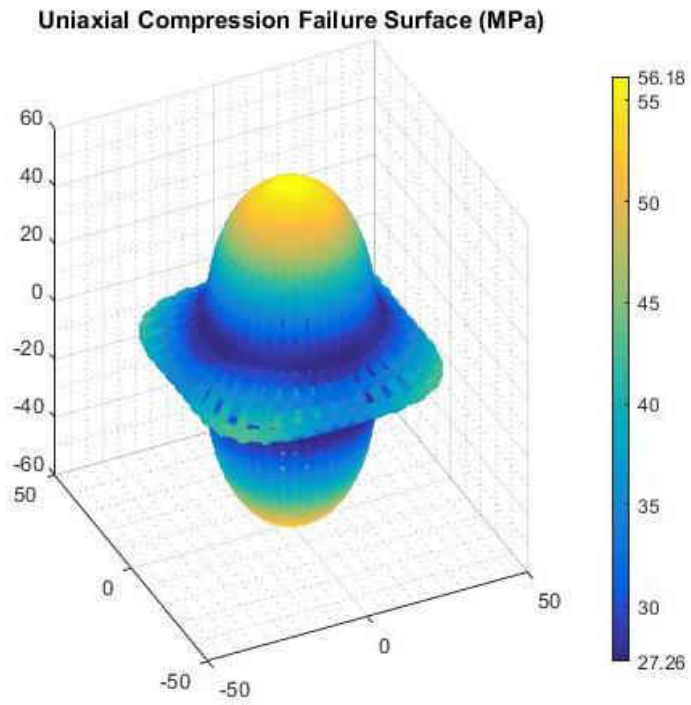


Figure 5.4: Failure surface for uni-axial compression as predicted by the Tsai-Wu criteria

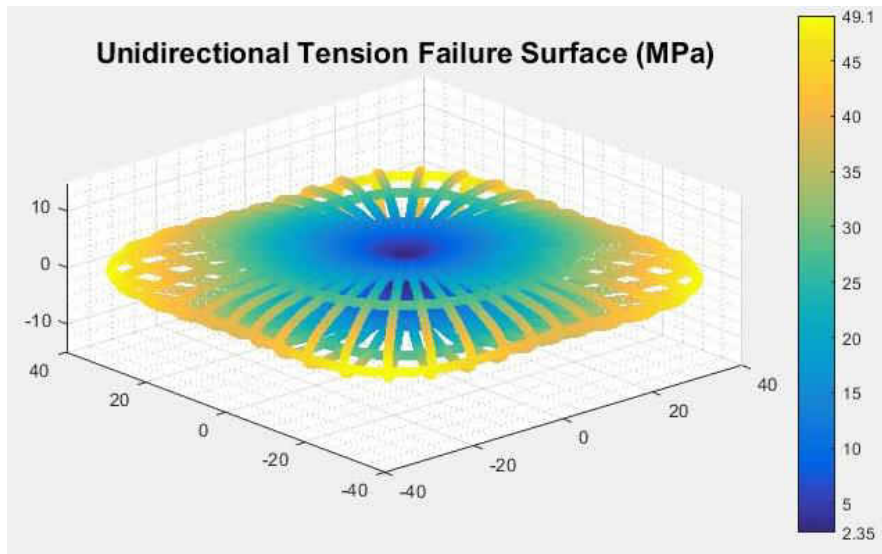


Figure 5.5: Failure surface for uni-axial tension as predicted by the Tsai-Wu criteria

Overall the Tsai-Wu criteria does a great job of capturing the trends seen in each plane, but fall short of correlating directly to the experimental values in many cases. However the failure surfaces created help visualize the complex behavior of FDM material. These results show promise for the use of the Tsai-Wu theory in future experiments of this type. It also gives reason to believe a new theory, possibly based on Tsai-Wu or another quadratic failure theory could be developed to better describe the complex behavior FDM materials.

CHAPTER 6: CONCLUSIONS

Given the popularity and investment into Additive Manufacturing in the last 5 years, it is safe to say that it will continue to revolutionize the manufacturing sector for years to come. Having the ability to manufacture parts with complex and custom geometries will encourage innovation and change the way engineers design. To truly utilize this ability though studies such as this will need to continue so that parts produced through AM can be trusted and qualified.

6.1. Closing Statements on Preformed Work

In this work, many knowledge gaps have been addressed. Through a mesostructural study, the cross section of FDM materials at multiple orientations was visualized. Although qualitative, this data helps understand why FDM materials have a direction-dependent behavior and where some symmetries lie. Through tensile and compressive experiments, the tensile and compressive strength and elastic modulus of the candidate material was recorded for 11 orientations. No study before has tested specimens in both tension and compression at this number of orientations. Through the analysis of this data, it was found that the material exhibits a tetragonal behavior with tensile-compressive asymmetry. Through the examination of failure surfaces and tested samples, the modes of failure and fracture were recorded with respect to how they change with orientation. Understanding the failure mechanisms can aid in developing future FDM specific failure criteria. Finally, the Tsai-Wu failure criteria was applied to the experimental data. Test in 5 orientations, Z+0, Z+45, Z+90, Y-45 and Y-90 were used to populate the Tsai-Wu coefficients and then the resulting failure surface for uniaxial tension and compression were compare to the experimental results. The comparison showed that the Tsai-Wu theory captured the general trends for almost all planes, but did not align with the experimental data in many places. This information can also be used in developing future failure criteria that can possibly tweak the Tsai-Wu coefficients to better fit experimental data.

This work sets the stage for future studies dealing with the failure of FDM parts. Through stressing the need for a complete understanding of the material behavior and showing the importance of the need for compressive and tensile testing of specimens all printed on the same printer, this sets a standard for future studies to use. As printing continues standardizing will allow for printers and therefore the parts produced by that printer to be certified for properties. Standardization of expected properties from printed parts will help make the potential of 3D printing to truly revolutionize manufacturing become a reality.

6.2. Future Work

As stated prior, this work should be used a stepping off point for future experiments. Future work which should stem from this include:

- Further experiments on test samples which include multiple orientations and test type. These type of experiments will continue to unmask the true interactions of stress and failure in FDM material
- Experiments such as this one but that are conducted using industrial printers. Industrial printers produce more consistent part which will help with the uncertainty of data and will help eliminate process inconsistencies. Also, the theories developed for FDM materials will need to work for industrial printers where end use parts with most likely be manufacture.
- Component level testing using simulation and experimental data to predict the behavior of a component. By developing components that are easily simulated and tested, a comparison can be made to experimental data, and the development of theories to help predict the behavior of AM materials can be tested. This work has already begun as a continuance of this thesis, utilized the

experimental data. The component seen in Figure 6.1 is designed to be able to be analytically solved, easily simulated, and easily tested. It can also be printed in a number of orientations with little trouble.

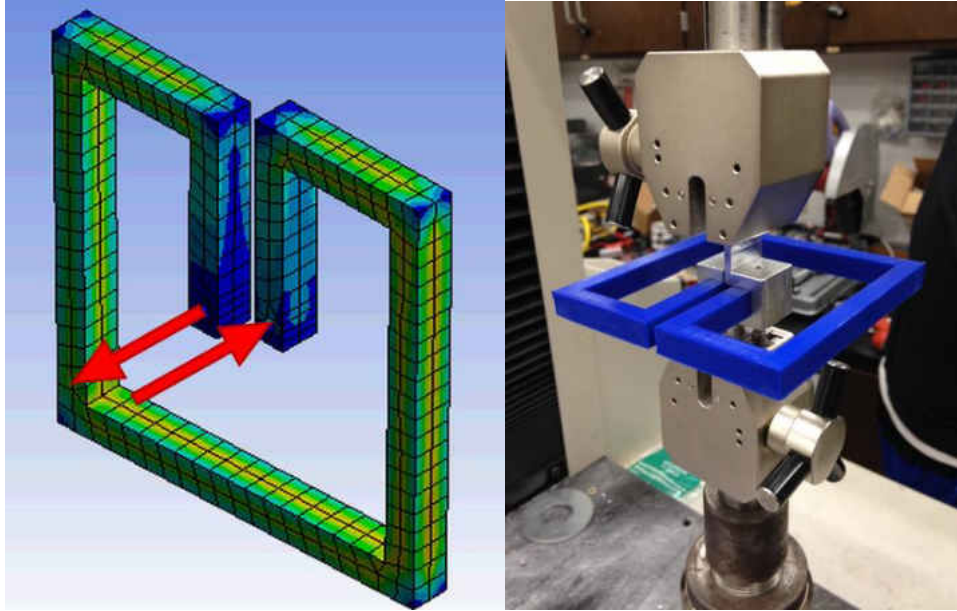


Figure 6.1: Component simulation (left) and component testing (right)

APPENDIX A: TSAI-WU FAILURE CODE

```

%% load data
close all; clear all; clc;
tfinal =
[38.3844405051970,3055.52654632276,38.3844405051970,3055.52654632276,33.1316020473478;32.4
441461196807,2585.43773226578,19.0891914151778,2354.12100182979,8.78205189901206;33.131602
0473478,2446.89344441384,6.28623668872776,1332.84019165836,4.73287471050135;34.25981731799
08,2758.83540956312,3.52363087964026,796.964716682633,3.98267725621327;39.6687026434144,31
46.13596181941,2.33375896899463,636.126964404744,2.33375896899463];
cfinal =
[35.5494612238967,1018.82844677411,35.5494612238967,1018.82844677411,63.6384473946997;36.3
878861597352,1164.69549687703,22.4381173454449,645.610803376156,21.6838638783597;63.638447
3946997,1639.21313602150,21.0346685921127,675.334985023572,23.3381850905876;36.87150026469
83,1004.40262864432,56.6498782618199,925.214115033268,36.8715002646983;34.5127242004761,88
7.598302173295,56.1818050551565,1359.75936795347,56.1818050551565];
for i = 1:5
degree(i) = (i-1)*22.5;
end

% XY = 1 , ZX = 3 , ZX+45 = 5
pl = 1;

%% Tsai-Wu
% S = cauchy stress matrix
% s = voight notation
% f = Fi matrix
% F = Fij matrix
% T = shear stresses
% Q,R,S = T23, T31, T12 in that order

%tensile-compressive strengths
Xt = (tfinal(1,1)+tfinal(5,1))/2;
Xc = (cfinal(1,1)+cfinal(5,1))/2;
Yt = Xt;
Yc = Xc;
Zt = tfinal(5,3);
Zc = cfinal(5,3);

% %Shear strength (symmetry term T23 = T31)
T23 = 7;
T31 = T23;
T12 = 23;
% ss12(shear) = T12;
Qt = T23;
Rt = T31;
St = T12;

Qc = T23;
Rc = T31;

```

```

Sc = T12;
%Sc = St;
%45 off axis results
Ut = tfinal(3,1);
Vt = tfinal(3,3);
Wt = Vt;
Uc = cfinal(3,1);
Vc = cfinal(3,3);
Wc = Vc;

f(1) = (1/Xt)-(1/Xc);
f(2) = (1/Yt)-(1/Yc);
f(3) = (1/Zt)-(1/Zc);

f(4) = (1/Qt)-(1/Qc);
f(5) = (1/Rt)-(1/Rc);
f(6) = (1/St)-(1/Sc);

%Axial Terms
F(1,1) = 1/(Xt*Xc);
F(2,2) = F(1,1);
F(3,3) = 1/(Zt*Zc);

%Shear terms
F(4,4) = 1/(Qt*Qc);
F(5,5) = F(4,4);
F(6,6) = 1/(St*Sc);

%Coupled terms (using 45 off-axis approximation)
F(1,2) = ((4/(Ut*Uc))-F(1,1)-F(2,2)-F(6,6))/2;
F(2,1) = F(1,2);

F(1,3) = ((4/(Vt*Vc))-F(1,1)-F(3,3)-F(5,5))/2;
F(3,1) = F(1,3);

F(2,3) = ((4/(Wt*Wc))-F(3,3)-F(2,2)-F(4,4))/2;
F(3,2) = F(2,3);

%To have a closed and convex surface, (F(i,i)*F(j,j))-(F(i,j)^2)>=0
for i = 1:3
for j = 1:3
CC(i,j) = (F(i,i)*F(j,j))-(F(i,j)*F(i,j));
if CC(i,j) < 0
fprintf('Compliance not met ---> ((F(i,i)*F(j,j))-(F(i,j)^2) < 0 ) ')
CC
return
end
end
end

```



```

end

S = zeros(3);
S(1,1) = 0;
TS = S(1,1);
for elev = 1:2
    elev
    for rot = 1:41
        rot
        S = zeros(3);
        S(1,1) = 0;
        TS = S(1,1);
        if elev == 1
            THETA = 1801;
        else
            THETA = 3601;
        end
        for theta = 1:THETA
            theta;
            %TS = TS-1;
            TS = TS+1;
            %tx = 0;
            if elev == 1
                ty = ((theta-901)/10)*pi/180;
                %ty = ((rot-21)*10)*pi/180;
                %ty = 0;
                %tz = pi/4;
                tz = ((rot-1)*9)*pi/180;
                %tz = ((theta-1)/10)*pi/180;
                t(theta) = (theta-1)/10;
            else
                %ty = ((theta-1)/10)*pi/180;
                ty = ((rot-21)*9)*pi/180;
                %ty = 0;
                %tz = 0;
                %tz = ((rot-1)*10)*pi/180;
                tz = ((theta-1)/10)*pi/180;
                t(theta) = (theta-1)/10;
            end
            %Rx = [ 1 0 0; 0 cos(tx) -sin(tx); 0 sin(tx) cos(tx)];
            Ry = [ cos(ty) 0 sin(ty); 0 1 0; -sin(ty) 0 cos(ty)];
            Rz = [cos(tz) -sin(tz) 0 ; sin(tz) cos(tz) 0; 0 0 1];
            R = Ry*Rz;
            S = R'*S*R;
            % Voigt Notation
            s(1) = S(1,1);
            s(2) = S(2,2);
            s(3) = S(3,3);
        end
    end
end

```

```

s(4) = S(2,3);
s(5) = S(3,1);
s(6) = S(1,2);
% LT = Left Terms = si*fi
% Lsum = Left Sum
Lsum = 0;
Rsum = 0;
done = 0;
fcrit = 0;
while done == 0
if fcrit < 1
%This sets the search precision
TS = TS-.01;
%TS = TS+.01;
S = zeros(3);
S(1,1) = TS;
%Rx = [ 1 0 0; 0 cos(tx) -sin(tx); 0 sin(tx) cos(tx)];
Ry = [ cos(ty) 0 sin(ty) ; 0 1 0; -sin(ty) 0 cos(ty)];
Rz = [cos(tz) -sin(tz) 0 ; sin(tz) cos(tz) 0; 0 0 1];
R = Ry*Rz;
S = R'*S*R;
%Voigt Notation
s(1) = S(1,1);
s(2) = S(2,2);
s(3) = S(3,3);
s(4) = S(2,3);
s(5) = S(3,1);
s(6) = S(1,2);
Lsum = 0;
Rsum = 0;
LT = 1:6;
for i = 1:6
LT(i) = f(i)*s(i);
Lsum = Lsum+LT(i);
%F matrix terms
% RT = Right terms = Fij*si*sj
% Rsum = Right Sum
RT = zeros(3);
for j = 1:6
RT(i,j) = F(i,j)*s(i)*s(j);
Rsum = Rsum+RT(i,j);
end
end
else
done = 1;
cstrength(theta) = TS;
end
fcrit = Lsum+Rsum;

```

```

end
end
if elev == 2
[x,y,z] = sph2cart(t*(pi/180),ty,-cstrength);
else
[x,y,z] = sph2cart(tz,(t-90)*(pi/180),-cstrength);
hold on
end
%plot(t,tstrength,'LineWidth',3,'LineStyle','--','DisplayName','Tension','Color',[0 1 1])
%plot(t,-cstrength,'LineWidth',3,'LineStyle',':','DisplayName','Compression','Color',[1 0 1])
color = ((x.^2+y.^2+z.^2).^(1/2));
scatter3(x,y,z,20,color)

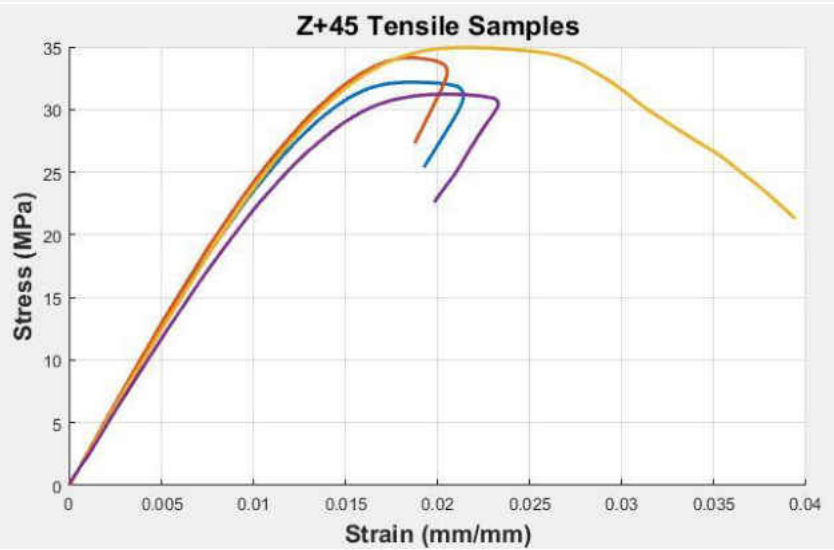
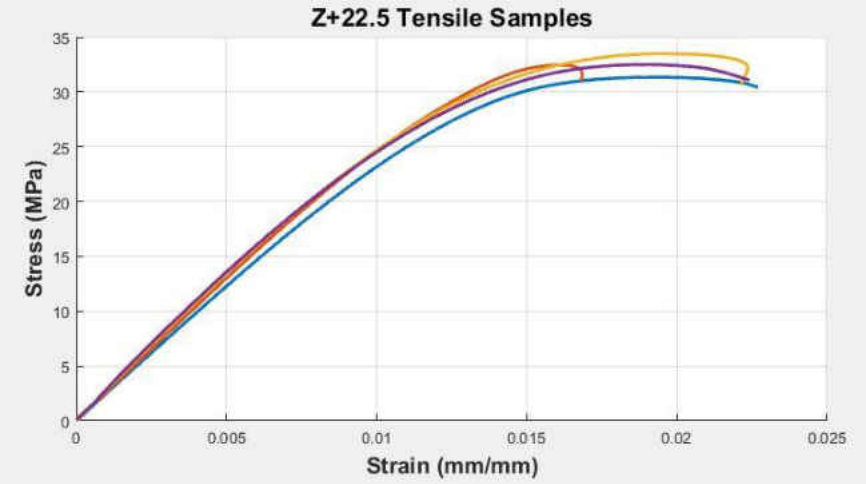
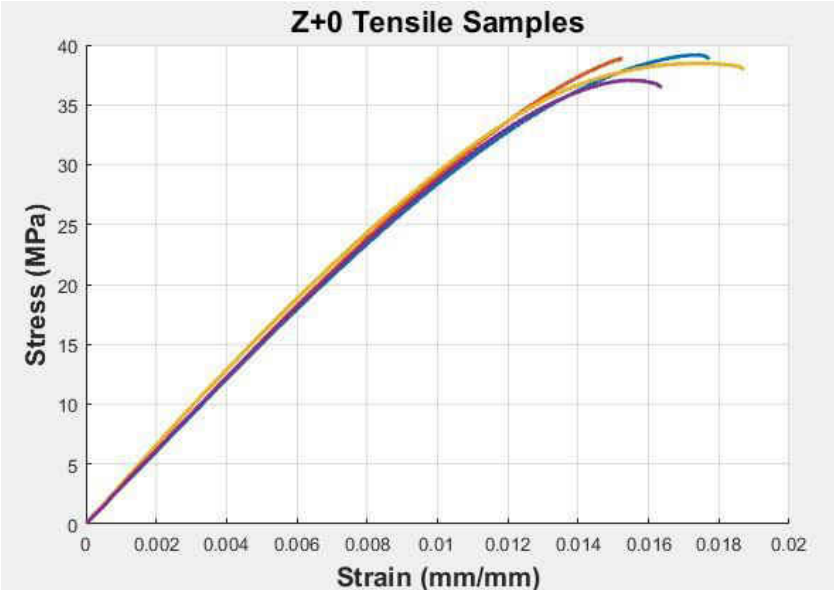
%
%LS = 0;
% for ls = 1:5
% r = ((ls-1)*22.5);
% R(ls) = (-cfinal(ls,pl)-strength((r*10)+1))^2;
% LS = LS+R(ls);
% end
% LS_com(shear) = LS;
end
end
%plot(degree, tfinal(:,pl),'MarkerSize',8,'LineStyle','none','Color',[0 0 0],'DisplayName','Tension
Data','MarkerFaceColor',[0 1 1],'MarkerEdgeColor',[0 0 0],'Marker','d','LineWidth',1.5);
%plot(degree, cfinal(:,pl),'MarkerSize',8,'LineStyle','none','DisplayName','Compression
Data','MarkerFaceColor',[1 0 1],'Marker','o','LineWidth',2,'MarkerEdgeColor',[0 0 0]);

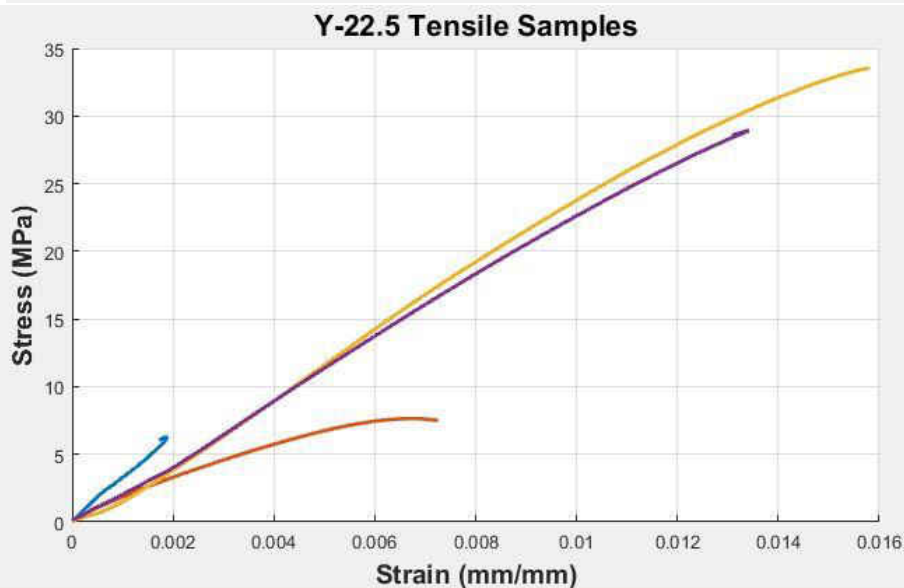
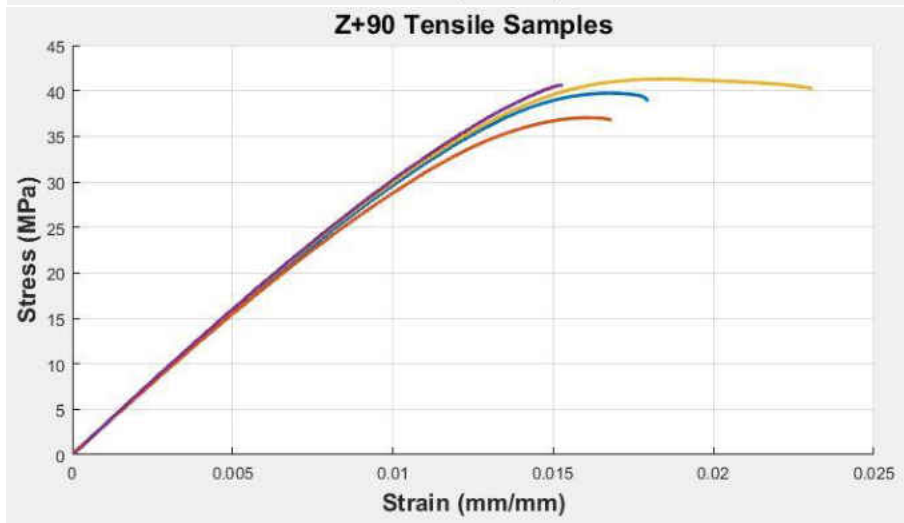
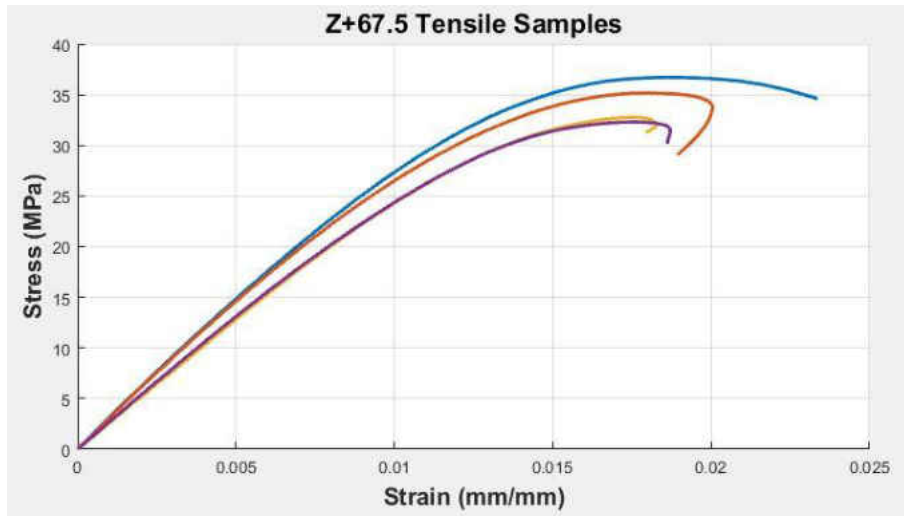
%label({'Orientation (degree)'},'FontWeight','bold','FontSize',13);
%ylabel({'Strength (MPa)'},'FontWeight','bold','FontSize',14);
%title({'Tsai-Wu Uniaxial Compressive Failure Surface (MPa)'},'FontSize',16);
%ax.FontSize = 14;

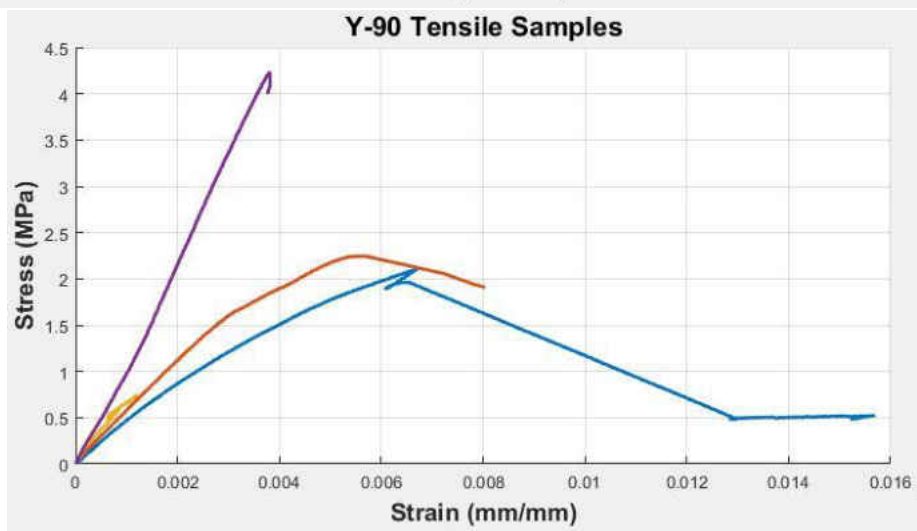
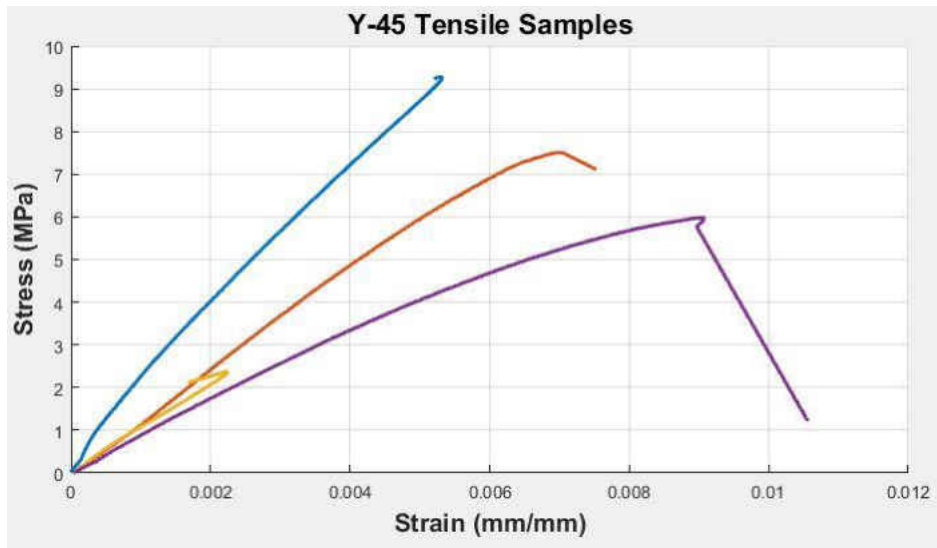
%legend('show');
axis equal
xlim([-60 60])
ylim([-60 60])
zlim([-65 65])
%hold off
%plot(ss12,LS_com)

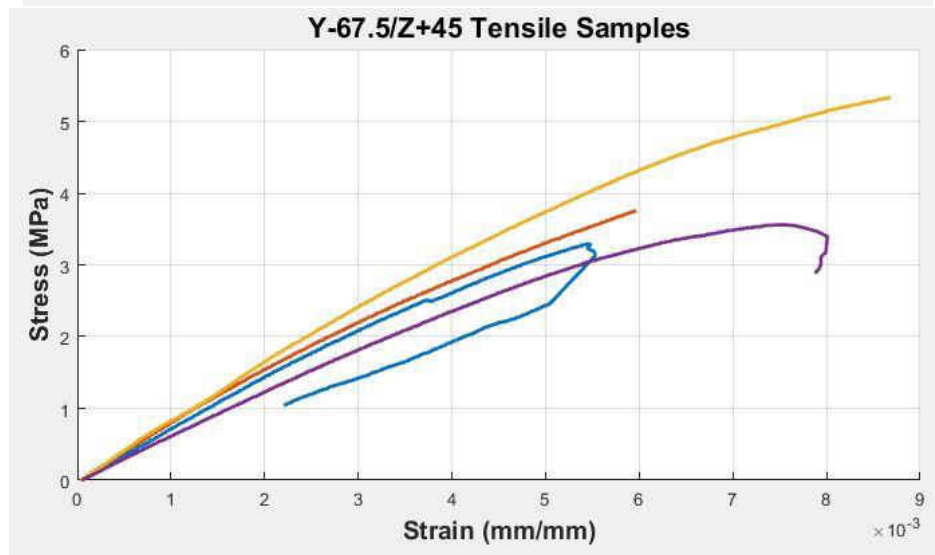
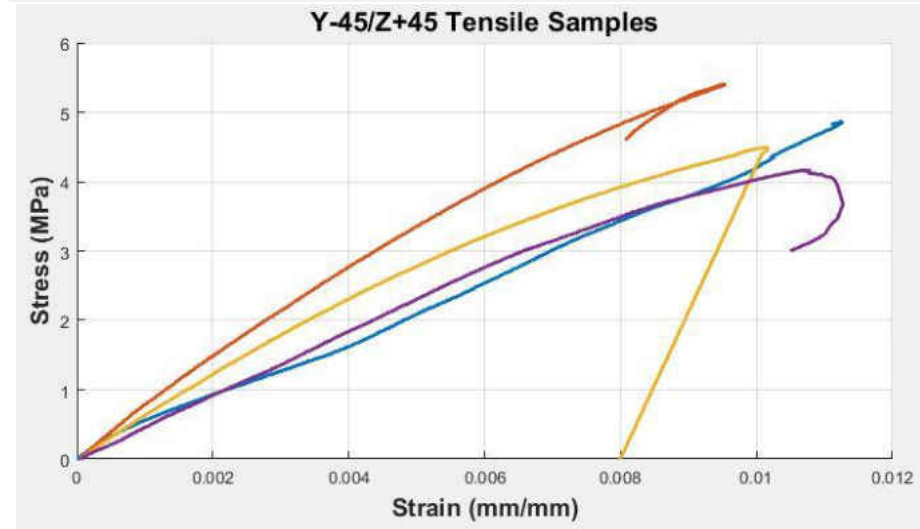
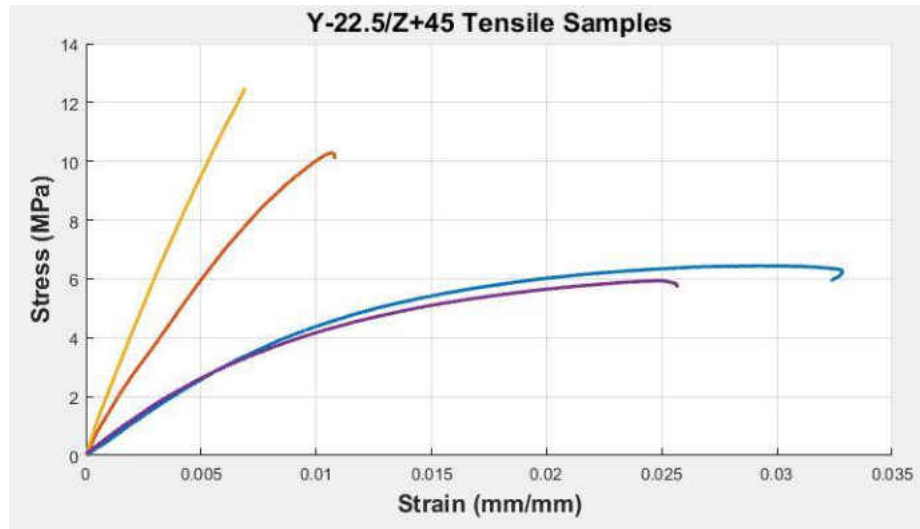
```

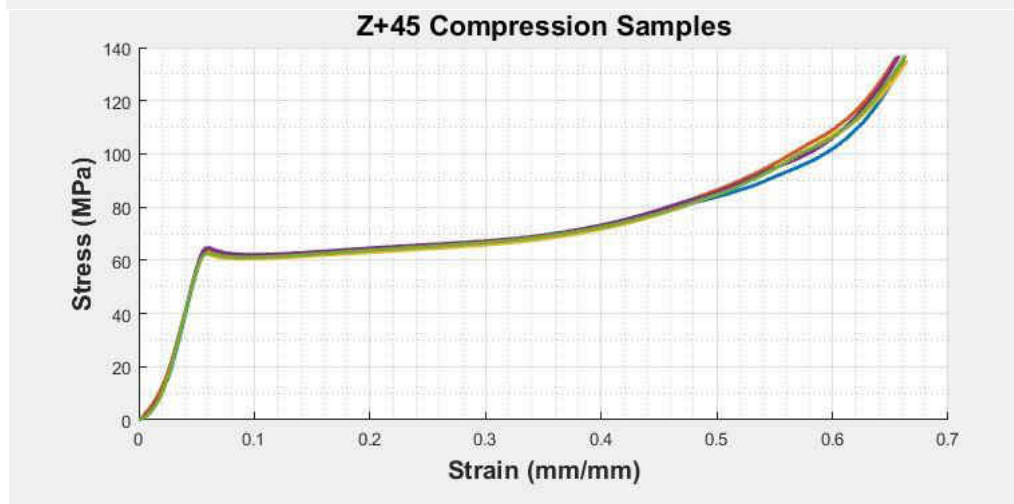
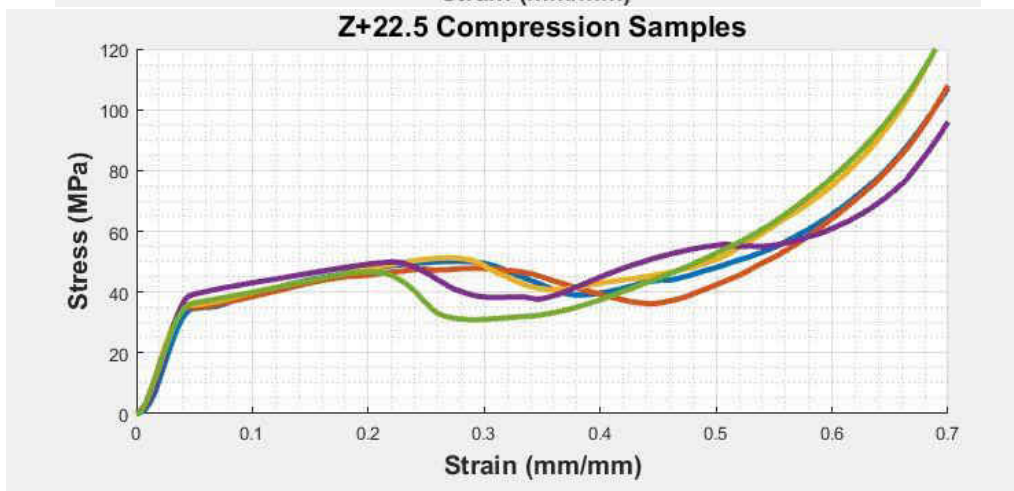
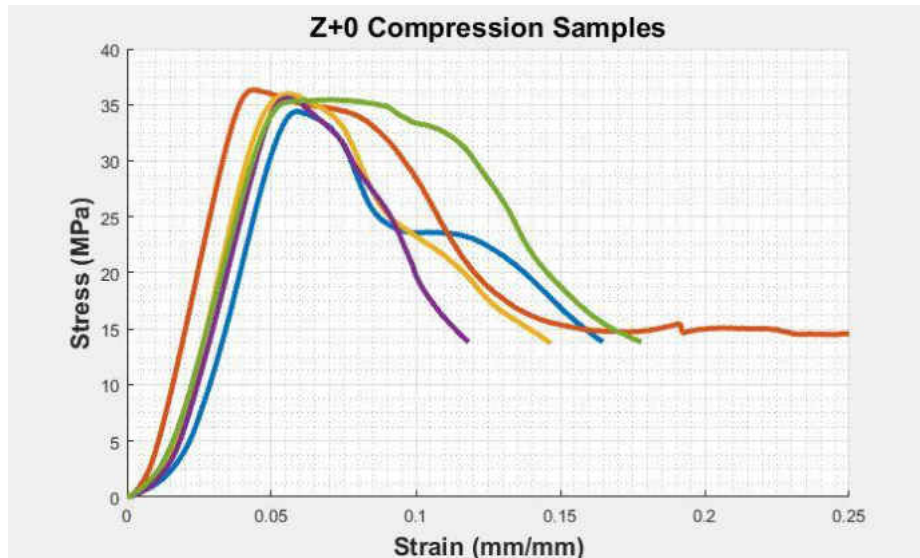
APPENDIX B: STRESS-STRAIN CURVES

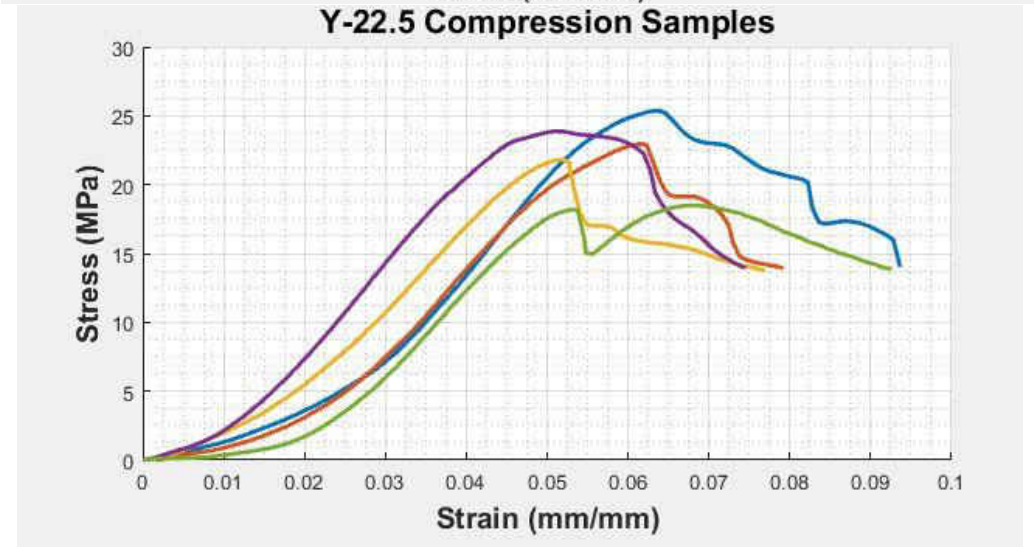
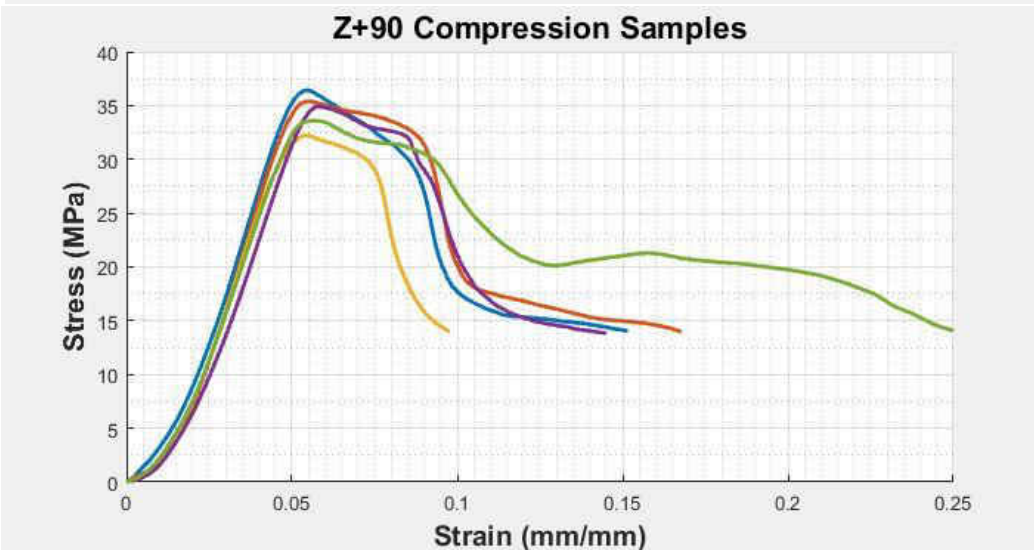
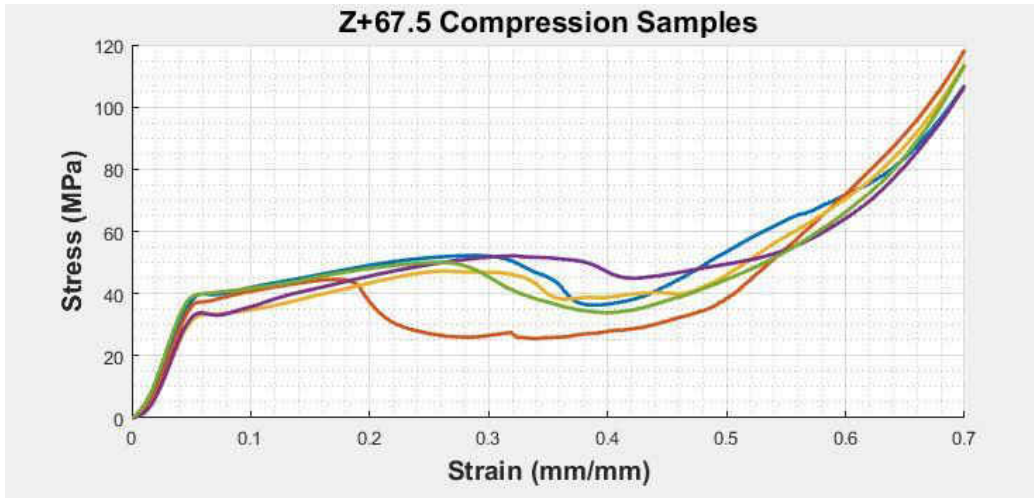




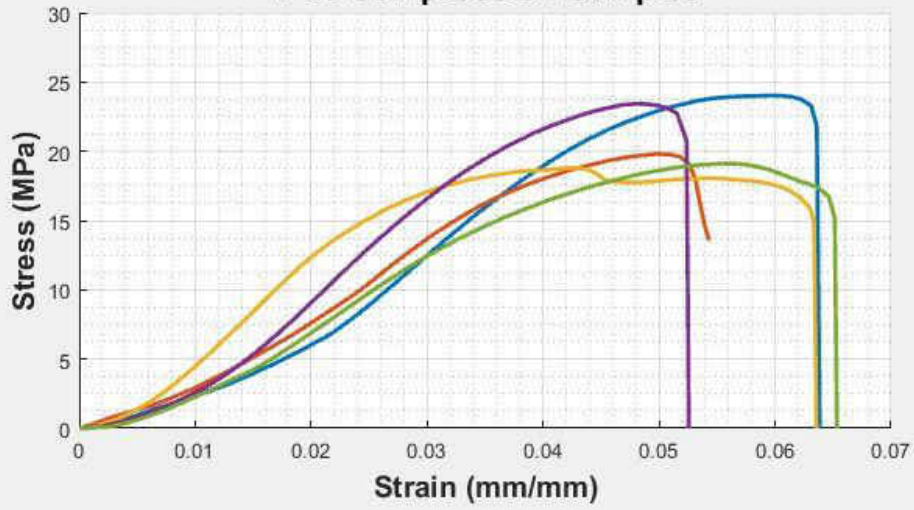




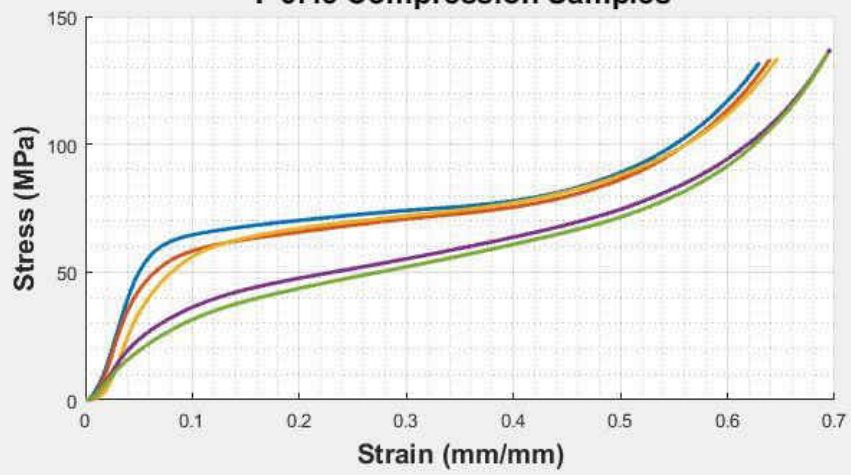




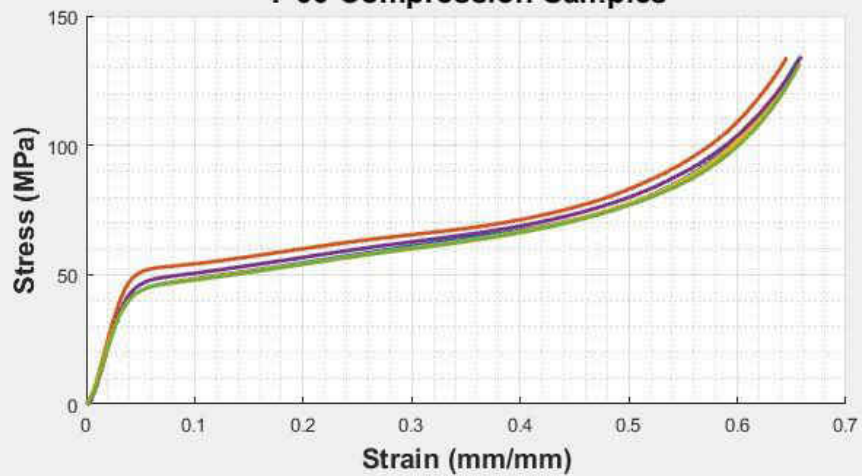
Y-45 Compression Samples

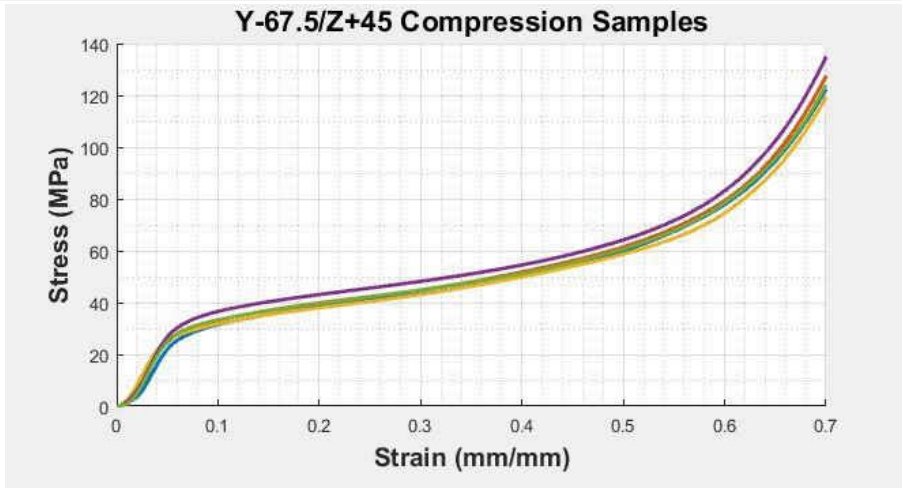
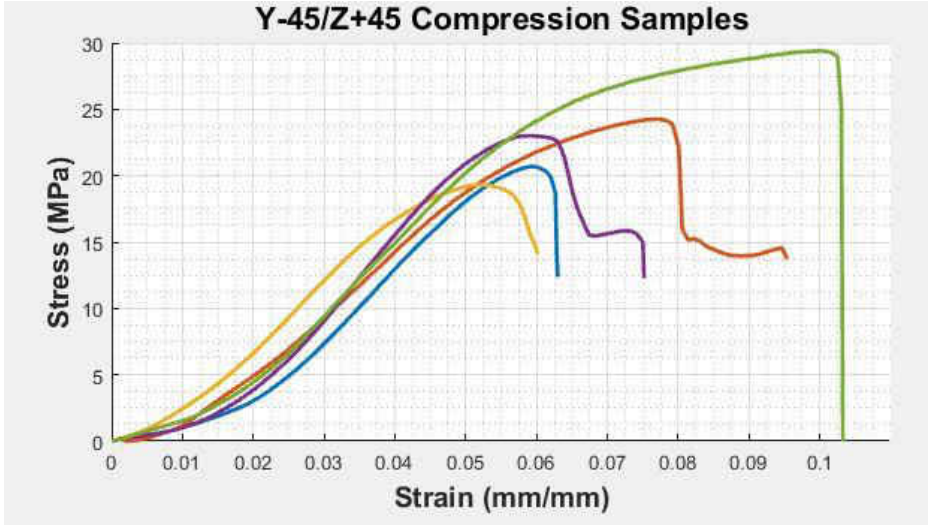
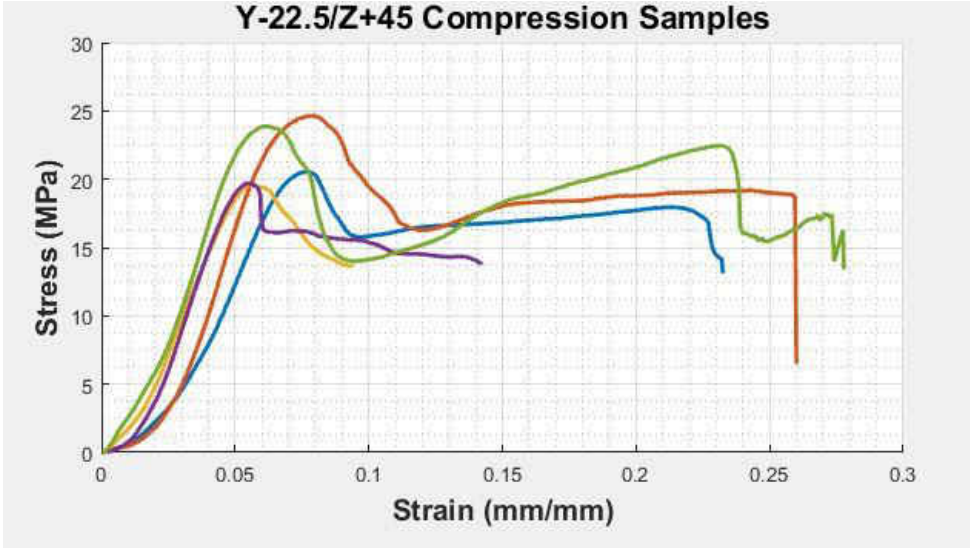


Y-67.5 Compression Samples



Y-90 Compression Samples





APPENDIX C: PRINTER SETTINGS

```
; external perimeters extrusion width = 0.40mm
; perimeters extrusion width = 0.40mm
; infill extrusion width = 0.40mm
; solid infill extrusion width = 0.40mm
; top infill extrusion width = 0.40mm
; support material extrusion width = 0.40mm
; avoid_crossing_perimeters = 0
; bed_temperature = 60
; bridge_fan_speed = 100
; brim_width = 5
; cooling = 1
; disable_fan_first_layers = 3
; duplicate_distance = 6
; extrusion_multiplier = 1.02
; fan_always_on = 0
; fan_below_layer_time = 60
; first_layer_bed_temperature = 60
; first_layer_extrusion_width = 0.4
; first_layer_speed = 50%
; first_layer_temperature = 210
; gcode_flavor = reprap
; infill_first = 0
; max_fan_speed = 100
; max_print_speed = 80
; max_volumetric_speed = 0
; min_fan_speed = 35
; min_print_speed = 15
; min_skirt_length = 0
; nozzle_diameter = 0.4
; only_retract_when_crossing_perimeters = 0
; ooze_prevention = 0
; retract_before_travel = 2
; retract_layer_change = 0
; retract_length = 2
; retract_lift = 0
; retract_lift_above = 0
; retract_lift_below = 0
; retract_restart_extra = 0
; retract_speed = 40
; slowdown_below_layer_time = 4
; standby_temperature_delta = -5
; temperature = 210
; travel_speed = 120
; dont_support_bridges = 1
; extrusion_width = 0.4
; first_layer_height = 0.2
; interface_shells = 0
; layer_height = 0.2
```

```

; raft_layers = 0
; seam_position = random
; support_material = 1
; support_material_angle = 0
; support_material_buildplate_only = 1
; support_material_contact_distance = 0
; support_material_enforce_layers = 0
; support_material_extruder = 1
; support_material_extrusion_width = 0.4
; support_material_interface_contact_loops = 1
; support_material_interface_extruder = 1
; support_material_interface_layers = 3
; support_material_interface_spacing = 0
; support_material_interface_speed = 30
; support_material_pattern = rectilinear
; support_material_spacing = 2
; support_material_speed = 60
; support_material_synchronize_layers = 0
; support_material_threshold = 45
; support_material_with_sheath = 0
; support_material_xy_spacing = 0
; xy_size_compensation = 0
; bottom_solid_layers = 0
; bridge_flow_ratio = 1
; bridge_speed = 30
; ensure_vertical_shell_thickness = 0
; external_fill_pattern = rectilinear
; external_perimeter_extrusion_width = 0.4
; external_perimeter_speed = 30
; external_perimeters_first = 0
; extra_perimeters = 0
; fill_angle = 0
; fill_density = 100%
; fill_pattern = rectilinear
; gap_fill_speed = 30
; infill_every_layers = 1
; infill_extruder = 1
; infill_extrusion_width = 0.4
; infill_overlap = 15
; infill_speed = 30
; overhangs = 1
; perimeter_extruder = 1
; perimeter_extrusion_width = 0.4
; perimeter_speed = 30
; perimeters = 0
; small_perimeter_speed = 30
; solid_infill_below_area = 1
; solid_infill_every_layers = 0

```

```
; solid_infill_extruder = 1
; solid_infill_extrusion_width = 0.4
; solid_infill_speed = 30
; thin_walls = 1
; top_infill_extrusion_width = 0.4
; top_solid_infill_speed = 30
; top_solid_layers = 0
```


REFERENCES

- [1] K. H. Church *et al.*, "Multimaterial and Multilayer Direct Digital Manufacturing of 3-D Structural Microwave Electronics," *Proceedings of the IEEE*, vol. 105, no. 4, pp. 688-701, 2017.
- [2] B. Boen, "Hot-Fire Tests Show 3-D Printed Rocket Parts Rival Traditionally Manufactured Parts," July 24, 2013. Available: <https://www.nasa.gov/exploration/systems/sls/3dprinting.html>
- [3] R. McGillivray, "Joint effort produces Australia's first 3D printed spine implant," Available: <https://www.rmit.edu.au/news/all-news/2015/august/australias-first-3d-printed-spine-implant>
- [4] 3Ders, "Argentinan patient leads normal life with 3D printed cranial implant," Available: <http://www.3ders.org/articles/20150510-argentinan-patient-leads-normal-life-with-3d-printed-cranial-implant.html>
- [5] *Standard Terminology for Additive Manufacturing ‐ General Principles ‐ Terminology*, 2015.
- [6] S. Singh, S. Ramakrishna, and R. Singh, "Material issues in additive manufacturing: A review," *Journal of Manufacturing Processes*, vol. 25, pp. 185-200, 2017.
- [7] G. Costabile, M. Fera, F. Fruggiero, A. Lambiase, and D. Pham, "Cost models of additive manufacturing: A literature review," *International Journal of Industrial Engineering Computations*, vol. 8, no. 2, pp. 263-283, 2017.
- [8] H. W. Hayden, W. G. Moffatt, and J. Wulff, *The structure and properties of materials Vol. III, Vol. III*. New York [etc.]: Wiley, 1965.
- [9] M. Bertoldi, M. Yardimci, C. Pistor, S. Guceru, and G. Sala, "Mechanical characterization of parts processed via fused deposition," in *Proceedings of the 1998 solid freeform fabrication symposium*, 1998, pp. 557-565.

- [10] *Standard Test Method for Determination of Tensile Properties of Moulding and Extrusion Plastics*, 1996.
- [11] J. F. Rodríguez, J. P. Thomas, and J. E. Renaud, "Mechanical behavior of acrylonitrile butadiene styrene (ABS) fused deposition materials. Experimental investigation," *Rapid Prototyping Journal*, vol. 7, no. 3, pp. 148-158, 2001.
- [12] J. Rodriguez, J. Thomas, and J. Renaud, "Maximizing the strength of fused-deposition ABS plastic parts," *Solid Freeform Fabrication Proceedings, Notre Dame, IN*, 1999.
- [13] J. F. Rodríguez, J. P. Thomas, and J. E. Renaud, "Mechanical behavior of acrylonitrile butadiene styrene fused deposition materials modeling," *Rapid Prototyping Journal*, vol. 9, no. 4, pp. 219-230, 2003.
- [14] J. F. Rodriguez, J. P. Thomas, and J. E. Renaud, "Characterization of the mesostructure of fused-deposition acrylonitrile-butadiene-styrene materials," *Rapid Prototyping Journal*, vol. 6, no. 3, pp. 175-186, 2000.
- [15] J. Rodriguez, J. Thomas, and J. Renaud, "Characterizing the microstructure of fused deposition polymer components," in *CAE and Intelligent Processing of Polymeric Materials*, 1997, no. ASME MD-Vol. 79, pp. 299-308: Wiley.
- [16] M. Montero, S. Roundy, D. Odell, S.-H. Ahn, and P. K. Wright, "Material characterization of fused deposition modeling (FDM) ABS by designed experiments," *Society of Manufacturing Engineers*, vol. 10, no. 13552540210441166, 2001.
- [17] S. H. Ahn, M. Montero, D. Odell, S. Roundy, and P. K. Wright, "Anisotropic material properties of fused deposition modeling ABS," *Rapid Prototyping Journal*, vol. 8, no. 4, pp. 248-257, 2002.
- [18] L. Li, Q. Sun, C. Bellehumeur, and P. Gu, "Composite Modeling and Analysis for Fabrication of FDM Prototypes with Locally Controlled Properties," *Journal of Manufacturing Processes*, vol. 4, no. 2, pp. 129-141, 2002.

- [19] A. K. Sood, R. K. Ohdar, and S. S. Mahapatra, "Parametric appraisal of mechanical property of fused deposition modelling processed parts," *Materials & Design*, vol. 31, no. 1, pp. 287-295, 2010.
- [20] D. Croccolo, M. De Agostinis, and G. Olmi, "Experimental characterization and analytical modelling of the mechanical behaviour of fused deposition processed parts made of ABS-M30," *Computational Materials Science*, vol. 79, pp. 506-518, 11// 2013.
- [21] N. Hill and M. Haghi, "Deposition direction-dependent failure criteria for fused deposition modeling polycarbonate," *Rapid Prototyping Journal*, vol. 20, no. 3, pp. 221-227, 2014.
- [22] M. Domingo-Espin, J. M. Puigoriol-Forcada, A.-A. Garcia-Granada, J. Llumà, S. Borros, and G. Reyes, "Mechanical property characterization and simulation of fused deposition modeling Polycarbonate parts," *Materials & Design*, vol. 83, pp. 670-677, 2015.
- [23] A. Lanzotti, D. Eujin Pei, M. Grasso, G. Staiano, and M. Martorelli, "The impact of process parameters on mechanical properties of parts fabricated in PLA with an open-source 3-D printer," *Rapid Prototyping Journal*, vol. 21, no. 5, pp. 604-617, 2015.
- [24] A. R. Torrado and D. A. Roberson, "Failure Analysis and Anisotropy Evaluation of 3D-Printed Tensile Test Specimens of Different Geometries and Print Raster Patterns," *Journal of Failure Analysis and Prevention*, vol. 16, no. 1, pp. 154-164, 2016.
- [25] J. Torres *et al.*, "An approach for mechanical property optimization of fused deposition modeling with polylactic acid via design of experiments," *Rapid Prototyping Journal*, vol. 22, no. 2, pp. 387-404, 2016.
- [26] R. Zou *et al.*, "Isotropic and anisotropic elasticity and yielding of 3D printed material," *Composites Part B: Engineering*, vol. 99, pp. 506-513, 2016.
- [27] *Standard Test Method for Tensile Properties of Plastics*, 2014.

- [28] J. Cantrell *et al.*, "Experimental Characterization of the Mechanical Properties of 3D Printed ABS and Polycarbonate Parts," *Advancement of Optical Methods in Experimental Mechanics, Volume 3 (9783319415994)*, p. 89, 01// 2017.
- [29] *Standard Test Method for Compressive Properties of Rigid Plastics*, 2015.
- [30] C. S. Lee, S. G. Kim, H. J. Kim, and S. H. Ahn, "Measurement of anisotropic compressive strength of rapid prototyping parts," *Journal of Materials Processing Technology*, vol. 187-188, pp. 627-630, 2007.
- [31] A. K. Sood, R. K. Ohdar, and S. S. Mahapatra, "Experimental investigation and empirical modelling of FDM process for compressive strength improvement," *Journal of Advanced Research*, vol. 3, no. 1, pp. 81-90, 1// 2012.
- [32] S. Guessasma, S. Belhabib, H. Nouri, and O. Ben Hassana, "Anisotropic damage inferred to 3D printed polymers using fused deposition modelling and subject to severe compression," *European Polymer Journal*, vol. 85, pp. 324-340, 12// 2016.
- [33] L. Bos, P. Gibson, M. Kotchetov, and M. Slawinski, "Classes of Anisotropic Media: A Tutorial," *Studia Geophysica et Geodaetica*, vol. 48, no. 1, pp. 265-287, 2004// 2004.
- [34] R. v. Mises, "Mechanics of solid bodies in the plastically-deformable state," 1913.
- [35] D. C. Drucker and W. Prager, "Soil mechanics and plastic analysis or limit design," *Quarterly of applied mathematics*, vol. 10, no. 2, pp. 157-165, 1952.
- [36] R. Hill, "A Theory of the Yielding and Plastic Flow of Anisotropic Metals," *Proceedings of the Royal Society of London. Series A. Mathematical and Physical Sciences*, 10.1098/rspa.1948.0045 vol. 193, no. 1033, p. 281, 1948.
- [37] S. W. Tsai and E. M. Wu, "A General Theory of Strength for Anisotropic Materials," *Journal of Composite Materials*, vol. 5, no. 1, pp. 58-80, 1971/01/01 1971.

- [38] J. Torres, J. Coteló, J. Karl, and A. P. Gordon, "Mechanical Property Optimization of FDM PLA in Shear with Multiple Objectives," *Jom*, vol. 67, no. 5, pp. 1183-1193, 2015.
- [39] G. Hodgson. *Slic3r Manual: Flow Math*. Available: <http://manual.slic3r.org/advanced/flow-math>
- [40] L. Buehler, *Buehler Sum-Met: The Science Behind Materials Preparation, A Guide to Materials Preparation and Analysis*. 2007.
- [41] W. Wu, P. Geng, G. Li, D. Zhao, H. Zhang, and J. Zhao, "Influence of Layer Thickness and Raster Angle on the Mechanical Properties of 3D-Printed PEEK and a Comparative Mechanical Study between PEEK and ABS," *Materials*, vol. 8, no. 9, pp. 5834-5846, 2015.
- [42] E. Kim, Y.-J. Shin, and S.-H. Ahn, "The effects of moisture and temperature on the mechanical properties of additive manufacturing components: fused deposition modeling," *Rapid Prototyping Journal*, vol. 22, no. 6, pp. 887-894, 2016.
- [43] A. Bellini and S. Güçeri, "Mechanical characterization of parts fabricated using fused deposition modeling," *Rapid Prototyping Journal*, vol. 9, no. 4, pp. 252-264, 2003.
- [44] J. J. C. Remmers and R. de Borst, "Delamination buckling of fibre–metal laminates," *Composites Science and Technology*, vol. 61, no. 15, pp. 2207-2213, 2001.